Further Development and Testing of a Second-Order Bulk Boundary Layer Model

by
Captain Richard D. Krasner

Department of Atmospheric Science
Colorado State University
Fort Collins, Colorado

David A. Randall, Principal Investigator

Colorado State University

Department of Atmospheric Science

Paper No. 528

FURTHER DEVELOPMENT AND TESTING OF A SECOND-ORDER BULK BOUNDARY LAYER MODEL

by

Captain Richard David Krasner

Department of Atmospheric Science
Colorado State University
Fort Collins, CO

May 1993

Atmospheric Science Paper No. 528

FURTHER DEVELOPMENT AND TESTING OF A SECOND-ORDER BULK BOUNDARY LAYER MODEL

by

Richard David Toumey

Department of Atmospheric Science
Colorado State University
Fort Collins, CO

May 1992

Atmospheric Science Paper No. 502

ABSTRACT

A one-layer bulk boundary layer model is developed following earlier work by Randall and Moeng. The model predicts the mixed layer values of the potential temperature, mixing ratio, and u- and v-momentum. The model also predicts the depth of the boundary layer and the vertically integrated turbulence kinetic energy (TKE). The TKE is determined using a second-order closure that relates the rate of dissipation to the TKE. The fractional area covered by rising motion (σ) and the entrainment rate (E) are diagnostically determined.

The model is used to study the clear convective boundary layer (CBL) using data from the Wangara, Australia boundary layer experiment. The Wangara data is also used as an observation base to validate model results. A further study is accomplished by simulating the planetary boundary layer (PBL) over an ocean surface. This study is designed to find the steady-state solutions of the prognostic variables.

The model clearly illustrated the features found in a CBL. The diurnal trend of the PBL depth was accurately reproduced. This included rapid growth during mid-morning, quasi-steady-state conditions during the afternoon, and an evening transition.

In the ocean study, the prognostic variables converged to their equilibrium values at about the same time. This is in contrast to an earlier study using similar conditions where the adjustment time for the PBL depth was considerably longer than for the other prognostic variables. This discrepancy was due to the different entrainment parameterizations used in each study. In the ocean study, the entrainment rate became very large during the initial portion of the simulation, whereas in the earlier study the entrainment rate remained small and constant throughout.

The TKE became very large during the mid-morning when rapid PBL growth was occurring. This large TKE indicated that the PBL was very turbulent due to the vigorous convection that was taking place. The fractional area covered by rising motion, σ, reached its minimum at this time; a further indication of the intense convection.

The gradients of the mean potential temperature and mean mixing ratio were determined. These gradients were large at the start of the simulation when the PBL was unmixed. The gradients decreased rapidly as turbulence mixed the PBL during mid-morning. The gradients were near zero in the afternoon indicating that the PBL was now well mixed.

A two-layer model was developed to address the problem of large gradients obtained in the one-layer model. This model produced the same results for the prognostic variables as the one-layer model. The gradients determined by the model were near zero. The mean potential temperatures and mixing ratios at the two levels in the model were then initially perturbed to study the effects of varying the dissipation time scale. A certain range of values of the model parameter related to the dissipation time scale allowed the large induced gradients to approach zero in a reasonable time.

The following items were presented for the first time in this thesis:

(1) A positive entrainment rate parameterization which assumes a balance between buoyancy production and dissipation of turbulence kinetic energy.

(2) A negative entrainment rate parameterization that allows the PBL depth to decrease late in the day when buoyancy production is no longer sufficient to maintain the turbulence.

(3) A fully implicit finite difference equation for the TKE (when the entrainment rate is positive) solved as a cubic equation. The square of the solution that is always real is assigned to the TKE.

(4) Results for both the Wangara and Ocean studies showing the fractional area covered by rising motion, convective mass flux, updraft and downdraft properties of $\overline{\theta}$ and $\overline{q}$ at the surface and PBL top, dissipation rates of θ and q at the surface and PBL top, dissipation time scale, and gradients of $\overline{\theta}$ and $\overline{q}$.

(5) Results and comparison for the Wangara study of two surface bulk transfer coefficients, one dependent on the surface velocity and the other on the turbulence kinetic energy.

(6) A two-layer model which predicts $\bar{\theta}$ and $\bar{q}$ at two levels.

(7) Equations that determine the upward turbulent fluxes of θ and q in the interior of the PBL. These equations are used to obtain $\bar{\theta}$ and $\bar{q}$ in the two-layer model.

ACKNOWLEDGMENTS

I would like to express my sincere appreciation to Dr. David Randall, Dr. Wayne Schubert, Cindy Carrick, Douglas Cripe, Don Dazlich, Scott Denning, Jerry Harrington, Ross Heikes, and Debra Youngblood for their assistance in preparing this thesis.

I also want to thank my wife, Darleen, for putting up with me during the past 18 months. Her inspiration kept me going during those rough moments.

TABLE OF CONTENTS

1. Introduction

1.a. Statement of Problem

The planetary boundary layer (PBL) exerts a significant influence on the earth's weather and climate. The large-scale atmosphere feels the effects of the PBL during the development and growth of thunderstorms with relatively short time scales ($\approx$ 1 hour), and over the entire time scale spectrum including long periods (10's - 100's of years) when global climatic change occurs. The predominant source of energy to drive the general circulation is the ocean. Surface fluxes of heat, moisture, and momentum over the oceans are transported to the free atmosphere through the PBL. These fluxes play a vital role in transforming the earth's climate over time. The turbulent eddies in the PBL are the means by which this energy is transmitted from the ocean to the free atmosphere where it interacts with the general circulation. Since the PBL is intimately tied to the evolution of the climate, an accurate representation of the PBL is required to correctly make predictions of the future climate using a general circulation model. The only way to accomplish this is to develop a model that predicts the state of the PBL using parameterizations.

The surface fluxes of heat, moisture, and momentum are not the only important parameters to consider. The fluxes of these quantities over the entire depth of the PBL should also be included because they affect the general circulation. The total water vapor in the PBL represents the latent heat available to drive the general circulation. Another parameter, the PBL depth, besides denoting the amount of mass contained within the PBL, gives insight into whether clouds are present. As the PBL depth increases, moisture can penetrate higher into the atmosphere, eventually reaching the lifting condensation level where clouds will form. Finally, one can obtain some information about the fractional cloud amount by predicting the fractional area in the PBL that rising motion covers. Clouds play a key role in the climate because they affect the radiation budget by reflecting solar radiation that the earth's surface would otherwise absorb, therefore, knowledge of the amount of cloud coverage is crucial to climate prediction.

1

1.b. Definition of Second-Order Bulk Boundary Layer Model

The bulk boundary layer model presented is further development of the work completed by Randall, Shao, and Moeng(1992). The model is 1-dimensional and employs a second-order turbulence closure, and a "bulk" approach to parametrically represent boundary-layer structure. Prediction equations are used to compute the boundary layer depth (Δp_m, in terms of pressure), mixed layer values of u- and v-momentum (u_m and v_m), potential temperature (θ_m), mixing ratio (q_m), and turbulence kinetic energy (e_m). This model also diagnoses the entrainment rate (E) and fractional area covered by rising motion (σ), which allows the determination of fractional cloud amounts. Figure 1.b.1 depicts the domain of the model. Subscript S- denotes the earth's surface, S the top of the ventilation or surface layer, B the base of the entrainment layer or the top of the PBL, and B+ the top of the entrainment layer or the level just above the top of the PBL. Both the surface and entrainment layers are infinitesimally thick (indicated by the stippling in figure 1.b.1).
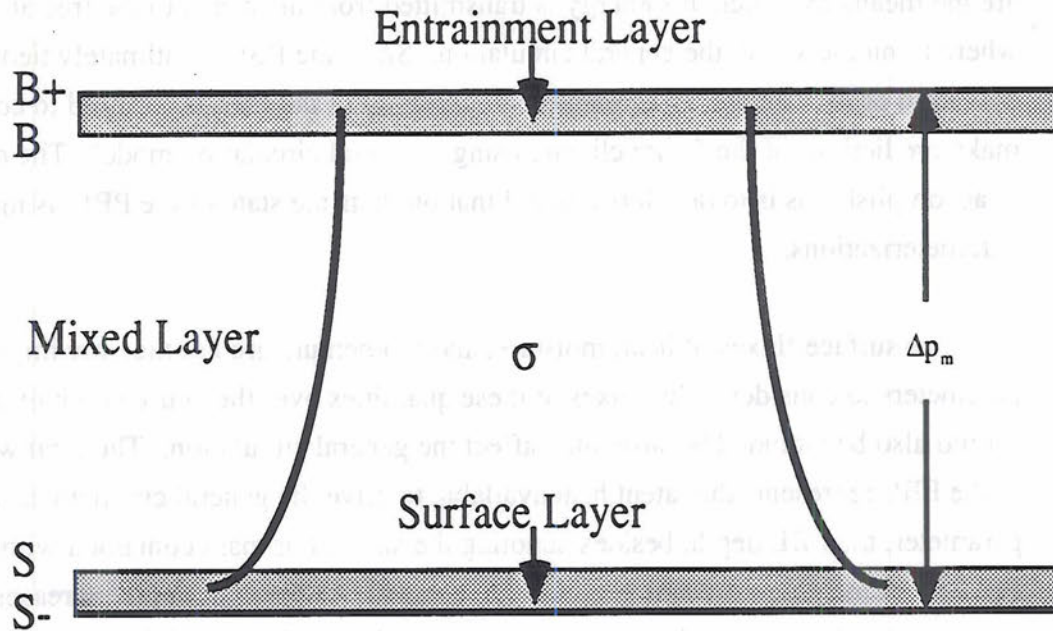
Figure 1.b.1: Domain of Bulk Boundary Layer Model.

1.c. Literature Review

Deardorff (1974a) completed a three-dimensional numerical study of the heated PBL where he determined the mean structure and height of the PBL. His study utilized data from Day 33 of the Wangara Experiment: Boundary Layer Data (Clarke et al., 1971). His model included grid-volume averaged equations for the momentum, potential temperature, and mixing ratio. The potential temperature equation included a term for the temperature change due to the divergence of the long-wave radiative flux. Deardorff also utilized subgrid transport equations ($\frac{\partial}{\partial t}\overline{u_i'u_j'}$, $\frac{\partial}{\partial t}\overline{u_i'\theta'}$, $\frac{\partial}{\partial t}\overline{u_i'q'}$, $\frac{\partial}{\partial t}\overline{\theta'^2}$, $\frac{\partial}{\partial t}\overline{\theta'q'}$, and $\frac{\partial}{\partial t}\overline{q'^2}$) for the subgrid Reynolds stresses. He assumed that the terrain was flat and the surface temperature and surface roughness were horizontally homogeneous.

The surface momentum flux was prescribed using the surface-layer formulations of Businger et al. (1971) and the surface layer integrals of Paulson (1970). The surface heat and moisture fluxes were computed using the subgrid transport equations. The model was initialized using data beginning at 0900L on Day 33.

Deardorff's model overestimated the calculated rate of growth of the mixed layer height between 1200-1500L. He attributed this overestimation to the lack of large-scale vertical motion in the model. Thus, the model mixed layer height was also overestimated during the afternoon. At 1200L the model predicted 1030 meters, while the actual height was 1010 meters. At 1500, the model height was 1400 meters and the actual height was only 1200 meters. The maximum model height was 1500 meters at 1800L and the maximum actual height was 1280 meters.

Yamada and Mellor (1975) completed a simulation of the diurnally varying planetary boundary layer and compared it with Days 33-34 of the Wangara data. Their model differed from Deardorff's by using ensemble mean closure instead of subgrid-scale closure. They used their level 3 model which required the solution of only 2 out of 10 differential equations for turbulence moments (turbulence kinetic energy and temperature variance).

Yamada's model underestimated the height of the PBL by about 300 meters during the afternoon hours. This discrepancy was due to the uncertainty in the observed values of the mean vertical wind. They concluded that accurate data for the thermal wind and

3

mean vertical wind are necessary to obtain realistic simulations for the mean winds and temperature.

Suarez et al. (1983) developed a parameterization for the PBL to be used in the UCLA General Circulation Model. Their work provides some of the basis for this thesis. The parameterization used a mixed-layer approach where the discontinuities in temperature and moisture at the top of the PBL were modeled using jumps. They utilized a modified σ-coordinate and bulk equations for the PBL.

Based on the earlier work by Deardorff (1970, 1972, and 1974a,b), the PBL depth was determined using a prognostic equation. Deardorff showed that entrainment was vitally important in the determination of the PBL depth and that the PBL depth affected the bulk Richardson number, which in turn was related to the stability dependence of the surface transfer coefficients.

The modified σ-coordinate was used to allow the varying depth of the PBL to be included into the GCM. In the conventional σ-coordinate system, surfaces follow the earth's topography. In the modified σ-coordinate system, the earth's surface and the PBL top are both coordinate surfaces. This allowed the PBL to be more effectively coupled to the large-scale dynamics. Also, the detailed structure that occurs at the PBL top where the jumps are did not have to be resolved by the GCM grid since the structure was at the interface of the two lowest GCM layers in the modified σ-coordinate system.

The bulk equations at the PBL top related the flux of a quantity to the product of the entrainment rate and the change (jump) of the quantity across the top interface. Surface bulk formula were determined using similarity theory formulated by Businger et al. (1971), just as Deardorff used. Since the fluxes at the PBL top use the entrainment rate, it had to be parameterized in terms of the prognostic variables. This parameterization was based on separating the buoyancy and shear terms into positive and negative production. The entrainment rate was then given by positive production minus negative production minus dissipation.

Randall et al. (1992) developed a second-order bulk boundary-layer model. This model matches the fluxes associated with the convective mass flux with the surface or ventilation mass flux and the entrainment mass flux. The model also provides the first

physically based means to determine the fractional area covered by rising motion, σ. Finally, the model allows the "well-mixed" assumption to be relaxed.

This thesis is a continuation of the work done by Randall et al. (1992). A new entrainment parameterization is introduced based on the sums of the buoyancy and shear production terms. A surface transfer coefficient is calculated based on the predicted turbulence kinetic energy. Results are shown using the diagnostics developed in Randall's bulk model including the convective mass flux and the fractional area covered by rising motion. Finally, a two-layer model is developed and tested.

2. Description of One-Layer Model

2.a. Equations

This chapter provides detailed derivations of the prediction equations used by the model. Table 2.a.1 provides a summary of the final equations used, the assumptions made in the derivations, and the boundary conditions applied to simplify and solve the prognostic equations.

Tensor notation is used throughout the derivations with the subscript j referring to one of the components of momentum or Cartesian coordinates ($u=u_1$, $v=u_2$, $w=u_3$, $x=x_1$, $y=x_2$, $z=x_3$, where subscripts i, j, or k are used with the values 1, 2, or 3).

Table 2.a.1: Model Equation Summary.

Equation	Assumptions	Top B.C.	Surface B.C.
Conservation of Mass (2.a.1) $$\frac{\partial(\Delta p_m)}{\partial t} = -\nabla \bullet (\Delta p_m v_m) + gE$$			
u-Momentum (2.a.2) $$\frac{\partial u_m}{\partial t} = \frac{E(u_{B+} - u_m)}{\rho_m \Delta z_m} - $$ $$\frac{\rho_{sfc} a^2 F_{mom}|v_m|u_m}{\rho_m \Delta z_m} + $$ $$f(v_m - v_g)$$	• Boussinesq • Shallow convection • Viscous effects ignored • $\frac{\partial}{\partial x}$ and $\frac{\partial}{\partial y}$ of perturbation quantities zero • Mixed layer values of v, ρ, and Δz used • Horizontal homogeneity	• Turbulence vanishes • Momentum flux vanishes • Momentum flux at level B vanishes if E<0	• Horizontal homogeneity • No mass crosses earth's surface • Louis (1979) surface momentum flux parameterization
v-Momentum (2.a.3) $$\frac{\partial v_m}{\partial t} = \frac{E(v_{B+} - v_m)}{\rho_m \Delta z_m} - $$ $$\frac{\rho_{sfc} a^2 F_{mom}|v_m|v_m}{\rho_m \Delta z_m} - $$ $$f(u_m - u_g)$$	• Same as u-momentum equation	• Same as u-momentum equation	• Same as u-momentum equation

Equation	Assumptions	Top B.C.	Surface B.C.
Potential Temperature (2.a.4) $$\frac{\partial \theta_m}{\partial t} = \frac{E(\overline{\theta}_{B+} - \theta_m)}{\rho_m \Delta z_m} + \frac{\rho_{sfc} a^2 |v_m| F_{heat-moist.}}{0.74 \rho_m \Delta z_m}(\overline{\theta}_{S-} - \theta_m)$$	• Same as momentum equations except: • Molecular conduction and radiation divergence ignored • Mixed layer value of θ also used • No phase changes of water	• Turbulence vanishes • Heat flux vanishes • Heat flux at level B vanishes if E<0	• Same as momentum equations except: • Louis (1979) surface heat-moisture flux parameterization
Moisture (2.a.5) $$\frac{\partial q_m}{\partial t} = \frac{E(\overline{q}_{B+} - q_m)}{\rho_m \Delta z_m} + \frac{\rho_{sfc} a^2 |v_m| F_{heat-moist.}}{0.74 \rho_m \Delta z_m}(\overline{q}_{S-} - q_m)$$	• Same as momentum equations except: • Source-sink term assumed to be a mean forcing and equal to zero • Molecular diffusion ignored • Mixed layer value of q also used • No clouds	• Turbulence vanishes • Moisture flux vanishes • Moisture flux at level B vanishes if E<0	• Same as potential temperature

Equation	Assumptions	Top B.C.	Surface B.C.
TKE (E>0) (2.a.6) $$\frac{\partial e_m}{\partial t} = \frac{g}{\Delta p_m}\left(S + B - Ee_m - D\right)$$	• Same as momentum equations except: • Viscous dissipation term approximated • Gravity waves neglected • Mixed layer value of TKE also used • $(F_v)_{S_-}$ constant in surface layer and is parallel to wind • F_v decreases linearly in entrainment layer and is parallel to wind • $\theta_m \cong \bar{\theta}_v$ • $F_{sv} \cong \dfrac{c_p TF_{\theta_v}}{\theta_m}$ • Ratio of F_{sv} and pressure approximately linear • $\sigma^2 = \dfrac{e_m}{a_1}$ (second order closure)	• TKE vanishes • Vertical turbulent flux of TKE at top equal to value at surface • Pressure correlation at top zero (due to neglect of gravity waves) • Vector momentum, heat, and moisture fluxes vanish	• No mass crosses earth's surface • Vertical turbulent flux of TKE at surface equal to value at top • Pressure correlation at surface zero (turbulence vanishes) • Vector momentum flux constant in surface layer and is parallel to wind • Momentum vanishes • Horizontal homogeneity • Louis (1979) surface heat-moisture flux parameterization

Table 2.a.1: Model Equation Summary (continued).

Equation	Assumptions	Top B.C.	Surface B.C.
TKE (E<0) (2.a.7) $$\frac{\partial e_m}{\partial t} = \frac{g}{\Delta p_m} weight\left(B_0 + S_0 - D\right)$$	• Same as TKE (E>0) except: • Production of TKE weighted based on contribution due to local change and entrainment production	Same as TKE (E>0) except: • Vector momentum, heat, and moisture fluxes vanish at level B and above since E<0	• Same as TKE (E>0)
Positive Entrainment (2.a.8) $$E = \rho_B \sqrt{e_m} \frac{b_1}{\left(1 + b_2 Ri\right)}$$	• No clouds • Turbulence required to mix newly entrained air • Balance between buoyant production and dissipation of TKE		
Negative Entrainment (2.a.9) $$E = \frac{\left(1 - weight\right)}{e_m}\left(B_0 + S_0 - D\right)$$	• No clouds • Turbulence required to mix newly entrained air • Local rate of change of TKE neglected		

2.a.(1) Conservation of Mass

The mass conservation equation is expressed by

$$\frac{\partial \rho}{\partial t} + \frac{\partial\left(\rho u_j\right)}{\partial x_j} = 0.$$

(2.a.(1).1)

This equation is not used directly (the form of this equation listed in Table 2.a.1 is used to predict the boundary layer depth), but is used to derive the other conservation equations.

2.a.(2) Conservation of Momentum

The Navier-Stokes equation is

$$\frac{\partial u_i}{\partial t} + u_j \frac{\partial u_i}{\partial x_j} = -\delta_{i3}g + f\varepsilon_{ij3}u_j - \frac{1}{\rho}\frac{\partial p}{\partial x_i} + \frac{\mu}{\rho}\frac{\partial^2 u_i}{\partial x_j^2} + \frac{(\lambda+\mu)}{\rho}\frac{\partial}{\partial x_i}\frac{\partial u_j}{\partial x_j}, \qquad (2.a.(2).1)$$

where f is the coriolis parameter ($2\Omega\sin\phi$), ε_{ij3} is the alternating unit tensor where

$$\varepsilon_{ij3} = \begin{cases} +1 \text{ for } i = 1 \text{ and } j = 2 \\ -1 \text{ for } i = 2 \text{ and } j = 1 \\ 0 \text{ for } i = j, \end{cases}$$

μ is the dynamic viscosity coefficient, ρ is the density, and $\lambda=-2\mu/3$. The incompressible form of (2.a.(2).1) is

$$\frac{\partial u_i}{\partial t} + u_j \frac{\partial u_i}{\partial x_j} = -\delta_{i3}g + f\varepsilon_{ij3}u_j - \frac{1}{\rho}\frac{\partial p}{\partial x_i} + \frac{\mu}{\rho}\frac{\partial^2 u_i}{\partial x_j^2}. \qquad (2.a.(2).2)$$

Equation (2.a.(2).2) is multiplied by the density (split into mean and perturbation parts when multiplied by g, constant otherwise: the Boussinesq approximation) to give

$$\bar{\rho}\left(\frac{\partial u_i}{\partial t} + u_j \frac{\partial u_i}{\partial x_j} \right) = -\bar{\rho}\delta_{i3}g - \rho'\delta_{i3}g + \bar{\rho}f\varepsilon_{ij3}u_j - \frac{\partial p}{\partial x_i} + \mu\frac{\partial^2 u_i}{\partial x_j^2}. \qquad (2.a.(2).3)$$

Next, (2.a.(2).3) is divided by the mean density to obtain

$$\frac{\partial u_i}{\partial t} + u_j \frac{\partial u_i}{\partial x_j} = -\delta_{i3}g - \frac{\rho'}{\bar{\rho}}\delta_{i3}g + f\varepsilon_{ij3}u_j - \frac{1}{\bar{\rho}}\frac{\partial p}{\partial x_i} + v\frac{\partial^2 u_i}{\partial x_j^2}, \qquad (2.a.(2).4)$$

where $v \equiv \mu/\bar{\rho}$ is the kinematic viscosity. For shallow convection $\frac{\rho'}{\bar{\rho}} \cong -\frac{\theta_v'}{\theta_v}$. This approximation is then applied to (2.a.(2).4) which yields

11

$$\frac{\partial u_i}{\partial t} + u_j \frac{\partial u_i}{\partial x_j} = -\delta_{i3}\left[g - \left(\frac{\theta_v'}{\overline{\theta_v}}\right)g\right] + f\varepsilon_{ij3}u_j - \frac{1}{\rho}\frac{\partial p}{\partial x_i} + v\frac{\partial^2 u_i}{\partial x_j^2} \ . \tag{2.a.(2).5}$$

Now, equation (2.a.(2).5) is multiplied by $\overline{\rho}$ and is added to u_i multiplied by the continuity equation to get

$$\overline{\rho}\frac{\partial u_i}{\partial t} = -u_i\frac{\partial \overline{\rho}}{\partial t} - \overline{\rho}u_j\frac{\partial u_i}{\partial x_j} - u_i\frac{\partial(\overline{\rho}u_j)}{\partial x_j} - \overline{\rho}\delta_{i3}\left[g - \left(\frac{\theta_v'}{\overline{\theta_v}}\right)g\right]$$
$$+ \overline{\rho}f\varepsilon_{ij3}u_j - \overline{\rho}\frac{1}{\rho}\frac{\partial p}{\partial x_i} + \overline{\rho}v\frac{\partial^2 u_i}{\partial x_j^2}. \tag{2.a.(2).6}$$

Equation (2.a.(2).6) is then put into flux form,

$$\frac{\partial(\overline{\rho}u_i)}{\partial t} = -\frac{\partial(\overline{\rho}u_iu_j)}{\partial x_j} - \overline{\rho}\delta_{i3}\left[g - \left(\frac{\theta_v'}{\overline{\theta_v}}\right)g\right] + \overline{\rho}f\varepsilon_{ij3}u_j -$$
$$\overline{\rho}\frac{1}{\rho}\frac{\partial p}{\partial x_i} + \overline{\rho}v\frac{\partial^2 u_i}{\partial x_j^2}. \tag{2.a.(2).7}$$

Only the horizontal momentum equations (i=1, 2) are considered, the geostrophic wind definition is used, and viscous effects are ignored. Then, (2.a.(2).7) becomes

$$\frac{\partial(\overline{\rho}u_i)}{\partial t} = -\frac{\partial(\overline{\rho}u_iu_j)}{\partial x_j} + \overline{\rho}f\varepsilon_{ij3}\left[u_j - \left(u_j\right)_g\right], \tag{2.a.(2).8}$$

where the g subscript denotes a geostrophic wind component. The wind components are next split into mean and perturbation parts to give

$$\frac{\partial(\overline{\rho}\overline{u_i} + \overline{\rho}u_i')}{\partial t} = -\frac{\partial(\overline{\rho}\overline{u_i}\overline{u_j} + \overline{\rho}\overline{u_i}u_j' + \overline{\rho}u_i'\overline{u_j} + \overline{\rho}u_i'u_j')}{\partial x_j} +$$
$$\overline{\rho}f\varepsilon_{ij3}\left[\overline{u_j} + u_j' - \left(u_j\right)_g\right]. \tag{2.a.(2).9}$$

The split is not necessary for the geostrophic component since this component is a constant. Equation (2.a.(2).9) is then simplified using the method of Reynolds averaging.

12

Consider an instantaneous quantity, A, which is split into a mean and perturbation component ($\overline{A}$ and A'). The mean component of A represents either the time, space, or ensemble average of A, and the perturbation component represents positive or negative deviations from this average. If $A = \overline{A} + A'$, then $\overline{(A)} = \overline{(\overline{A} + A')}$, or $\overline{A} = \overline{A} + \overline{A'}$. The last equality can only be true if $\overline{A'} = 0$ This just states that the sum of positive deviations from the mean equals the absolute value of the sum of the negative deviations, thus the net sum of the deviations is zero. Reynolds averaging is accomplished by applying the above result to quantities split into mean and perturbation parts. Stull (1991) provides a detailed discussion of Reynolds averaging. Equation (2.a.(2).9) then becomes

$$\frac{\partial(\overline{\rho}\overline{u}_i)}{\partial t} = -\frac{\partial\left(\overline{\rho}\overline{u}_i\overline{u}_j + \overline{\rho}\overline{u'_i u'_j}\right)}{\partial x_j} + \overline{\rho}f\varepsilon_{ij3}\left[\overline{u}_j - \left(u_j\right)_g\right].$$

(2.a.(2).10)

The u-component of (2.a.(2).10) is

$$\frac{\partial(\overline{\rho}\overline{u})}{\partial t} = -\frac{\partial(\overline{\rho}\overline{u}\,\overline{u})}{\partial x} - \frac{\partial(\overline{\rho}\overline{u}\,\overline{v})}{\partial y} - \frac{\partial(\overline{\rho}\overline{u}\,\overline{w})}{\partial z} -$$
$$\frac{\partial\left(\overline{\rho}\overline{u'u'}\right)}{\partial x} - \frac{\partial\left(\overline{\rho}\overline{u'v'}\right)}{\partial y} - \frac{\partial\left(\overline{\rho}\overline{u'w'}\right)}{\partial z} + \overline{\rho}f\left(\overline{v} - v_g\right).$$

(2.a.(2).11)

Horizontal derivatives of perturbation quantities are neglected because $\Delta x \approx \Delta y \gg \Delta z$,   thus $\dfrac{\Delta(\text{horizontal flux})}{\Delta x, \Delta y} \ll \dfrac{\Delta(\text{vertical flux})}{\Delta z}$. Equation (2.a.(2).11), without these terms, is next vertically integrated from the lower surface in the boundary layer, z_{S-}, to just above the boundary layer top, z_{B+} which yields

$$\int_{z=z_{S-}}^{z=z_{B+}} \frac{\partial(\overline{\rho}\overline{u})}{\partial t}\,dz = -\int_{z=z_{S-}}^{z=z_{B+}} \frac{\partial(\overline{\rho}\overline{u}\,\overline{u})}{\partial x}\,dz - \int_{z=z_{S-}}^{z=z_{B+}} \frac{\partial(\overline{\rho}\overline{u}\,\overline{v})}{\partial y}\,dz -$$
$$\int_{z=z_{S-}}^{z=z_{B+}} \frac{\partial(\overline{\rho}\overline{u}\,\overline{w})}{\partial z}\,dz - \int_{z=z_{S-}}^{z=z_{B+}} \frac{\partial\left(\overline{\rho}\overline{u'w'}\right)}{\partial z}\,dz +$$
$$\int_{z=z_{S-}}^{z=z_{B+}} \overline{\rho}f\left(\overline{v} - v_g\right)dz.$$

(2.a.(2).12)

Equation (2.a.(2).12) is then transformed using Leibniz's rule to give

$$\frac{\partial}{\partial t}\int_{z=z_{S-}}^{z=z_{B+}}\overline{\rho}\,\overline{u}\,dz = \overline{\rho}(t,\,z_{B+})\overline{u}(t,\,z_{B+})\frac{\partial z_{B+}}{\partial t} - \overline{\rho}(t,\,z_{S-})\overline{u}(t,\,z_{S-})\frac{\partial z_{S-}}{\partial t}$$

$$-\frac{\partial}{\partial x}\int_{z=z_{S-}}^{z=z_{B+}}\overline{\rho}\,\overline{u}\,\overline{u}\,dz + \overline{\rho}(t,\,z_{B+})\overline{u}(t,\,z_{B+})\overline{u}(t,\,z_{B+})\frac{\partial z_{B+}}{\partial x} -$$

$$\overline{\rho}(t,\,z_{S-})\overline{u}(t,\,z_{S-})\overline{u}(t,\,z_{S-})\frac{\partial z_{S-}}{\partial x} - \frac{\partial}{\partial y}\int_{z=z_{S-}}^{z=z_{B+}}\overline{\rho}\,\overline{u}\,\overline{v}\,dz +$$

$$\overline{\rho}(t,\,z_{B+})\overline{u}(t,\,z_{B+})\overline{v}(t,\,z_{B+})\frac{\partial z_{B+}}{\partial y} -$$

$$\overline{\rho}(t,\,z_{S-})\overline{u}(t,\,z_{S-})\overline{v}(t,\,z_{S-})\frac{\partial z_{S-}}{\partial y} -$$

$$\overline{\rho}(t,\,z_{B+})\overline{u}(t,\,z_{B+})\overline{w}(t,\,z_{B+}) +$$ (2.a.(2).13)

$$\overline{\rho}(t,\,z_{S-})\overline{u}(t,\,z_{S-})\overline{w}(t,\,z_{S-}) - \overline{\rho}(t,\,z_{B+})\overline{u'w'}(t,\,z_{B+}) +$$

$$\overline{\rho}(t,\,z_{S-})\overline{u'w'}(t,\,z_{S-}) + \rho_m f(v_m - v_g)\Delta z_m,$$

where the mixed layer values (denoted by subscript m) of v (the v-component of the wind), the density, and the boundary layer depth have been used to simplify the integration. Since turbulence vanishes above the boundary layer, $\overline{\rho}(t,\,z_{B+})\overline{u'w'}(t,\,z_{B+})$ is zero.

Next, the terms at height B+ and at height S- are combined to give

$$\frac{\partial}{\partial t}\int_{z=z_{S-}}^{z=z_{B+}}\overline{\rho}\,\overline{u}\,dz = \overline{u}\left[\overline{\rho}\left(\frac{\partial z_{B+}}{\partial t} + \overline{u}\frac{\partial z_{B+}}{\partial x} + \overline{v}\frac{\partial z_{B+}}{\partial y} - \overline{w}\right)\right] -$$

$$\overline{u}\left[\overline{\rho}\left(\frac{\partial z_{S-}}{\partial t} + \overline{u}\frac{\partial z_{S-}}{\partial x} + \overline{v}\frac{\partial z_{S-}}{\partial y} - \overline{w}\right)\right]$$ (2.a.(2).14)

$$-\frac{\partial}{\partial x}\int_{z=z_{S-}}^{z=z_{B+}}\overline{\rho}\,\overline{u}\,\overline{u}\,dz - \frac{\partial}{\partial y}\int_{z=z_{S-}}^{z=z_{B+}}\overline{\rho}\,\overline{u}\,\overline{v}\,dz +$$

$$\left(\overline{\rho}\overline{u'w'}\right)_{S-} + \rho_m f(v_m - v_g)\Delta z_m,$$

where the function notation has been dropped. The terms inside the square brackets represent the entrainment mass flux, E, across the B+ and S- surfaces respectively. The S- surface is the earth's surface, where the entrainment mass flux is zero (the individual terms are not necessarily zero, but their sum must be zero since no mass can cross the

earth's surface). Equation (2.a.(2).14) then simplifies to

$$\frac{\partial}{\partial t} \int_{z=z_{S-}}^{z=z_{B+}} \overline{\rho u}\, dz = E\overline{u}_{B+} - \nabla \bullet \int_{z=z_{S-}}^{z=z_{B+}} \overline{u\rho v}\, dz + \left(\overline{\rho u' w'}\right)_{S-} + \rho_m f\left(v_m - v_g\right)\Delta z_m, \quad (2.a.(2).15)$$

where the second term on the right hand side is a combination of the fourth and fifth terms in equation (2.a.(2).14). Now, the first term and the divergence term are integrated using mixed layer values as was done for the coriolis term to give

$$\frac{\partial\left(\rho_m u_m \Delta z_m\right)}{\partial t} = E\overline{u}_{B+} - \nabla \bullet \left[u_m \rho_m v_m \Delta z_m\right] + \left(\overline{\rho u' w'}\right)_{S-} +$$
$$\rho_m f\left(v_m - v_g\right)\Delta z_m,$$

or

$$\rho_m \Delta z_m \frac{\partial u_m}{\partial t} = E\overline{u}_{B+} - u_m \frac{\partial\left(\rho_m \Delta z_m\right)}{\partial t} - \nabla \bullet \left(u_m \rho_m v_m \Delta z_m\right) +$$
$$\left(\overline{\rho u' w'}\right)_{S-} + \rho_m f\left(v_m - v_g\right)\Delta z_m, \quad (2.a.(2).16)$$

The derivative in the second term on the right hand side of the lower equation of (2.a.(2).16) can be expressed in terms of the entrainment mass flux into the top of the boundary layer. This is shown by Figure 2.a.(2).1.

(1) Entrainment brings mass into PBL top at local point

$(\rho_m \Delta z_m)_2$

Local Point

(2) Mass flux converges at local point

$(\rho_m \Delta z_m)_{local}$

V_m

$(\rho_m \Delta z_m)_1$

Area of more mass

Area of less mass

(3) Area containing more mass is advected into local point by the velocity
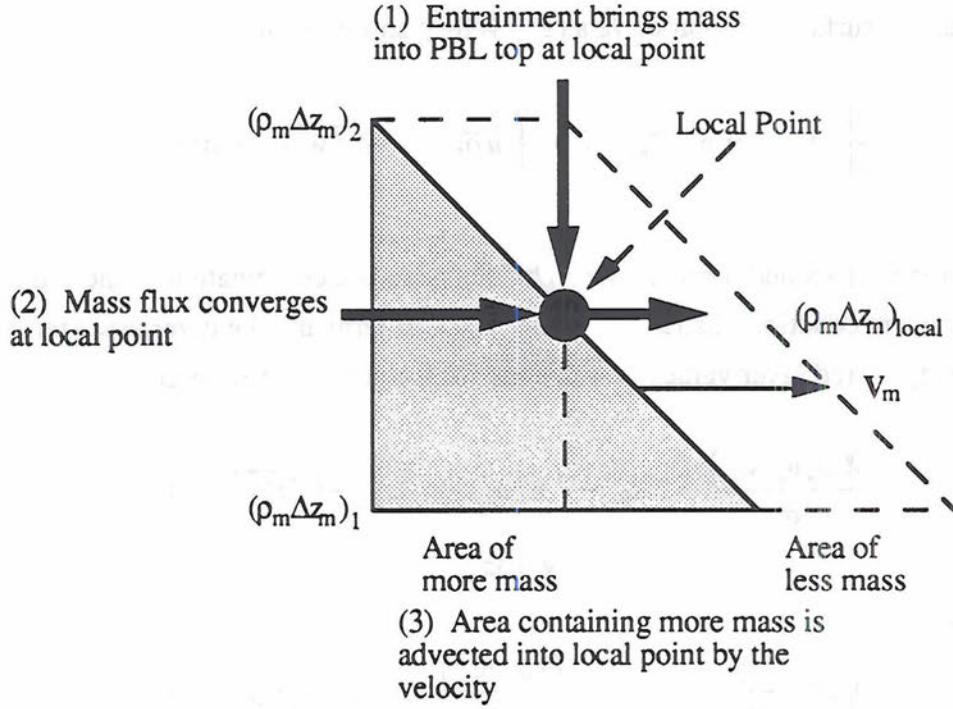
Figure 2.a.(2).1: Processes Which Cause Local Change in Mass.

The local mass flux ($(\rho_m \Delta z_m)_{local}$) changes due to: (1) the entrainment of mass into the PBL top (E), (2) horizontal convergence of mass flux ($-\rho_m \Delta z_m (\nabla \bullet v_m)_{local}$), and (3) horizontal advection of mass flux ($-v_m \bullet \nabla(\rho_m \Delta z_m)_{local}$). Therefore,

$\dfrac{\partial(\rho_m \Delta z_m)}{\partial t} = E - \rho_m \Delta z_m (\nabla \bullet v_m)_{local} - v_m \bullet \nabla(\rho_m \Delta z_m)_{local}$. Substituting this into the last equation of (2.a.(2).16) gives.

$$\rho_m \Delta z_m \frac{\partial u_m}{\partial t} = E\overline{u}_{B+} - u_m \left[E - \rho_m \Delta z_m (\nabla \bullet v_m) - v_m \bullet \nabla(\rho_m \Delta z_m) \right]$$
$$- \nabla \bullet (u_m \rho_m v_m \Delta z_m) + (\overline{\rho u'w'})_{S-} + \rho_m f(v_m - v_g) \Delta z_m,$$

or using the vector identity $u_m \nabla \bullet (\rho_m v_m \Delta z_m) = u_m \rho_m \Delta z_m (\nabla \bullet v_m) + u_m v_m \bullet \nabla(\rho_m \Delta z_m)$,

$$\rho_m \Delta z_m \frac{\partial u_m}{\partial t} = E\overline{u}_{B+} - Eu_m + u_m \nabla \bullet (\rho_m \Delta z_m v_m)$$
$$- \nabla \bullet (u_m \rho_m v_m \Delta z_m) + (\overline{\rho u'w'})_{S-} + \rho_m f(v_m - v_g) \Delta z_m,$$

or

16

$$\rho_m \Delta z_m \frac{\partial u_m}{\partial t} = E(\overline{u}_{B+} - u_m) + u_m \nabla \bullet (\rho_m v_m \Delta z_m) - u_m \nabla \bullet (\rho_m v_m \Delta z_m) -$$
$$\rho_m \Delta z_m v_m \bullet \nabla u_m + (\overline{\rho u'w'})_{S-} + \rho_m f(v_m - v_g) \Delta z_m,$$

or

$$\rho_m \Delta z_m \frac{\partial u_m}{\partial t} = E(\overline{u}_{B+} - u_m) - \rho_m \Delta z_m v_m \bullet \nabla u_m + (\overline{\rho u'w'})_{S-}$$
$$+ \rho_m f(v_m - v_g) \Delta z_m. \tag{2.a.(2).17}$$

Horizontal homogeneity is assumed in the last equation of (2.a.(2).17). This eliminates the second term on the right hand side. Then this equation is divided by the mixed layer density and boundary layer depth to give

$$\frac{\partial u_m}{\partial t} = \frac{E(\overline{u}_{B+} - u_m)}{\rho_m \Delta z_m} + \frac{(\overline{\rho u'w'})_{S-}}{\rho_m \Delta z_m} + f(v_m - v_g). \tag{2.a.(2).18}$$

The local rate of change of the mixed layer u-momentum component is due to the entrainment flux of momentum through the boundary layer top, the surface flux of momentum, coriolis-pressure gradient effects, and momentum divergence. The v-component equation is derived in the same manner and is

$$\frac{\partial v_m}{\partial t} = \frac{E(\overline{v}_{B+} - v_m)}{\rho_m \Delta z_m} + \frac{(\overline{\rho v'w'})_{S-}}{\rho_m \Delta z_m} - f(u_m - u_g). \tag{2.a.(2).19}$$

Chapter 3 provides details of the parameterization of the surface momentum fluxes.

The equations with the included parameterization are

$$\frac{\partial u_m}{\partial t} = \frac{E(u_{B+} - u_m)}{\rho_m \Delta z_m} - \frac{\rho_{sfc} a^2 F_{mom} |v_m| u_m}{\rho_m \Delta z_m} + f(v_m - v_g), \tag{2.a.(2).20}$$

and

$$\frac{\partial v_m}{\partial t} = \frac{E(v_{B+} - v_m)}{\rho_m \Delta z_m} - \frac{\rho_{sfc} a^2 F_{mom} |v_m| v_m}{\rho_m \Delta z_m} - f(u_m - u_g), \tag{2.a.(2).21}$$

17

where ρ_{sfc} is the surface air density, a^2 is a drag coefficient, F_{mom} is an empirical function which is dependent on a bulk Richardson number, and $|v_m|$ is the magnitude of the mixed layer horizontal velocity ($|v_m| = (u_m^2 + v_m^2)^{1/2}$).

2.a.(3) Conservation of Potential Temperature

The conservation equation for moist static energy is

$$\frac{\partial h}{\partial t} + u_j \frac{\partial h}{\partial x_j} = v_h \frac{\partial^2 h}{\partial x_j^2} - \frac{1}{\bar{\rho} c_p} \frac{\partial Q_j}{\partial x_j},$$ (2.a.(3).1)

where $h = c_p T + gz + L_v q$ is moist static energy (L_v is latent heat of vaporization of water and q is the water vapor mixing ratio), v_h is the kinematic molecular diffusivity for moist static energy, c_p the specific heat for moist air at constant pressure, and Q_j the component of net radiation in the jth direction. This equation is then multiplied by the mean density and is added to the product of h and the continuity equation which gives

$$\bar{\rho} \frac{\partial h}{\partial t} + h \frac{\partial \bar{\rho}}{\partial t} = -\bar{\rho} u_j \frac{\partial h}{\partial x_j} - h \frac{\partial (\bar{\rho} u_j)}{\partial x_j} + \bar{\rho} v_h \frac{\partial^2 h}{\partial x_j^2} - \frac{1}{c_p} \frac{\partial Q_j}{\partial x_j}.$$ (2.a.(3).2)

Now, equation (2.a.(3).2) is put into flux form,

$$\frac{\partial (\bar{\rho} h)}{\partial t} = -\frac{\partial (\bar{\rho} u_j h)}{\partial x_j} + \bar{\rho} v_h \frac{\partial^2 h}{\partial x_j^2} - \frac{1}{c_p} \frac{\partial Q_j}{\partial x_j}.$$ (2.a.(3).3)

Next, equation (2.a.(3).3) is expanded into mean and perturbation parts to give

$$\frac{\partial (\bar{\rho} \bar{h})}{\partial t} + \frac{\partial (\bar{\rho} h')}{\partial t} = -\frac{\partial (\bar{\rho} \bar{u}_j \bar{h})}{\partial x_j} - \frac{\partial (\bar{\rho} \bar{u}_j h')}{\partial x_j} - \frac{\partial (\bar{\rho} u'_j \bar{h})}{\partial x_j} - \frac{\partial (\bar{\rho} u'_j h')}{\partial x_j} +$$
$$\bar{\rho} v_h \frac{\partial^2 \bar{h}}{\partial x_j^2} + \bar{\rho} v_h \frac{\partial^2 h'}{\partial x_j^2} - \frac{1}{c_p} \frac{\partial \bar{Q}_j}{\partial x_j} - \frac{1}{c_p} \frac{\partial Q'_j}{\partial x_j}.$$ (2.a.(3).4)

After Reynolds averaging, equation (2.a.(3).4) becomes

18

$$\frac{\partial\left(\overline{\rho}\overline{h}\right)}{\partial t} = -\frac{\partial\left(\overline{\rho}\overline{u}_j\overline{h}\right)}{\partial x_j} - \frac{\partial\left(\overline{\rho}\overline{u'_j h'}\right)}{\partial x_j} + \overline{\rho}v_h\frac{\partial^2\overline{h}}{\partial x_j^2} + -\frac{1}{c_p}\frac{\partial\overline{Q}_j}{\partial x_j}.$$ (2.a.(3).5)

The horizontal derivatives of the perturbation quantities are neglected using the same scaling argument presented in section 2.a.(2), then equation (2.a.(3).5) is vertically integrated ignoring molecular conduction and radiation divergence which gives

$$\int_{z=z_{S-}}^{z=z_{B+}}\frac{\partial\left(\overline{\rho}\overline{h}\right)}{\partial t}dz = -\int_{z=z_{S-}}^{z=z_{B+}}\frac{\partial\left(\overline{\rho}\overline{u}\overline{h}\right)}{\partial x}dz - \int_{z=z_{S-}}^{z=z_{B+}}\frac{\partial\left(\overline{\rho}\overline{v}\overline{h}\right)}{\partial y}dz - \int_{z=z_{S-}}^{z=z_{B+}}\frac{\partial\left(\overline{\rho}\overline{w}\overline{h}\right)}{\partial z}dz$$
$$-\int_{z=z_{S-}}^{z=z_{B+}}\frac{\partial\left(\overline{\rho}\overline{w'h'}\right)}{\partial z}dz.$$ (2.a.(3).6)

Leibniz's rule is then applied to (2.a.(3).6) to yield

$$\frac{\partial}{\partial t}\int_{z=z_{S-}}^{z=z_{B+}}\overline{\rho}\overline{h}dz = \overline{\rho}\overline{h}\frac{\partial z_{B+}}{\partial t} - \overline{\rho}\overline{h}\frac{\partial z_{S-}}{\partial t} - \frac{\partial}{\partial x}\int_{z=z_{S-}}^{z=z_{B+}}\overline{\rho}\overline{u}\overline{h}dz + \overline{\rho}\overline{u}\overline{h}\frac{\partial z_{B+}}{\partial x} -$$
$$\overline{\rho}\overline{u}\overline{h}\frac{\partial z_{S-}}{\partial x} - \frac{\partial}{\partial y}\int_{z=z_{S-}}^{z=z_{B+}}\overline{\rho}\overline{v}\overline{h}dz + \overline{\rho}\overline{v}\overline{h}\frac{\partial z_{B+}}{\partial y} - \overline{\rho}\overline{v}\overline{h}\frac{\partial z_{S-}}{\partial y} -$$
$$\overline{\rho}\overline{w}\overline{h}\left(t, z_{B+}\right) + \overline{\rho}\overline{w}\overline{h}\left(t, z_{S-}\right) - \overline{\rho}\overline{w'h'}\left(t, z_{B+}\right) +$$
$$\overline{\rho}\overline{w'h'}\left(t, z_{S-}\right).$$ (2.a.(3).7)

The second to last term in (2.a.(3).7) is zero because turbulence goes to zero above the boundary layer. The terms at the bottom and top of the boundary layer are then combined to give

$$\frac{\partial}{\partial t}\int_{z=z_{S-}}^{z=z_{B+}}\overline{\rho}\overline{h}dz = \overline{h}\left[\overline{\rho}\left(\frac{\partial z_{B+}}{\partial t} + \overline{u}\frac{\partial z_{B+}}{\partial x} + \overline{v}\frac{\partial z_{B+}}{\partial y} - \overline{w}\right)\right] -$$
$$\overline{h}\left[\overline{\rho}\left(\frac{\partial z_{S-}}{\partial t} + \overline{u}\frac{\partial z_{S-}}{\partial x} + \overline{v}\frac{\partial z_{S-}}{\partial y} - \overline{w}\right)\right] -$$
$$\frac{\partial}{\partial x}\int_{z=z_{S-}}^{z=z_{B+}}\overline{\rho}\overline{u}\overline{h}dz - \frac{\partial}{\partial y}\int_{z=z_{S-}}^{z=z_{B+}}\overline{\rho}\overline{v}\overline{h}dz + \left(\overline{\rho}\overline{w'h'}\right)_{S-}.$$ (2.a.(3).8)

19

As described in the previous section, the terms in the brackets represent the entrainment mass flux across the PBL top and surface respectively (where the surface terms add to zero because no mass can cross the earth's surface). The horizontal derivative terms are combined as in the last section, and then equation (2.a.(3).8) reduces to

$$\frac{\partial}{\partial t}\int_{z=z_{s-}}^{z=z_{B+}}\overline{\rho}\overline{h}\,dz = E\overline{h}_{B+} - \nabla \bullet \int_{z=z_{s-}}^{z=z_{B+}}\overline{h}\,\overline{\rho}\,\overline{v}\,dz + \left(\overline{\rho w'h'}\right)_{s-}. \qquad (2.a.(3).9)$$

The integrals are then evaluated using mixed layer values,

$$\frac{\partial(\rho_m h_m \Delta z_m)}{\partial t} = E\overline{h}_{B+} - \nabla \bullet \left(h_m \rho_m v_m \Delta z_m\right) + \left(\overline{\rho w'h'}\right)_{s-},$$

or

$$\rho_m \Delta z_m \frac{\partial h_m}{\partial t} = E\overline{u}_{B+} - h_m \frac{\partial(\rho_m \Delta z_m)}{\partial t} - \nabla \bullet \left(h_m \rho_m v_m \Delta z_m\right) +$$
$$\left(\overline{\rho w'h'}\right)_{s-},$$

or employing the same vector identity and expression for the entrainment used to obtain equation (2.a.(2).17),

$$\rho_m \Delta z_m \frac{\partial h_m}{\partial t} = E\left(\overline{h}_{B+} - h_m\right) - \rho_m \Delta z_m v_m \bullet \nabla h_m + \left(\overline{\rho w'h'}\right)_{s-}. \qquad (2.a.(3).10)$$

Now, horizontal homogeneity is assumed in (2.a.(3).10) which eliminates the third term on the right hand side. Then the entrainment terms are combined, and the equation is divided by the mixed layer density and boundary layer depth which gives

$$\frac{\partial h_m}{\partial t} = \frac{E\left(\overline{h}_{B+} - h_m\right)}{\rho_m \Delta z_m} + \frac{\left(\overline{\rho w'h'}\right)_{s-}}{\rho_m \Delta z_m}. \qquad (2.a.(3).11)$$

The equation for the mixed layer potential temperature (with no phase changes of water) is based on the above equation. It is obtained by replacing the moist static energy by the potential temperature and including the surface heat flux parameterization presented in Chapter 3 to give

$$\frac{\partial \theta_m}{\partial t} = \frac{E(\overline{\theta}_{B+} - \theta_m)}{\rho_m \Delta z_m} + \frac{\rho_{sfc} a^2 |v_m| F_{heat-moisture}}{0.74 \rho_m \Delta z_m}(\overline{\theta}_{S-} - \theta_m), \tag{2.a.(3).12}$$

where a^2 is the same drag coefficient used in (2.a.(2).20), $|v_m|$ is defined as in the previous section, and $F_{heat-moisture}$ is a similar function to F_{mom}.

2.a.(4) Conservation of Moisture

The conservation of total water is given by

$$\frac{\partial q_t}{\partial t} + u_j \frac{\partial q_t}{\partial x_j} = v_{q_t} \frac{\partial^2 q_t}{\partial x_j^2} + \frac{S_{q_t}}{\overline{\rho}}, \tag{2.a.(4).1}$$

where v_{q_t} is the molecular diffusivity for water and S_{q_t} is a net precipitation source-sink term. This equation is then multiplied by the mean density and is added to the product of q_t and the continuity equation to yield

$$\overline{\rho}\frac{\partial q_t}{\partial t} + q_t \frac{\partial \overline{\rho}}{\partial t} = -\overline{\rho}u_j \frac{\partial q_t}{\partial x_j} - q\frac{\partial(\overline{\rho}u_j)}{\partial x_j} + \overline{\rho}v_{q_t}\frac{\partial^2 q_t}{\partial x_j^2} + S_{q_t}. \tag{2.a.(4).2}$$

Equation (2.a.(4).2) is next put into flux form,

$$\frac{\partial(\overline{\rho}q_t)}{\partial t} = -\frac{\partial(\overline{\rho}u_j q_t)}{\partial x_j} + \overline{\rho}v_{q_t}\frac{\partial^2 q_t}{\partial x_j^2} + S_{q_t}. \tag{2.a.(4).3}$$

Equation (2.a.(4).3) after expanding into mean and perturbation quantities becomes

$$\frac{\partial(\overline{\rho}\overline{q}_t)}{\partial t} + \frac{\partial(\overline{\rho}q_t')}{\partial t} = -\frac{\partial(\overline{\rho}\overline{u}_j \overline{q}_t)}{\partial x_j} - \frac{\partial(\overline{\rho}\overline{u}_j q_t')}{\partial x_j} - \frac{\partial(\overline{\rho}u_j'\overline{q}_t)}{\partial x_j} - \frac{\partial(\overline{\rho}u_j' q_t')}{\partial x_j} +$$
$$\overline{\rho}v_{q_t}\frac{\partial^2 \overline{q}_t}{\partial x_j^2} + \overline{\rho}v_{q_t}\frac{\partial^2 q_t'}{\partial x_j^2} + S_{q_t}, \tag{2.a.(4).4}$$

where the source-sink term, S_{q_t}, is assumed to be a mean forcing. This equation is then Reynolds averaged to give

$$\frac{\partial(\overline{\rho}\overline{q_t})}{\partial t} = -\frac{\partial(\overline{\rho}\overline{u_j}\overline{q_t})}{\partial x_j} - \frac{\partial(\overline{\rho}\overline{u_j'q_t'})}{\partial x_j} + \overline{\rho}v_{q_t}\frac{\partial^2 \overline{q_t}}{\partial x_j^2} + S_{q_t}.$$ (2.a.(4).5)

Assuming $S_{q_t} = 0$ (no precipitation leaving or falling into an air parcel), neglecting molecular diffusion, and neglecting horizontal derivatives of perturbation terms, (2.a.(4).5) becomes, after vertical integration,

$$\int_{z=z_{s-}}^{z=z_{B+}}\frac{\partial(\overline{\rho}\overline{q_t})}{\partial t}dz = -\int_{z=z_{s-}}^{z=z_{B+}}\frac{\partial(\overline{\rho}\overline{u}\overline{q_t})}{\partial x}dz - \int_{z=z_{s-}}^{z=z_{B+}}\frac{\partial(\overline{\rho}\overline{v}\overline{q_t})}{\partial y}dz -$$

$$\int_{z=z_{s-}}^{z=z_{B+}}\frac{\partial(\overline{\rho}\overline{w}\overline{q_t})}{\partial z}dz - \int_{z=z_{s-}}^{z=z_{B+}}\frac{\partial(\overline{\rho}\overline{w'q_t'})}{\partial z}dz.$$ (2.a.(4).6)

This equation is analogous to (2.a.(3).6). Following the derivation from the previous section, (2.a.(4).6) simplifies to

$$\frac{\partial(q_t)_m}{\partial t} = \frac{E(\overline{q}_{B+}-(q_t)_m)}{\rho_m \Delta z_m} + \frac{(\overline{\rho}\overline{w'q_t'})_{s-}}{\rho_m \Delta z_m}.$$ (2.a.(4).7)

In the absence of clouds, $q_t = q$ (water vapor mixing ratio). Then, equation (2.a.(4).7) is used with q and the same parameterization for the surface moisture flux as was used for the surface heat flux, to give

$$\frac{\partial q_m}{\partial t} = \frac{E(\overline{q}_{B+}-q_m)}{\rho_m \Delta z_m} + \frac{\rho_{sfc}a^2|v_m|F_{heat-moisture}}{0.74\rho_m \Delta z_m}(\overline{q}_{s-}-q_m).$$ (2.a.(4).8)

2.a.(5) Turbulence Kinetic Energy (TKE) Equation

Equation (2.a.(2).5) is expanded into mean and perturbation parts (except for the $\left[g - \left(\frac{\theta_v'}{\overline{\theta}_v}\right)g\right]$ term which has already been expanded when making the Boussinesq approximation) to give

22

$$\frac{\partial(\overline{u}_i + u_i')}{\partial t} + \left(\overline{u}_j + u_j'\right)\frac{\partial(\overline{u}_i + u_i')}{\partial x_j} = -\delta_{i3}\left[g - \left(\frac{\theta_v'}{\overline{\theta}_v}\right)g\right] + f\varepsilon_{ij3}\left(\overline{u}_j + u_j'\right) -$$

$$\frac{1}{\overline{\rho}}\frac{\partial(\overline{p} + p')}{\partial x_i} + v\frac{\partial^2(\overline{u}_i + u_i')}{\partial x_j^2}.$$

(2.a.(5).1)

Equation (2.a.(5).1) is then algebraically expanded which yields

$$\frac{\partial\overline{u}_i}{\partial t} = -\frac{\partial u_i'}{\partial t} - \frac{\overline{u}_j\partial\overline{u}_i}{\partial x_j} - \frac{\overline{u}_j\partial u_i'}{\partial x_j} - \frac{u_j'\partial\overline{u}_i}{\partial x_j} - \frac{u_j'\partial u_i'}{\partial x_j} - \delta_{i3}g + \delta_{i3}\left(\frac{\theta_v'}{\overline{\theta}_v}\right)g +$$

$$f\varepsilon_{ij3}\overline{u}_j + f\varepsilon_{ij3}u_j' - \frac{1}{\overline{\rho}}\frac{\partial\overline{p}}{\partial x_i} - \frac{1}{\overline{\rho}}\frac{\partial p'}{\partial x_i} + v\frac{\partial^2\overline{u}_i}{\partial x_j^2} + v\frac{\partial^2 u_i'}{\partial x_j^2}.$$

(2.a.(5).2)

This equation is then Reynolds averaged and simplifies to

$$\frac{\partial\overline{u}_i}{\partial t} + \frac{\overline{u}_j\partial\overline{u}_i}{\partial x_j} + \frac{\overline{u_j'\partial u_i'}}{\partial x_j} = -\delta_{i3}g + f\varepsilon_{ij3}\overline{u}_j - \frac{1}{\overline{\rho}}\frac{\partial\overline{p}}{\partial x_i} + v\frac{\partial^2\overline{u}_i}{\partial x_j^2}.$$

(2.a.(5).3)

Next, the continuity equation for turbulent fluctuations is multiplied by u_i' and Reynolds averaged which gives $\overline{u_i'\frac{\partial u_j'}{\partial x_j}} = 0$. This term is added to the last term on the left hand side of (2.a.(5).3). This sum is then put into flux form,

$$\frac{\partial\overline{u}_i}{\partial t} + \frac{\overline{u}_j\partial\overline{u}_i}{\partial x_j} + \frac{\partial\left(\overline{u_i'u_j'}\right)}{\partial x_j} = -\delta_{i3}g + f\varepsilon_{ij3}\overline{u}_j - \frac{1}{\overline{\rho}}\frac{\partial\overline{p}}{\partial x_i} + v\frac{\partial^2\overline{u}_i}{\partial x_j^2}.$$

(2.a.(5).4)

Now, (2.a.(5).4) is subtracted from (2.a.(5).2) which leaves

$$\frac{\partial u_i'}{\partial t} = -\overline{u}_j\frac{\partial u_i'}{\partial x_j} - u_j'\frac{\partial\overline{u}_i}{\partial x_j} - u_j'\frac{\partial u_i'}{\partial x_j} + \delta_{i3}\left(\frac{\theta_v'}{\overline{\theta}_v}\right)g + f\varepsilon_{ij3}u_j' - \frac{1}{\overline{\rho}}\frac{\partial p'}{\partial x_i} +$$

$$v\frac{\partial^2 u_i'}{\partial x_j^2} + \frac{\partial\left(\overline{u_i'u_j'}\right)}{\partial x_j}.$$

(2.a.(5).5)

Equation (2.a.(5).5) is next multiplied by $\overline{\rho}2u_i'$ which gives

23

$$\bar{\rho}2u_i'\frac{\partial u_i'}{\partial t} = -\bar{\rho}2\bar{u}_j u_i'\frac{\partial u_i'}{\partial x_j} - \bar{\rho}2u_i'u_j'\frac{\partial \bar{u}_i}{\partial x_j} - \bar{\rho}2u_i'u_j'\frac{\partial u_i'}{\partial x_j} + \bar{\rho}2\delta_{i3}u_i'\left(\frac{\theta_v'}{\bar{\theta}_v}\right)g +$$

$$\bar{\rho}2f\varepsilon_{ij3}u_i'u_j' - \bar{\rho}2\frac{u_i'}{\bar{\rho}}\frac{\partial p'}{\partial x_i} + \bar{\rho}2vu_i'\frac{\partial^2 u_i'}{\partial x_j^2} + \bar{\rho}2u_i'\frac{\partial(\overline{u_i'u_j'})}{\partial x_j}. \qquad (2.a.(5).6)$$

The Reynolds averaged continuity equation, using mean density, is then multiplied by $(u_i')^2$ and added to (2.a.(5).6) which results in

$$\bar{\rho}2u_i'\frac{\partial u_i'}{\partial t} + (u_i')^2\frac{\partial\bar{\rho}}{\partial t} = -\bar{\rho}2\bar{u}_j u_i'\frac{\partial u_i'}{\partial x_j} - (u_i')^2\frac{\partial(\bar{\rho}\bar{u}_j)}{\partial x_j} - \bar{\rho}2u_i'u_j'\frac{\partial \bar{u}_i}{\partial x_j} -$$

$$\bar{\rho}2u_i'u_j'\frac{\partial u_i'}{\partial x_j} + \bar{\rho}2\delta_{i3}u_i'\left(\frac{\theta_v'}{\bar{\theta}_v}\right)g + \bar{\rho}2f\varepsilon_{ij3}u_i'u_j' - \qquad (2.a.(5).7)$$

$$\bar{\rho}2\frac{u_i'}{\bar{\rho}}\frac{\partial p'}{\partial x_i} + \bar{\rho}2vu_i'\frac{\partial^2 u_i'}{\partial x_j^2} + \bar{\rho}2u_i'\frac{\partial(\overline{u_i'u_j'})}{\partial x_j}.$$

Equation (2.a.(5).7) is then put into flux form,

$$\frac{\partial\left[\bar{\rho}(u_i')^2\right]}{\partial t} = -\frac{\partial\left[\bar{\rho}\bar{u}_j(u_i')^2\right]}{\partial x_j} - \bar{\rho}2u_i'u_j'\frac{\partial \bar{u}_i}{\partial x_j} - \bar{\rho}u_j'\frac{\partial\left[(u_i')^2\right]}{\partial x_j} +$$

$$\bar{\rho}2\delta_{i3}u_i'\left(\frac{\theta_v'}{\bar{\theta}_v}\right)g + \bar{\rho}2f\varepsilon_{ij3}u_i'u_j' - \bar{\rho}2\frac{u_i'}{\bar{\rho}}\frac{\partial p'}{\partial x_i} + \bar{\rho}2vu_i'\frac{\partial^2 u_i'}{\partial x_j^2} + \qquad (2.a.(5).8)$$

$$\bar{\rho}2u_i'\frac{\partial(\overline{u_i'u_j'})}{\partial x_j}.$$

The perturbation continuity equation ($\frac{\partial(\bar{\rho}u_j')}{\partial x_j} = 0$, derived by using mean density

in the continuity equation, expanding this equation into mean and turbulent momentum parts, and subtracting the Reynolds averaged expanded equation from the expanded equation) is multiplied by $(u_i')^2$ and added to (2.a.(5).8). The result is then put into flux form,

$$\frac{\partial\left[\overline{\rho}(u_i')^2\right]}{\partial t} = -\frac{\partial\left[\overline{\rho}\,\overline{u}_j(u_i')^2\right]}{\partial x_j} - \overline{\rho}2u_i'u_j'\frac{\partial \overline{u}_i}{\partial x_j} - \frac{\partial\left[\overline{\rho}u_j'(u_i')^2\right]}{\partial x_j} +$$

$$\overline{\rho}2\delta_{i3}u_i'\left(\frac{\theta_v'}{\overline{\theta}_v}\right)g + \overline{\rho}2f\varepsilon_{ij3}u_i'u_j' - \overline{\rho}2\frac{u_i'}{\overline{\rho}}\frac{\partial p'}{\partial x_i} + \overline{\rho}2vu_i'\frac{\partial^2 u_i'}{\partial x_j^2} + \qquad (2.a.(5).9)$$

$$\overline{\rho}2u_i'\frac{\partial\left(\overline{u_i'u_j'}\right)}{\partial x_j}.$$

Equation (2.a.(5).9) is next Reynolds averaged to give

$$\frac{\partial\left[\overline{\rho}\,\overline{(u_i')^2}\right]}{\partial t} = -\frac{\partial\left[\overline{\overline{\rho}\,\overline{u}_j(u_i')^2}\right]}{\partial x_j} - \overline{\rho}2\overline{u_i'u_j'}\frac{\partial \overline{u}_i}{\partial x_j} - \frac{\partial\left[\overline{\overline{\rho}u_j'(u_i')^2}\right]}{\partial x_j} +$$

$$\overline{\rho}2\delta_{i3}\overline{u_i'\left(\frac{\theta_v'}{\overline{\theta}_v}\right)}g + \overline{\rho}2f\varepsilon_{ij3}\overline{u_i'u_j'} - \overline{\rho}2\overline{\frac{u_i'}{\overline{\rho}}\frac{\partial p'}{\partial x_i}} + \overline{\rho}2v\overline{u_i'\frac{\partial^2 u_i'}{\partial x_j^2}}. \qquad (2.a.(5).10)$$

Equation (2.a.(5).10) is simplified in the following manner. First, the second to last term (pressure perturbation term) is rewritten as $-\left(\frac{2\overline{\rho}}{\overline{\rho}}\right)\frac{\partial\left(\overline{u_i'p'}\right)}{\partial x_i} + 2\overline{\rho}\frac{\overline{p'}}{\overline{\rho}}\frac{\partial u_i'}{\partial x_i}$. Next, the repeated indices are summed over which eliminates the coriolis term in (2.a.(5).10) and the last term in the expression above (which converts the pressure term to divergence form). Since TKE is defined as $\overline{e} = 0.5\left(\overline{u'^2} + \overline{v'^2} + \overline{w'^2}\right)$, it is appropriate to sum over the repeated indices here. Finally, the last term (viscous dissipation term) is rewritten as $\overline{\rho}v\frac{\partial^2\left(\overline{u_i'^2}\right)}{\partial x_j^2} - 2\overline{\rho}v\overline{\left(\frac{\partial u_i'}{\partial x_j}\right)^2}$. The first term in this expression is the molecular diffusion of velocity variance. This variance changes slowly with distance in the boundary layer with typical values for the first term on the order of 10^{-11} kg m^{-1} s^{-3}. Considering an eddy 0.1 meters in diameter with a velocity that changes by 0.01 meters per second across the eddy, the instantaneous shear across this eddy is .1 s^{-1}. The shear becomes larger for smaller eddies. Using this value, the second term is on the order of 10^{-6} kg m^{-1} s^{-3}. For smaller eddies this term would be larger. Thus, the first term in this expression is several orders of magnitude less than the second term and can be ignored. These results are then applied to (2.a.(5).10) which, after dividing by 2, gives

$$\frac{\partial(\overline{\rho}\overline{e})}{\partial t} = -\frac{\partial(\overline{\rho}\overline{u_j}\overline{e})}{\partial x_j} - \overline{\rho}\overline{u_i'u_j'}\frac{\partial\overline{u_i}}{\partial x_j} - \frac{\partial(\overline{\rho}\overline{u_j'e})}{\partial x_j} + \overline{\rho}\delta_{i3}\frac{\overline{(u_i'\theta_v')}}{\overline{\theta}_v}g -$$

$$\frac{\partial(\overline{u_i'p'})}{\partial x_i} - \varepsilon, \tag{2.a.(5).11}$$

where $\varepsilon = \overline{\rho}v\overline{\left(\dfrac{\partial u_i'}{\partial x_j}\right)^2}$. Equation (2.a.(5).11) is simplified by neglecting horizontal

derivatives of perturbation terms. This gives

$$\frac{\partial(\overline{\rho}\overline{e})}{\partial t} = -\frac{\partial(\overline{\rho}\overline{u}\overline{e})}{\partial x} - \frac{\partial(\overline{\rho}\overline{v}\overline{e})}{\partial y} - \frac{\partial(\overline{\rho}\overline{w}\overline{e})}{\partial z} - \overline{\rho}\overline{u_i'u_i'}\frac{\partial\overline{u_i}}{\partial x_i} - \frac{\partial(\rho\overline{w'e})}{\partial z}$$

$$+\overline{\rho}\frac{\overline{(w'\theta_v')}}{\overline{\theta}_v}g - \frac{\partial(\overline{w'p'})}{\partial z} - \varepsilon. \tag{2.a.(5).12}$$

Now, this equation is integrated from level S- to B+ (see figure 1.b.1)

$$\int_{z=z_{S-}}^{z=z_{B+}}\frac{\partial(\overline{\rho}\overline{e})}{\partial t}\,dz = -\int_{z=z_{S-}}^{z=z_{B+}}\frac{\partial(\overline{\rho}\overline{u}\overline{e})}{\partial x}\,dz - \int_{z=z_{S-}}^{z=z_{B+}}\frac{\partial(\overline{\rho}\overline{v}\overline{e})}{\partial y}\,dz - \int_{z=z_{S-}}^{z=z_{B+}}\frac{\partial(\overline{\rho}\overline{w}\overline{e})}{\partial z}\,dz -$$

$$\int_{z=z_{S-}}^{z=z_{B+}}\overline{\rho}\overline{u_i'u_i'}\frac{\partial\overline{u_i}}{\partial x_i}\,dz - \int_{z=z_{S-}}^{z=z_{B+}}\frac{\partial(\rho\overline{w'e})}{\partial z}\,dz + \tag{2.a.(5).13}$$

$$\int_{z=z_{S-}}^{z=z_{B+}}\overline{\rho}\frac{\overline{(w'\theta_v')}}{\overline{\theta}_v}g\,dz - \int_{z=z_{S-}}^{z=z_{B+}}\frac{\partial(\overline{w'p'})}{\partial z}\,dz - \int_{z=z_{S-}}^{z=z_{B+}}\varepsilon\,dz.$$

Leibniz's rule is used to transform (2.a.(5).13) to

26

$$\frac{\partial}{\partial t}\int_{z=z_{S-}}^{z=z_{B+}}\overline{\rho e}\,dz = \overline{e}\left[\overline{\rho}\left(\frac{\partial z_{B+}}{\partial t}+\overline{u}\frac{\partial z_{B+}}{\partial x}+\overline{v}\frac{\partial z_{B+}}{\partial y}-\overline{w}\right)\right]-$$

$$\overline{e}\left[\overline{\rho}\left(\frac{\partial z_{S-}}{\partial t}+\overline{u}\frac{\partial z_{S-}}{\partial x}+\overline{v}\frac{\partial z_{S-}}{\partial y}-\overline{w}\right)\right]$$

$$-\frac{\partial}{\partial x}\int_{z=z_{S-}}^{z=z_{B+}}\overline{\rho u e}\,dz-\frac{\partial}{\partial y}\int_{z=z_{S-}}^{z=z_{B+}}\overline{\rho v e}\,dz+$$

$$-\int_{z=z_{S-}}^{z=z_{B+}}\overline{\rho u_i' u_i'}\frac{\partial \overline{u_i}}{\partial x_i}\,dz+\int_{z=z_{S-}}^{z=z_{B+}}\overline{\rho}\frac{\overline{(w'\theta_v')}}{\overline{\theta}_v}g\,dz-\qquad\text{(2.a.(5).14)}$$

$$\int_{z=z_{S-}}^{z=z_{B+}}\frac{\partial\left(\rho\overline{w'e}\right)}{\partial z}\,dz-\int_{z=z_{S-}}^{z=z_{B+}}\frac{\partial\left(\overline{w'p'}\right)}{\partial z}\,dz-\int_{z=z_{S-}}^{z=z_{B+}}\varepsilon\,dz.$$

This equation is similar to (2.a.(2).14), where the bracketed portion of the first two terms on the right hand side is the entrainment mass flux across the B+ and S-surfaces. The first term is zero because the turbulence kinetic energy vanishes just above the PBL top, and the second term is zero because the entrainment mass flux across the earth's surface is zero. The seventh term on the right hand side, which represents the flux divergence of TKE, is zero because the vertical turbulent flux of TKE is equal at the top and bottom of the PBL, hence the vertical integration of this quantity is zero. Finally, the second to last term on the right hand side (pressure correlation term) is zero since turbulence vanishes at the surface, and if gravity waves (that remove TKE from the top of the PBL) are neglected. Equation (2.a.(5).14) is then rewritten, using the hydrostatic relation ($\frac{\partial p}{\partial z}=-\rho g$),

$$\frac{\partial}{\partial t}\int_{z=z_{S-}}^{z=z_{B+}}\overline{\rho e}\,dz=-\nabla\bullet\int_{z=z_{S-}}^{z=z_{B+}}\overline{e}\overline{\rho}\overline{v}\,dz-\int_{z=z_{S-}}^{z=z_{B+}}\mathbf{F}_x\bullet\frac{\partial\overline{v}}{\partial x}\,dz-\int_{z=z_{S-}}^{z=z_{B+}}\mathbf{F}_y\bullet\frac{\partial\overline{v}}{\partial y}\,dz+$$

$$\int_{p=p_{B+}}^{p=p_{S-}}\mathbf{F}_v\bullet\frac{\partial\overline{v}}{\partial p}\,dp+\int_{p=p_{B+}}^{p=p_{S-}}\left(\overline{\rho}\frac{\overline{(w'\theta_v')}}{\overline{\theta}_v}\right)\frac{1}{\rho}\,dp-\int_{z=z_{S-}}^{z=z_{B+}}\varepsilon\,dz,\qquad\text{(2.a.(5).15)}$$

where $\mathbf{F}_x=\overline{\rho v'u'}$, $\mathbf{F}_y=\overline{\rho v'v'}$, and $\mathbf{F}_v=\overline{\rho v'w'}$ are each three components of the turbulent momentum flux (also known as the Reynolds stress). The subscript v (for vector) is used instead of w in the last equality because this quantity will be called the vector momentum flux. The first and second integrals are simplified by using the mixed layer values for the density, TKE, and momentum which gives

$$\frac{\partial\left(\rho_m e_m \Delta z_m\right)}{\partial t} = -\nabla \bullet \left(e_m \rho_m v_m \Delta z_m\right) - \int\limits_{z=z_{S-}}^{z=z_{B+}} F_x \bullet \frac{\partial \overline{v}}{\partial x}\, dz -$$

$$\int\limits_{z=z_{S-}}^{z=z_{B+}} F_y \bullet \frac{\partial \overline{v}}{\partial y}\, dz + \int\limits_{p=p_{B+}}^{p=p_{S-}} \left(F_v \bullet \frac{\partial \overline{v}}{\partial p}\right) dp +$$

$$\int\limits_{p=p_{B+}}^{p=p_{S-}} \left(\overline{\rho}\,\frac{\overline{(w'\theta_v')}}{\overline{\theta}_v}\right)\frac{1}{\rho}\, dp - \int\limits_{z=z_{S-}}^{z=z_{B+}} \varepsilon\, dz,$$

or

$$\frac{\partial\left(\rho_m e_m \Delta z_m\right)}{\partial t} = -e_m \rho_m \Delta z_m \left(\nabla \bullet v_m\right) - v_m \bullet \nabla\left(e_m \rho_m \Delta z_m\right)$$

$$-\int\limits_{z=z_{S-}}^{z=z_{B+}} F_x \bullet \frac{\partial \overline{v}}{\partial x}\, dz - \int\limits_{z=z_{S-}}^{z=z_{B+}} F_y \bullet \frac{\partial \overline{v}}{\partial y}\, dz +$$ (2.a.(5).16)

$$\int\limits_{p=p_{B+}}^{p=p_{S-}} \left(F_v \bullet \frac{\partial \overline{v}}{\partial p}\right) dp + \int\limits_{p=p_{B+}}^{p=p_{S-}} \left(\overline{\rho}\,\frac{\overline{(w'\theta_v')}}{\overline{\theta}_v}\right)\frac{1}{\rho}\, dp - \int\limits_{z=z_{S-}}^{z=z_{B+}} \varepsilon\, dz.$$

The shear term is then simplified by breaking the integration up into surface layer, mixed layer, and entrainment layer components. For the surface layer, the flux is constant and parallel to the wind (either both quantities are negative or positive, therefore, the product and integration of the product are positive). The wind increases from zero at S- to its mixed layer value at S. Therefore,

$$S_{Top\ of\ Surface\ Layer} = -\left|(F_v)_S\right| \int\limits_{p=p_{S-}}^{p=p_S} \frac{\partial|\overline{v}|}{\partial p}\, dp,$$

or (2.a.(5).17)

$$S_{Top\ of\ Surface\ Layer} = \left|(F_v)_S\right|\left|v_m\right|.$$

The negative sign in the first equation of (2.a.(5).17) is needed because the limits of integration were reversed, but as was stated above, the result (second equation) is positive. For the mixed layer, the wind is equal to its mixed layer value, thus there is no shear here. In the entrainment layer, the flux is assumed to decrease linearly from its value at B to zero at B+. The wind changes from its mixed layer value at B to another value at B+. Again, the wind and flux are assumed to be parallel. Then,

28

$$S_{Top\ of\ Entrainment\ Layer} = -\frac{1}{2}\big|(F_v)_B\big| \int_{p=p_B}^{p=p_{B+}} \frac{\partial |\bar{v}|}{\partial p}\, dp,$$

or

$$S_{Top\ of\ Entrainment\ Layer} = \frac{1}{2}\big|(F_v)_B\big||\Delta\bar{v}| = \frac{1}{2}E|\Delta\bar{v}|^2,$$

(2.a.(5).18)

where $|\Delta\bar{v}| = |\bar{v}_{B+}| - |\bar{v}_m|$ and $(F_v)_B = -E|\Delta\bar{v}|$. The second equality in (2.a.(5).18) is valid because the flux of momentum into the top of the boundary layer is due to entrainment of air from the free atmosphere when there is wind shear through the entrainment layer. This flux is zero if the entrainment rate is less than zero or if there is no wind shear. The second equality is obtained in the following manner. Neglecting fluxes due to radiation and clouds, the rate at which mass is added to the PBL from the free atmosphere (FA) is given by gE. For any arbitrary variable, A, the upward turbulent flux of A is denoted by F_A. The continuity of the total flux at level B, assuming $(F_A)_{B+} = 0$, is $-EA_{B+} = -EA_B + (F_A)_B$. The flux added to the PBL from the free atmosphere must equal the total flux within the PBL which consists of the flux within the PBL due to mass entrainment and the flux within the PBL due to upward turbulence transport. The transition of A at the PBL top is modeled as a jump given by $\Delta A = A_{B+} - A_B$. Using this in the flux continuity equation gives $(F_A)_B = -E\Delta A$. If $A = v$ then the second equality is obtained. Next, horizontal homogeneity is assumed in equation (2.a.(5).16), except for the second term which contains the mean divergence. This eliminates the third, fourth, and fifth terms in this equation. Then, (2.a.(5).17) and (2.a.(5).18) are summed with the result substituted into (2.a.(5).16) to give

$$\frac{\partial(\rho_m e_m \Delta z_m)}{\partial t} = -e_m \rho_m \Delta z_m (\nabla \bullet v_m) + \frac{1}{2}E|\Delta v|^2 + |(F_v)_s||v_m| +$$
$$\int_{p=p_{B+}}^{p=p_{S-}} \left(\bar{\rho}\frac{\overline{(w'\theta'_v)}}{\bar{\theta}_v} \right) \frac{1}{\rho}\, dp - \int_{z=z_{S-}}^{z=z_{B+}} \varepsilon\, dz.$$

(2.a.(5).19)

The buoyancy term can also be simplified by using an approximation for the flux of virtual dry static energy. The buoyancy term is written

$$B = \int_{p=p_{B+}}^{p=p_{S-}} \left(\bar{\rho}\frac{\overline{(w'\theta'_v)}}{\bar{\theta}_v} \right) \frac{1}{\rho}\, dp,$$

or using $F_{\theta_v} = \overline{\rho} \overline{w'\theta_v'}$,

$$B = \int_{p=p_{B+}}^{p=p_{S-}} \frac{F_{\theta_v}}{\overline{\theta}_v} \frac{1}{\rho} dp = \frac{1}{c_p} \int_{p=p_{B+}}^{p=p_{S-}} \frac{c_p \overline{T}_v F_{\theta_v}}{\theta_m} \frac{1}{\rho \overline{T}_v} dp,$$

where $\theta_m \cong \overline{\theta}_v$, or using $F_{SV} \equiv \dfrac{c_p \overline{T}_v F_{\theta_v}}{\theta_m}$ and equation of state,

$$B = \frac{R}{c_p} \int_{p=p_{B+}}^{p=p_{S-}} \frac{F_{SV}}{p} dp = \kappa \int_{p=p_{B+}}^{p=p_{S-}} \frac{F_{SV}}{p} dp. \qquad (2.a.(5).20)$$

Since the pressure does not change that much in the PBL and the flux of virtual dry static energy varies linearly, their ratio is nearly linear, and the last integral in (2.a.(5).20) can be simplified to

$$B = \frac{\kappa}{2} \left[\frac{(F_{SV})_S}{p_S} + \frac{(F_{SV})_B}{p_B} \right] \Delta p_m. \qquad (2.a.(5).21)$$

Now, the definition of the flux of virtual dry static energy from (2.a.(5).20) is used in (2.a.(5).21) to get

$$B = \frac{\kappa}{2} \left[\frac{c_p (\overline{T}_v)_S (F_{\theta_v})_S}{p_S \theta_m} + \frac{c_p (\overline{T}_v)_B (F_{\theta_v})_B}{p_B \theta_m} \right] \Delta p_m,$$

or using Poisson's equation,

$$B = \frac{\kappa}{2} \left\{ \left[\left(\frac{p_S}{p_o} \right)^\kappa \frac{c_p \theta_m (F_{\theta_v})_S}{p_S \theta_m} \right] + \left[\left(\frac{p_B}{p_o} \right)^\kappa \frac{c_p \theta_m (F_{\theta_v})_B}{p_B \theta_m} \right] \right\} \Delta p_m,$$

or

$$B = \frac{R}{2} \left\{ \left[\left(\frac{p_S}{p_o} \right)^\kappa \frac{(F_{\theta_v})_S}{p_S} \right] + \left[\left(\frac{p_B}{p_o} \right)^\kappa \frac{(F_{\theta_v})_B}{p_B} \right] \right\} \Delta p_m,$$

30

or using $F_{\theta_v} = F_\theta + (\theta_m)_v \delta F_q$, where $\delta = \dfrac{1-\varepsilon}{\varepsilon} = \dfrac{1-0.622}{0.622} = 0.608$,

$$B = \frac{R\Delta p_m}{2} \left\{ \left(\frac{p_S}{p_o}\right)^\kappa \left[\frac{(F_\theta)_S + (\theta_m)_v \delta(F_q)_S}{p_S}\right] \right.$$
$$\left. + \left(\frac{p_B}{p_o}\right)^\kappa \left[\frac{(F_\theta)_B + (\theta_m)_v \delta(F_q)_B}{p_B}\right] \right\},$$

(2.a.(5).22)

where $(F_\theta)_S$, $(F_\theta)_B = -E\Delta\theta$, $(F_q)_S$, and $(F_q)_B = -E\Delta q$ are the PBL surface and PBL top heat and moisture fluxes respectively. The PBL top fluxes of heat and moisture are defined in the same manner as the mass flux into the PBL top. Chapter 3 contains the details of the surface heat and moisture flux parameterizations.

The dissipation term is modeled by using a second-order closure assumption. The vertically integrated dissipation rate is $D = \int_{z=z_{S_-}}^{z=z_{B_+}} \varepsilon \, dz = \rho_m \sigma^3$, where σ is the dissipation velocity. Closure is obtained by assuming the square of σ is proportional to the vertically averaged TKE, $\sigma^2 = \dfrac{e_m}{a_1}$, where $a_1 = 0.163$ based on Deardorff's (1974) results. The vertically integrated dissipation rate is then related to the vertically averaged TKE by

$$D = \rho_m \left(\frac{e_m}{a_1}\right)^{\frac{3}{2}}.$$

(2.a.(5).23)

The TKE equation is finally written

$$\frac{\partial(\rho_m e_m \Delta z_m)}{\partial t} = -e_m \rho_m \Delta z_m (\nabla \bullet v_m) + S + B - D,$$

or

$$\Delta z_m \rho_m \frac{\partial e_m}{\partial t} = -e_m \left[\frac{\partial(\Delta z_m \rho_m)}{\partial t} + \rho_m \Delta z_m (\nabla \bullet v_m)\right] + S + B - D,$$

31

or using the hydrostatic relation and since the term inside the brackets is the entrainment,

$$\frac{\partial e_m}{\partial t} = \frac{g}{\Delta p_m}\left(S + B - Ee_m - D\right),$$

(2.a.(5).24)

where S is given by (2.a.(5).17) and (2.a.(5).18), B by (2.a.(5).22), and D by (2.a.(5).23). The entrainment rate is determined in the following section.

2.a.(6) Entrainment Rate Equations

Entrainment is the mechanism that brings unmixed free-atmosphere air into the top of the PBL. This air becomes mixed by the existing turbulence in the mixed layer causing the mixed layer to grow. The entrainment rate is positive if free-atmosphere air is being brought into the top of the mixed layer. It is zero if no air is transported across the PBL top. If air is being removed from the top of the mixed layer then the entrainment rate is negative and the mixed layer is decaying. Because the previously described prognostic equations require knowledge of E, it must be parameterized to solve these equations. Since turbulence is required to mix newly entrained free-atmosphere air, E is considered proportional to the square root of the TKE. This is the basis for the parameterization described in section 2.a.(6)(a). This parameterization is used when the entrainment rate is determined to be positive.

If there is no turbulence, then the TKE and E will equal zero. The existence of turbulence alone, however, does not guarentee that E will be positive. Table 2.a.(6).1 summarizes the conditions that determine the sign of E.

Table 2.a.(6).1: Sign of E Based on B+S and B_0+S_0.

	Sum of Buoyancy and Shear Computed with E=0 (where $0 \leq$ fraction ≤ 1)	
Sum of Buoyancy and Shear	$B_0 + S_0 <$ fraction $* D$	$B_0 + S_0 >$ fraction $* D$
$B + S <$ fraction $* D$	Case 1 **E<0**	Case 2 **E>0** $(B < B_0 \therefore EB_1 < 0;$ since $EB_1 = 0$ if $E \leq 0$, E must be greater than zero and B_1 must be less than zero)
$B + S >$ fraction $* D$	Case 3 **E>0** $(B > B_0 \therefore EB_1 > 0;$ since $EB_1 = 0$ if $E \leq 0$, E must be greater than zero and B_1 must be greater than zero)	Case 4 **E>0**

These conditions are checked during each time step of a model run. If E is determined to be less than zero during a given time step, then the negative parameterization described in section 2.a.(6)(b) is used to compute E.

During rapid growth, the TKE and E become large. Since the dissipation rate is proportional to the TKE, it also becomes large. It is possible for the sums of B+S and

33

$B_0 + S_0$ to be less than D which would cause a large entrainment rate to suddenly become negative. There are two ways to prevent this from happening. One way is to set a threshold of E such that when E is currently greater than this threshold it is calculated using the positive parameterization regardless of the value of the sums. A better way is to check the sums against a fraction of the dissipation (as indicated in Table 2.a.(6).1), where this fraction is set as a tunable parameter. A proper selection of this parameter will prevent the sums from being less than the fraction of the dissipation during periods of rapid PBL growth. Table 2.a.(6).1 is discussed further in section 2.a.(6)(b).

During the late afternoon, before sunset, the clear convective boundary layer over land has reached a quasi-steady-state. At this point the surface buoyancy flux rapidly approaches zero with the loss of daytime heating. Both the entrainment rate and TKE are small compared to their values in the mid-morning (during the rapid growth of the PBL). At this point, a balance has occurred in the TKE equation Since there are no processes to generate a significant amount of TKE at this time of day, the local rate of change of the TKE is small and can be neglected. The sign of the entrainment rate then depends on the sum of the buoyancy and shear terms. If this sum is small enough the entrainment rate will be negative.

There are contributions to the buoyancy and shear production from the surface and PBL top. The contributions from the PBL top depend on the sign and magnitude of the entrainment rate. Since the entrainment rate determines how fast mass is brought into the top of the PBL, mass will cross the free-atmosphere PBL top interface only when the entrainment rate is positive. Thus, if the entrainment is zero or less then there will be no contribution to the buoyancy or shear production at the top of the PBL. With positive entrainment, buoyancy production at the top of the PBL can be positive or negative depending on the gradient of temperature and moisture here. The shear production at the PBL top is always non-negative. It is positive if the entrainment rate is positive and there is wind shear across the top of the PBL, and it is zero if either the wind shear is zero or the entrainment rate is zero or less. Therefore, the sum of the buoyancy and shear production (with surface and top contributions) along with the sum of the buoyancy and shear production at the top of the PBL must be considered to determine the sign of the entrainment rate.

2.a.(6)(a) Positive Entrainment

From Breidenthal and Baker (1985), the positive entrainment rate formula without clouds is

$$E = \rho_B \sqrt{e_m} \frac{b_1}{(1 + b_2 Ri)},$$

(2.a.(6)(a).1)

where $Ri = \frac{g \Delta \bar{\theta}_v \Delta z_m}{(\theta_m)_v e_m}$ is the relevant Richardson number, and b_1 and b_2 are constants determined as follows. For a strong inversion, $b_2 Ri \gg 1$, and (2.a.(6)(a).1) reduces to

$$E = \rho_B \sqrt{e_m} \frac{b_1}{b_2 Ri}.$$

(2.a.(6)(a).2)

Now, substituting the expression for Ri into (2.a.(6)(a).2) gives

$$\frac{b_1}{b_2} = \frac{g E \Delta \bar{\theta}_v \Delta z_m}{\rho_B (\theta_m)_v (e_m)^{3/2}}.$$

(2.a.(6)(a).3)

Using the famous "0.2" formula, $E \Delta \bar{\theta}_v = 0.2 \left(F_{\theta_v} \right)_s$ (see Randall, 1984), (2.a.(6)(a).3) becomes

$$\frac{b_1}{b_2} = \frac{0.2 g \left(F_{\theta_v} \right)_s \Delta z_m}{\rho_B (\theta_m)_v (e_m)^{3/2}}.$$

(2.a.(6)(a).4)

Next, a balance is assumed between buoyant production and dissipation of TKE. The buoyancy term is written in a slightly different form from (2.a.(5).22), and the dissipation is given by (2.a.(5).23). This balance is then written

$$\frac{g \left(F_{\theta_v} \right)_s \Delta z_m}{2 \theta_s} = \rho_m \left(\frac{e_m}{a_1} \right)^{3/2}.$$

(2.a.(6)(a).5)

Since $\rho_B = \rho_m$ and $(\theta_m)_v \cong \theta_s$, (2.a.(6)(a).5) can be substituted into (2.a.(6)(a).4) to obtain

$$\frac{b_1}{b_2} = \frac{(0.2)2}{(a_1)^{3/2}} \approx 6.10.$$

(2.a.(6)(a).6)

Now, in the no inversion limit (Ri=0), (2.a.(6)(a).1) reduces to

$$E = \rho_B \sqrt{e_m} b_1.$$

(2.a.(6)(a).7)

Deardorff (1974) found by large-eddy simulation that

$$E = 0.2\rho_B \left[\frac{g(F_{\theta_v})_s \Delta z_m}{(\rho\theta)_s} \right]^{1/3},$$

(2.a.(6)(a).8)

where $w^* = \left[\dfrac{g(F_{\theta_v})_s \Delta z_m}{(\rho\theta)_s} \right]^{1/3}$ is the convective velocity scale of Deardorff (1970). Using

(2.a.(6)(a).5) and (2.a.(6)(a).8) (where $\rho_s = \rho_m = \rho_B$), (2.a.(6)(a).7) becomes

$$b_1 = 0.2 \left[\frac{2}{(a_1)^{3/2}} \right]^{1/3} \approx 0.624.$$

(2.a.(6)(a).9)

Finally, from (2.a.(6)(a).6), one obtains $b_2 \approx 0.102$.

2.a.(6)(b) Negative Entrainment

Assuming the entrainment rate and TKE are small compared to their values during rapid PBL growth, the local rate of change of TKE is small and can be neglected in the TKE equation to give

$$0 = -Ee_m + S + B - D.$$

(2.a.(6)(b).1)

The sign of the entrainment rate then depends on the sum of the buoyancy and shear terms. Solving for E in the above equation gives

$$E = \frac{S + B - D}{e_m},$$

(2.a.(6)(b).2)

36

where E>0 if (S+B)>D. There are four possible cases for determining the sign of E. The buoyancy and shear terms are first written

$$B = B_0 + EB_1 \text{ and } S = S_0 + ES_1,$$
(2.a.(6)(b).3)

where the zero subscript indicates the surface contribution to the buoyancy and shear (as if E were zero), and the one subscript is the contribution to the buoyancy and shear at the top of the PBL due to entrainment (as if the surface fluxes were zero). The buoyancy and shear terms (B and S) are then computed assuming E>0. Then, the surface contributions to the buoyancy and shear (B_0 and S_0) are computed and summed. These sums are compared to arrive at one of the four possible cases listed in Table 2.a.(6).1.

If Case 1 occurs then the entrainment rate is determined using the negative production formulation. This is accomplished by partitioning the TKE equation into a weighted contribution of the local rate of change of TKE and a weighted contribution of the production of TKE due to entrainment. Equation (2.a.(5).24) is split into two equations (where $B=B_0$ and $S=S_0$ since E<0),

$$g^{-1}\Delta p_m \frac{\partial e_m}{\partial t} = weight\left(B_0 + S_0 - D\right)$$

and
(2.a.(6)(b).4)

$$E = \frac{(1 - weight)\left(B_0 + S_0 - D\right)}{e_m},$$

where $0 \leq weight \leq 1$. If the weight is set to one then the sum of the above equations is just (2.a.(5).24). The TKE is first determined using the top equation in (2.a.(6)(b).4), and then the entrainment rate is determined using this new value of the TKE and the bottom equation in (2.a.(6)(b).4).

2.b. Initialization

The model requires that certain variables, including prognostic variables, be initialized before time-stepped predictions are made. Chapter 4 provides a brief description of the Wangara data set used to initialize the land simulations. For land, four data files are used that include: three hourly sounding data which includes temperatures

and mixing ratios at various pressure levels, hourly sounding data which includes u and v wind components at various heights, hourly ground temperatures, and hourly u and v geostrophic wind components. Prognostic variables initialized over land are obtained by interpolating between two data periods based on the model start time (e.g., with a start of 1030L, temperatures and mixing ratios would equal the sum of one-half of their values at the 0900L and 1200L sounding times), and by interpolating between data levels (heights or pressures) where appropriate. Table 2.b.1 summarizes the prognostic variables that are initialized for simulations over land or water.

Table 2.b.1: Summary of Prognostic Variable Initializations.

Prognostic Variable	Land Initialization	Water Initialization
Mean pressure thickness	Initialized based on data and start time of model run	Assigned an initial value
Mean u and v wind components	Initialized from data	Computed as one-half sum of surface wind and wind at top of PBL
Mean potential temperature	Initialized from data	Assigned an initial value
Mean mixing ratio	Initialized from data	Assigned an initial value
Turbulence kinetic energy	Assigned an initial value	Assigned an initial value

Table 2.b.2 contains the constants that must be set at the start of a simulation.

Table 2.b.2: Summary of Constants.

Constant	Land Value	Water Value	Use
Time step (Δt)	60 seconds	60 seconds	Compute prognostic equations
Sea surface temperature	N/A	289° K	Compute surface potential temperature, surface mixing ratio, and surface density
Mixing ratio at top of PBL	Not a constant: interpolated between two sounding periods	1 g/kg	Compute virtual potential temperature at top of PBL, buoyancy, and mean mixing ratio
Potential temperature lapse rate above the PBL	N/A	4° K/km	Compute potential temperature at top of PBL
Surface u and v wind components	N/A	2 m/s	Compute u and v wind components at top of PBL
Wind lapse rate above the PBL	N/A	5 m/s/km	Compute u and v wind components at top of PBL
Geostrophic u and v wind components	Not constant: interpolated between two sounding periods	u_g=-10 m/s v_g=0 m/s	Compute mean u and v wind components

2.c. Top Boundary Conditions

As shown by figure 1.b.1, the model domain is bounded at the top by the free atmosphere and at the bottom by the earth's surface. Top boundary conditions are applied at the PBL top-free atmosphere interface, and surface boundary conditions are applied at

39

the PBL bottom-earth surface interface. Lateral boundary conditions are not required with the assumption of horizontal homogeneity.

Turbulence in the mixed layer results in uniform prognostic variables within the layer (i.e., $\theta \to \theta_m$, $q \to q_m$, $e \to e_m$, $u \to u_m$, $v \to v_m$). This turbulence also mixes free-atmosphere air that is entrained into the top of the PBL. The first and very important top boundary condition that the model requires is that the turbulence becomes zero at the interface between the PBL top and the free atmosphere. This boundary condition is used to simplify the prognostic equations. Zero flux at the interface is the boundary condition that leads to $(F_A)_B = -E\Delta A$ (described in section 2.a.(5)). The next boundary condition is applied to the flux of A at level B, not at the interface, when the entrainment rate is less than zero. This flux is zero when the entrainment rate is less than zero because no mass enters the PBL top when E<0. The model uses this boundary condition to set the fluxes of heat, moisture, and momentum across the PBL top to zero whenever the entrainment is less than zero. The remaining top boundary conditions are applied to the TKE equation. Since TKE is a measure of the turbulence, the TKE also vanishes at the interface. The next boundary condition applies to both the top and bottom. The vertical turbulent flux of TKE at the top is equal to its value at the surface. The final top boundary condition is that the pressure correlation term vanishes at the top of the PBL when gravity waves are neglected.

2.d. Surface Boundary Conditions

The earth's surface acts as physical barrier at the bottom of the PBL. Complications arise in applying surface boundary conditions when the surface is heterogeneous and varies orographically. The first surface boundary condition is horizontal homogeneity. The next boundary condition is that no mass can cross the earth's surface. These two boundary conditions are used with all the prognostic equations. The equality of the vertical turbulent flux of TKE at the top and bottom is the third surface boundary condition. The remaining boundary condition is the loss of turbulence at the earth's surface. This, along with the neglect of gravity waves mentioned above, eliminates the pressure correlation term in the TKE equation. Table 2.a.1 lists the boundary conditions used with the prognostic equations.

40

3. One-Layer Model Time Schemes

3.a Surface Heat-Moisture and Momentum Flux Parameterizations

The parameterization scheme developed by Louis (1979) is well suited to this model. The parameterization is complicated enough to accurately represent the effects of boundary layer fluxes over long periods, but not too complicated to preclude rapid computer solutions even with lengthy simulations. This is especially important in incorporating this model into a general circulation model where very long simulation periods are required. The parameterization also fits well with the boundary layer being represented by one or two levels, and the assumption that the fluxes vary linearly with height from the surface to the PBL top (the top may be constant, or in this case prognostically determined by the model). The description of the boundary layer by this model is sufficiently detailed to prevent incorrect feed-back from occurring. Accurate feed-back is necessary because this parameterization relates the magnitude of the fluxes to the prognostic variables. Finally, since the model depends on both buoyant and shear driven turbulence, the parameterization should simulate both of these processes. Louis' parameterization accomplishes this by requiring that the diffusion coefficients not only depend on the wind shear, but also the static stability of the atmosphere.

The parameterization scheme is based on Monin-Obukhov similarity theory. The Monin-Obukhov scale height is given by

$$L = \frac{\bar{\theta} u_*^2}{k g \theta_*}, \tag{3.a.1}$$

where $u_* = \sqrt{|\overline{w'u'}|}$ is the scaling velocity, k the Von Karman constant, g the acceleration of gravity, and $\theta_* = -\overline{w'\theta'}/u_*$ the scaling temperature. The integrated flux profile relationships give

$$u = \frac{u_*}{k}\left[ln(z/z_0) - \psi_{mom}(z/L) + \psi_{mom}(z_0/L) \right], \tag{3.a.2}$$

41

and

$$\Delta\theta = -R\frac{\theta_*}{k}\left[ln(z/z_0) - \psi_{heat-moisture}(z/L) + \psi_{heat-moisture}(z_0/L)\right], \qquad (3.a.3)$$

where z is the surface height (set to 10 meters in the model), z_0 the roughness height, ψ are Businger's functions for momentum and heat-moisture, R is a constant equal to 0.74, and $\Delta\theta = \theta_{s_-} - \theta_m$ (the opposite of Louis' definition, hence the minus sign in (3.a.3)). Substitution of (3.a.2) and (3.a.3) into (3.a.1) results in

$$L = -\frac{\overline{\theta}u^2}{g\Delta\theta}\frac{\left[ln(z/z_0) - \psi_{mom}(z/L) + \psi_{heat-moisture}(z_0/L)\right]}{\left[ln(z/z_0) - \psi_{mom}(z/L) + \psi_{mom}(z_0/L)\right]^2}. \qquad (3.a.4)$$

The momentum and heat flux formulations are then determined in the following manner. First, the square of the scaling velocity is solved for from (3.a.1). This gives

$$u_*^2 = \frac{kg\theta_* L}{\overline{\theta}}. \qquad (3.a.5)$$

Next, (3.a.4) is substituting into (3.a.5) to get

$$u_*^2 = -\frac{ku^2\theta_*}{\Delta\theta}\frac{\left[ln(z/z_0) - \psi_{mom}(z/L) + \psi_{heat-moisture}(z_0/L)\right]}{\left[ln(z/z_0) - \psi_{mom}(z/L) + \psi_{mom}(z_0/L)\right]^2}. \qquad (3.a.6)$$

Then, equation (3.a.3) is used to convert (3.a.6) to

$$u_*^2 = a^2 u^2 F_{mom}(z/z_0, L), \qquad (3.a.7)$$

where $a^2 = \dfrac{k^2}{\left[ln(z/z_0)\right]^2}$ is the drag coefficient, and F a function dependent on z, z_0, and L.

The Monin-Obukhov scale height is related to the bulk Richardson number, $Ri_B = -\dfrac{gz\Delta\theta}{\overline{\theta}u^2}$, which can be inferred from (3.a.4), therefore F is also dependent on z, z_0, and Ri_B. Thus, the surface momentum flux is

$$\rho_{s_-}\overline{w'u'} = -\rho_{s_-}u_*^2 = -\rho_{s_-}a^2 u^2 F_{mom}(z/z_0, Ri_B). \qquad (3.a.8)$$

Similarly, the surface heat and moisture fluxes are

$$\rho_{S-}\overline{w'\theta'} = -\rho_{S-}u_{\bullet}\theta_{\bullet} = \frac{\rho_{S-}a^2u\Delta\theta F_{heat-moisture}(z/z_0,Ri_B)}{R} \qquad (3.a.9a)$$

and

$$\rho_{S-}\overline{w'q'} = -\rho_{S-}u_{\bullet}q_{\bullet} = \frac{\rho_{S-}a^2u\Delta qF_{heat-moisture}(z/z_0,Ri_B)}{R}. \qquad (3.a.9b)$$

The model uses $(u^2)_{u-momentum} = |v_m|u_m$, $(u^2)_{v-momentum} = |v_m|v_m$, and $(u)_{heat-moisture} = |v_m|$ in the above equations.

Louis computed the momentum and heat-moisture functions numerically. Analytical formulae were then fit to the functions. The analytical formulae eliminate the need to perform an iterative calculation during each time step. For unstable conditions (when $Ri_B < 0$)

$$F = 1 - \frac{bRi_B}{1+c|Ri_B|^{1/2}}, \qquad (3.a.10)$$

where b=9.4, $c_{mom} = 7.4a^2b\left(\frac{z}{z_0}\right)^{1/2}$, and $c_{heat-moisture} = 5.3a^2b\left(\frac{z}{z_0}\right)^{1/2}$. The function for the neutral and stable cases ($Ri_B \geq 0$) is

$$F = \frac{1}{(1+b'Ri_B)^2}, \qquad (3.a.11)$$

where $b' = 4.7$.

3.b. Conservation of Momentum

The conservation of momentum equations (2.a.(2).20) and (2.a.(2).21) are approximated by a forward time scheme for the first, 101st, 201st, 301st, etc., time steps, and by a leap-frog time scheme for all other time steps. This is illustrated in figure 3.b.1 below. Periodically using a forward time step prevents any large divergence from building up in the solutions produced by the leap-frog time steps.

F1   L2   L4...   L100 F101 L102...L...

N+...   101   103

Time   0   2
Step   N+3   100   102   N+...

L1   L3...   L99   L101... L...

Leap-Frog Scheme
starts over here
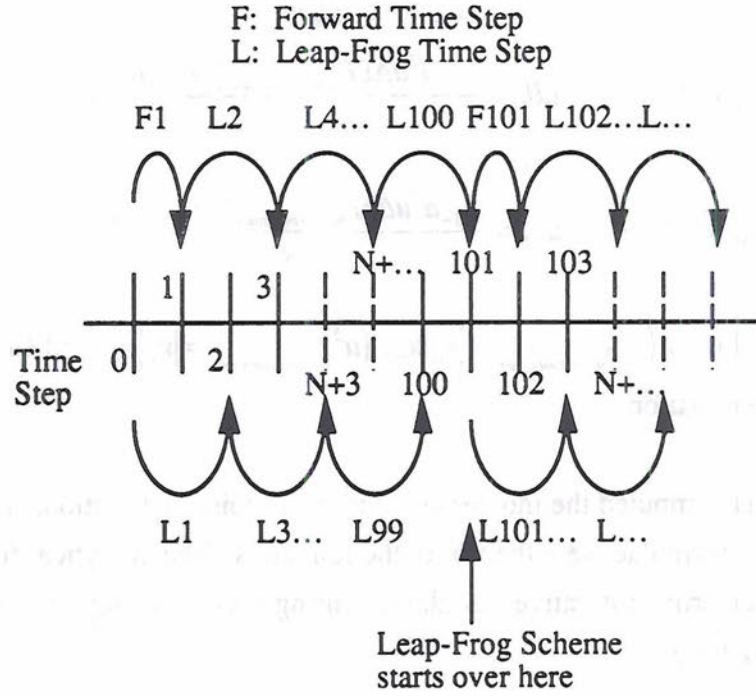
Figure 3.b.1: Conservation of Momentum Time Scheme Flow Diagram

The forward time difference schemes for (2.a.(2).20) and (2.a.(2).21) when E>0 are

$$u_m^n = u_m^{n-1} + \Delta t f\left(v_m^{n-1} - v_g\right) - \frac{\Delta t \rho_{sfc} a^2 F_{mom} u_m^n \left|v_m^{n-1}\right|}{\rho_m \Delta z_m} + \frac{\Delta t E\left(u_{B+} - u_m^n\right)}{\rho_m \Delta z_m},$$

or

$$u_m^n = \frac{u_m^{n-1} + \Delta t f\left(v_m^{n-1} - v_g\right) + \frac{\Delta t E u_{B+}}{\rho_m \Delta z_m}}{1 + \frac{\Delta t \rho_{sfc} a^2 F_{mom} \left|v_m^{n-1}\right|}{\rho_m \Delta z_m} + \frac{\Delta t E}{\rho_m \Delta z_m}},$$ (3.b.1)

and

$$v_m^n = v_m^{n-1} - \Delta t f\left(u_m^{n-1} - u_g\right) - \frac{\Delta t \rho_{sfc} a^2 F_{mom} v_m^n \left|v_m^{n-1}\right|}{\rho_m \Delta z_m} + \frac{\Delta t E\left(v_{B+} - v_m^n\right)}{\rho_m \Delta z_m},$$

or

44

$$v_m^n = \frac{v_m^{n-1} - \Delta t f\left(u_m^{n-1} - u_g\right) + \dfrac{\Delta t E v_{B+}}{\rho_m \Delta z_m}}{1 + \dfrac{\Delta t \rho_{sfc} a^2 F_{mom}\left|v_m^{n-1}\right|}{\rho_m \Delta z_m} + \dfrac{\Delta t E}{\rho_m \Delta z_m}}.$$ (3.b.2)

For $E \leq 0$, equations (3.b.1) and (3.b.2) reduce to

$$u_m^n = \frac{u_m^{n-1} + \Delta t f\left(v_m^{n-1} - v_g\right)}{1 + \dfrac{\Delta t \rho_{sfc} a^2 F_{mom}\left|v_m^{n-1}\right|}{\rho_m \Delta z_m}},$$ (3.b.1a)

and

$$v_m^n = \frac{v_m^{n-1} - \Delta t f\left(u_m^{n-1} - u_g\right)}{1 + \dfrac{\Delta t \rho_{sfc} a^2 F_{mom}\left|v_m^{n-1}\right|}{\rho_m \Delta z_m}}.$$ (3.b.2a)

The pressure gradient/coriolis terms are represented explicitly (n-1), while the divergence and flux terms are represented implicitly (n). Fully implicit representation would require solving two equations in two unknowns simultaneously. The partially implicit representation is used to simplify solving the equations and still maintain stability. Initial condition data (see section 2.b.) is used for the values at n-1 for the first time step. The values computed by the previous leap-frog time step are used as initial conditions (n-1 values) for the forward time step computations at time steps 101, 201, 301, etc.

The leap-frog time difference schemes for (2.a.(2).20) and (2.a.(2).21) when E>0 are

$$u_m^{n+1} = u_m^{n-1} + 2\Delta t f\left(v_m^n - v_g\right) - \frac{2\Delta t \rho_{sfc} a^2 F_{mom} u_m^{n+1}\left|v_m^{n-1}\right|}{\rho_m \Delta z_m} + \frac{2\Delta t E\left(u_{B+} - u_m^{n+1}\right)}{\rho_m \Delta z_m}$$

or

$$u_m^{n+1} = \frac{u_m^{n-1} + 2\Delta t f\left(v_m^n - v_g\right) + \dfrac{2\Delta t E u_{B+}}{\rho_m \Delta z_m}}{1 + \dfrac{2\Delta t \rho_{sfc} a^2 F_{mom}\left|v_m^{n-1}\right|}{\rho_m \Delta z_m} + \dfrac{2\Delta t E}{\rho_m \Delta z_m}},$$ (3.b.3)

and

$$v_m^{n+1} = v_m^{n-1} - 2\Delta t f\left(u_m^n - u_g\right) - \frac{2\Delta t \rho_{sfc} a^2 F_{mom} v_m^{n+1}\left|v_m^{n-1}\right|}{\rho_m \Delta z_m} + \frac{2\Delta t E\left(v_{B+} - v_m^{n+1}\right)}{\rho_m \Delta z_m}$$

or

$$v_m^{n+1} = \frac{v_m^{n-1} - 2\Delta t f_c\left(u_m^n - u_g\right) + \dfrac{2\Delta t a^2 F_{mom}\left|v_m^{n-1}\right|}{\rho_m \Delta z_m} + \dfrac{2\Delta t E v_{B+}}{\rho_m \Delta z_m}}{1 + \dfrac{2\Delta t \rho_{sfc} a^2 F_{mom}\left|v_m^{n-1}\right|}{\rho_m \Delta z_m} + \dfrac{2\Delta t E}{\rho_m \Delta z_m}}. \tag{3.b.4}$$

For E≤0, (3.b.3) and (3.b.4) become

$$u_m^{n+1} = \frac{u_m^{n-1} + 2\Delta t f\left(v_m^n - v_g\right)}{1 + \dfrac{2\Delta t \rho_{sfc} a^2 F_{mom}\left|v_m^{n-1}\right|}{\rho_m \Delta z_m}}, \tag{3.b.3a}$$

and

$$v_m^{n+1} = \frac{v_m^{n-1} - 2\Delta t f_c\left(u_m^n - u_g\right) + \dfrac{2\Delta t a^2 F_{mom}\left|v_m^{n-1}\right|}{\rho_m \Delta z_m}}{1 + \dfrac{2\Delta t \rho_{sfc} a^2 F_{mom}\left|v_m^{n-1}\right|}{\rho_m \Delta z_m}}. \tag{3.b.4a}$$

Here again, the pressure gradient/coriolis terms are represented explicitly (n), and the divergence and flux terms are represented implicitly (n+1). After the values at n+1 are computed during a leap-frog time step, the values at n-1 are updated to the values at n and the values at n are updated to the newly computed values at n+1, before the next leap-frog time step.

3.c. Conservation of Potential Temperature

Equation (2.a.(3).12), $\dfrac{\partial \theta_m}{\partial t} = \dfrac{E\left(\bar{\theta}_{B+} - \theta_m\right)}{\rho_m \Delta z_m} + \dfrac{\rho_{sfc} a^2 \left|v_m\right| F_{heat-moisture}}{0.74 \rho_m \Delta z_m}\left(\bar{\theta}_{S-} - \theta_m\right)$, is

rewritten as

$$\frac{\partial \theta_m}{\partial t} = \frac{gE}{\Delta p_m}\left(\bar{\theta}_{B+} - \theta_m\right) + \frac{gV}{\Delta p_m}\left(\bar{\theta}_{S-} - \theta_m\right), \tag{3.c.1}$$

where $V = \dfrac{\rho_{sfc} a^2 |v_m| F_{heat-moisture}}{0.74}$ is the ventilation or surface layer mass flux. A backward (implicit) time scheme is used to represent (3.c.1). This scheme is unconditionally stable and has first order accuracy. The finite difference form of (3.c.1) when E>0 is then

$$\theta_m^{n+1} = \theta_m^n + \frac{gE\Delta t}{\Delta p_m}\left(\overline{\theta}_{B+} - \theta_m^{n+1}\right) + \frac{gV\Delta t}{\Delta p_m}\left(\overline{\theta}_{S-} - \theta_m^{n+1}\right),$$

or

$$\theta_m^{n+1} = \frac{\theta_m^n + \dfrac{gE\Delta t}{\Delta p_m}\overline{\theta}_{B+} + \dfrac{gV\Delta t}{\Delta p_m}\overline{\theta}_{S-}}{1 + \dfrac{gE\Delta t}{\Delta p_m} + \dfrac{gV\Delta t}{\Delta p_m}}. \tag{3.c.2}$$

When E≤0 (3.c.2) reduces to

$$\theta_m^{n+1} = \frac{\theta_m^n + \dfrac{gV\Delta t}{\Delta p_m}\overline{\theta}_{S-}}{1 + \dfrac{gV\Delta t}{\Delta p_m}}. \tag{3.c.2a}$$

Equations (3.c.2) and (3.c.2a) were used for the ocean simulations.

A prescribed surface heat flux was used for the Wangara simulations. Following André et al. (1978), the surface heat flux is approximated from Day 33 of the Wangara data as a sine wave (Figure 3.c.1)

$$Q_0 = (Q_0)_{max}\, sin\left(\frac{\pi(t_{min} - 450)}{600}\right), \tag{3.c.3}$$

where Q_0 is the kinematic heat flux in units of K m s^{-1}, $(Q_0)_{max}$ the maximum value of the heat flux set to 0.18 K m s^{-1}, and t_{min} is the current simulated model time in minutes. The surface heat flux is then obtained by multiplying Q_0 by the surface air density to give units of K kg m^{-2} s^{-1}. The maximum downward heat flux at night was set to 0.005 K m s^{-1} ($\approx$ 6 W m^{-2}).
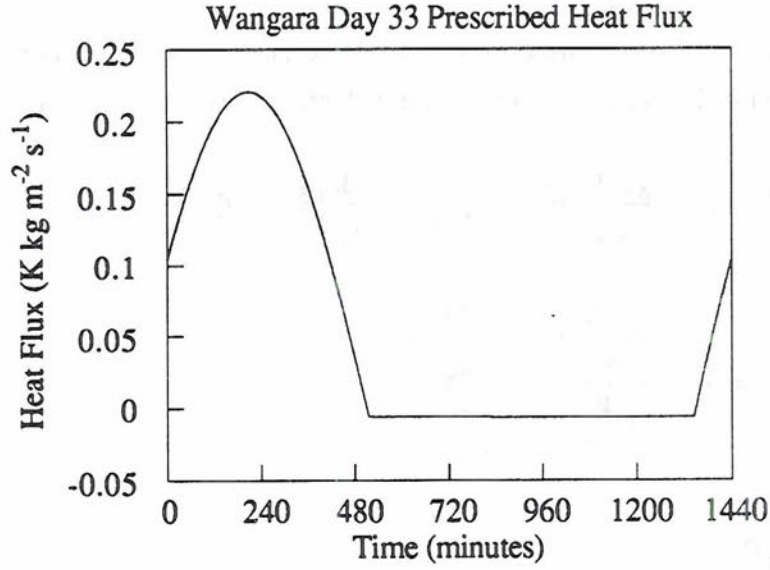
Figure 3.c.1: Prescribed Wangara Day 33 Surface Heat Flux From André et al. (1978)

Using the prescribed heat flux for Wangara, equations (3.c.2) and (3.c.2a) become

$$\theta_m^{n+1} = \frac{\theta_m^n + \frac{gE\Delta t}{\Delta p_m}\overline{\theta}_{B+} + \frac{g\Delta t}{\Delta p_m}\rho_{S-}Q_0}{1 + \frac{gE\Delta t}{\Delta p_m}} \tag{3.c.4}$$

and

$$\theta_m^{n+1} = \theta_m^n + \frac{g\Delta t}{\Delta p_m}\rho_{S-}Q_0. \tag{3.c.4a}$$

3.d. Conservation of Mixing Ratio

The time scheme equations for the mixing ratio are developed in the same manner as the equations for the potential temperature. A backward (implicit) scheme is also used to represent equation (2.a.(4).8) rewritten similar to (3.c.1). Then, when E>0, the mixing ratio time difference equation is

$$q_m^{n+1} = \frac{q_m^n + \frac{gE\Delta t}{\Delta p_m}\overline{q}_{B+} + \frac{gV\Delta t}{\Delta p_m}\overline{q}_{S-}}{1 + \frac{gE\Delta t}{\Delta p_m} + \frac{gV\Delta t}{\Delta p_m}}. \tag{3.d.1}$$

48

When $E \leq 0$, (3.d.1) becomes

$$q_m^{n+1} = \frac{q_m^n + \frac{gV\Delta t}{\Delta p_m}\bar{q}_{s-}}{1 + \frac{gV\Delta t}{\Delta p_m}}. \tag{3.d.1a}$$

Here, the Louis (1979) heat-moisture surface flux parameterization was used for both the Wangara and ocean simulations.

3.e. Turbulence Kinetic Energy

The time difference form of equation (2.a.(5).24) is written

$$\left(g^{-1}\Delta p_m\right)\frac{\sqrt{e_m^{n+1}}^2 - \sqrt{e_m^n}^2}{\Delta t} = E(B_1 + S_1) + B_0 + S_0 - Ee_m^{n+1} - D, \tag{3.e.1}$$

or using $D = \frac{\rho_m}{(a_1)^{\frac{3}{2}}}\sqrt{e_m^{n+1}}^3$ and $E = \rho_B\sqrt{e_m^{n+1}}\frac{b_1}{(1+b_2Ri)}$,

$$\left(g^{-1}\Delta p_m\right)\frac{\sqrt{e_m^{n+1}}^2 - \sqrt{e_m^n}^2}{\Delta t} = \rho_B\sqrt{e_m^{n+1}}\frac{b_1}{(1+b_2Ri)}(B_1 + S_1) + B_0 + S_0 -$$

$$\rho_B\sqrt{e_m^{n+1}}\frac{b_1}{(1+b_2Ri)}e_m^{n+1} - \frac{\rho_m}{(a_1)^{\frac{3}{2}}}\sqrt{e_m^{n+1}}^3. \tag{3.e.2}$$

After rearrangement, (3.e.2) becomes

$$\sqrt{e_m^{n+1}}^3 + \frac{\Delta p_m}{g\Delta t}\left[\frac{\rho_m}{(a_1)^{3/2}} + \frac{\rho_B b_1}{(1+b_2Ri)}\right]^{-1}\sqrt{e_m^{n+1}}^2 -$$

$$\frac{\rho_B b_1(B_1 + S_1)}{(1+b_2Ri)}\left[\frac{\rho_m}{(a_1)^{3/2}} + \frac{\rho_B b_1}{(1+b_2Ri)}\right]^{-1}\sqrt{e_m^{n+1}} -$$

$$\left(\frac{\sqrt{e_m^n}^2\Delta p_m}{\Delta p_m g} + B_0 + S_0\right)\left[\frac{\rho_m}{(a_1)^{3/2}} + \frac{\rho_B b_1}{(1+b_2Ri)}\right]^{-1} = 0. \tag{3.e.3}$$

49

This is a backward (implicit) finite difference equation just as was used for the potential temperature and mixing ratio equations, however, it is also a cubic equation whose three roots (one always real, other two complex conjugates or real) are equal to $\sqrt{e_m^{n+1}}$. When $E \geq 0$ the model solves this cubic equation and the square of the solution that is always real is assigned to e_m^{n+1}.

When the entrainment rate is less than zero, the TKE at the next time step is determined by applying a backward (implicit) scheme to the top equation of (2.a.(6)(b).4), $g^{-1}\Delta p_m \dfrac{\partial e_m}{\partial t} = weight(B_0 + S_0 - D)$, where $D = \dfrac{\rho_m}{(a_1)^{\frac{3}{2}}}\sqrt{e_m^n}\,e_m^{n+1}$. Here the dissipation is written in partially implicit form so the finite difference scheme can be solved without using a cubic equation. As with the forward scheme used for the momentum equations, this partial implicit representation still provides a stable solution. Thus, the equation for the TKE with $E < 0$ is

$$\frac{e_m^{n+1} - e_m^n}{\Delta t} = \frac{weight}{g\Delta p_m}\left(B_0 + S_0 - \frac{\rho_m}{(a_1)^{\frac{3}{2}}}\sqrt{e_m^n}\,e_m^{n+1}\right)$$

or

$$e_m^{n+1} = \frac{e_m^n + \dfrac{weight\Delta t}{g\Delta p_m}(B_0 + S_0)}{1 + \dfrac{weight\Delta t \rho_m \sqrt{e_m^n}}{g\Delta p_m (a_1)^{\frac{3}{2}}}} \tag{3.e.3a}$$

4. Simulations

A short description of the Wangara dataset is provided in the next section. The Wangara data is used to validate the model and study the clear convective boundary layer. The last section in this chapter briefly describes the ocean experiment. The ocean simulation is designed to study steady-state conditions in the PBL.

4.a. Land Simulation

The Wangara dataset was compiled by Clarke et. al. (1971). It consists of 44 days of boundary layer data from 15 July to 27 August, 1967. The data was obtained from the area around Hay, Australia located at 34°30'S, 144°56'W. The data collection project was given the name "Wangara", which means "west wind". Day 33 of the Wangara dataset was used for the land simulation.

Day 33 was characterized by clear skies, negligible advection of heat and moisture, and high pressure. The nearest front was over 1000 km away. These conditions proved perfect for study of the clear convective boundary layer. This particular day has been widely used in boundary layer studies because of these ideal conditions and the readily available data.

The data includes temperature and mixing ratio soundings every three hours from the surface to 2000 meters. Soundings of the u and v components of the wind are provided every hour from the surface to 2000 meters. The resolution of this sounding data is every 50 meters from the surface to 1000 meters, and every 100 meters for the remainder. The ground temperature and the geostrophic wind are provided once an hour. Clarke provides additional data that is not used in this model.

4.b. Ocean Simulation

The data required is minimal since steady-state solutions are sought for the ocean simulation. A constant sea surface temperature (SST) is specified. The surface mixing ratio is computed based on the SST. The mixing ratio at the top of the PBL is fixed. The

initial air temperature is specified to provide a positive surface heat flux at the start of the simulation. The surface winds and the geostrophic winds are set to constants. The potential temperature and winds at the top of the PBL are determined based on their surface values and constant lapse rates. Finally, a divergence is specified to balance the entrainment rate in the PBL depth prediction equation.

5. One-Layer Model Prognostic Results

5.a. Wangara Experiments

5.a.(1) Twenty-four Hour Simulation

A 24-hour simulation using the Wangara Day 33 data was run to predict the diurnal variation of the prognostic variables. The dissipation fraction (see Table 2.a.(6).1) and the fraction of TKE production due to the local rate of change of TKE when the entrainment rate is less than zero (Section 2.a.(6)(b)) were set to 0.90. The simulation was started at 0900L with a time step of 60 seconds. A cooling rate of $2°$ day^{-1} was applied to the predicted mixed layer potential temperature. The initial PBL depth was set to 18 mb ($\approx$120 meters). The initial TKE was set to 0.2 m^2 s^{-2}. The Coriolis parameter, f, is equal to -8.26 10^{-5} s^{-1} for Wangara.

Figure 5.a.(1).1 shows the diurnal change of the PBL depth. The abscissa indicates the number of minutes into the simulation after the start time.

Wangara PBL Depth
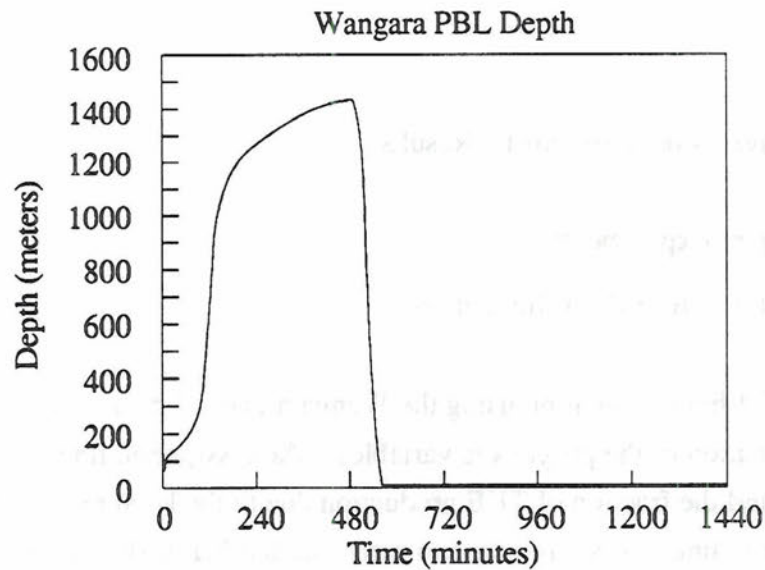
Figure 5.a.(1).1: Predicted Diurnal Δz_m for Wangara Day 33.

This profile is typical of a clear convective boundary layer (CBL). At the start of the simulation during the early morning a strong inversion exists just above the surface. The boundary layer is shallow at this time (≈ 100 meters). The strong inversion present during the early morning acts to suppress the buoyancy. Since buoyancy is the driving force in CBLs, the boundary layer grows slowly during this initial stage.

As the surface heating increases, the lapse rate transitions from stable to unstable. The air just above the surface warms enough to remove the existing low-level inversion. Figure 5.a.(1).2 shows $\theta_m - \theta_{S-}$ and $\theta_{B+} - \theta_m$. The first difference is a measure of the strength of the surface inversion and the second difference the strength of the PBL top inversion.
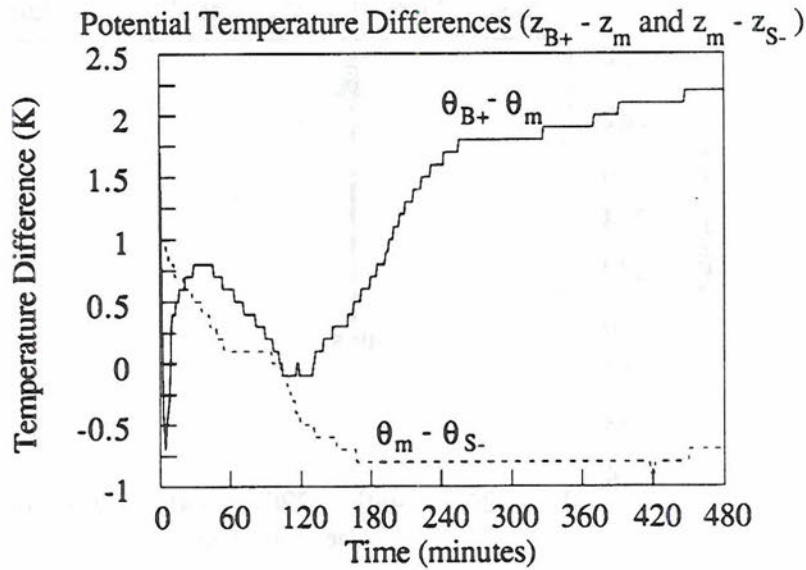
Figure 5.a.(1).2: Diurnal $\theta_m - \theta_{s-}$ and $\theta_{B+} - \theta_m$ for Wangara Day 33.

The surface heating becomes strong enough to remove the surface inversion after about 100 minutes. This marks the second stage when rapid boundary layer growth takes place. At this time strong heating at the surface creates buoyant thermals which rise. The near-surface lapse rate is now superadiabatic which results in an unstable boundary layer. This allows the thermals to continue to rise until they reach the inversion marking the present height of the PBL. The large amount of buoyancy at this time of day creates vigorous mixing, hence the name mixed layer. This causes the conservative variables to become nearly uniform with height in the mixed layer. The predicted diurnal variation of the mixed layer prognostic variables are shown in Figures 5.a.(1).3-5.a.(1).6.

Wangara Mixed Layer Potential Temperature
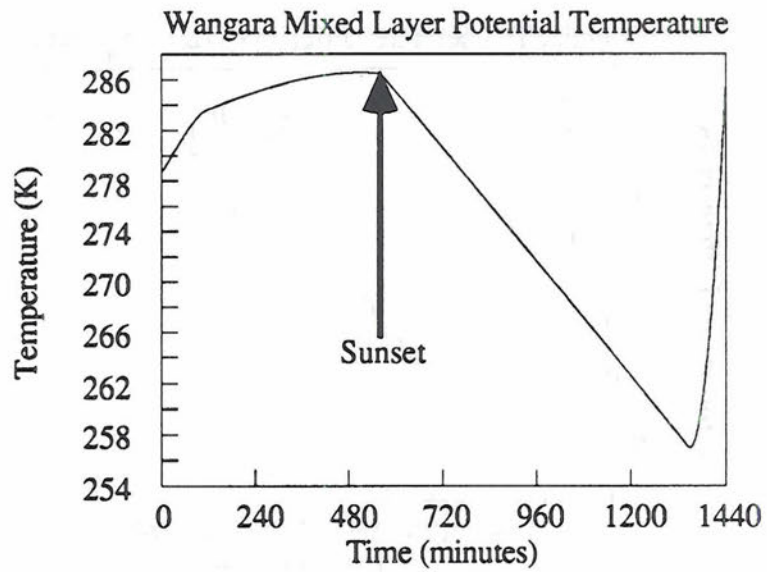
Figure 5.a.(1).3: Predicted Diurnal θ_m for Wangara Day 33.

Wangara Mixed Layer Mixing Ratio
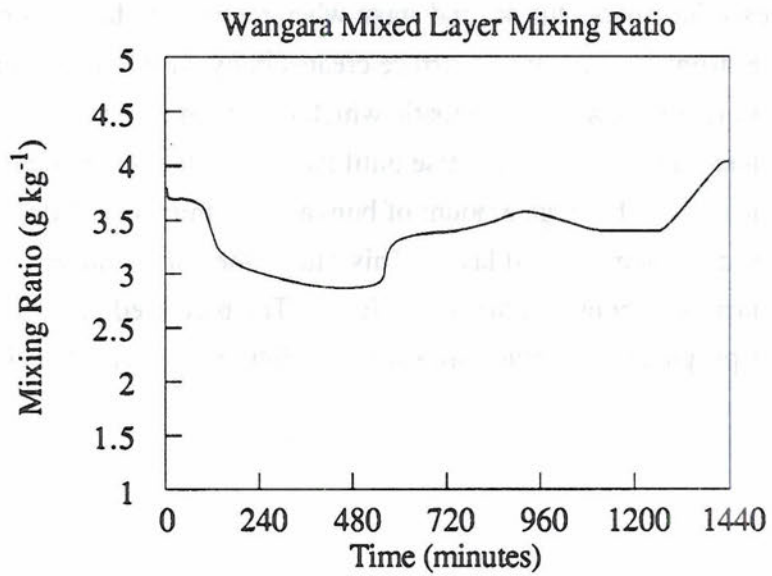
Figure 5.a.(1).4: Predicted Diurnal q_m for Wangara Day 33.

Wangara Mixed Layer Horizontal Velocity
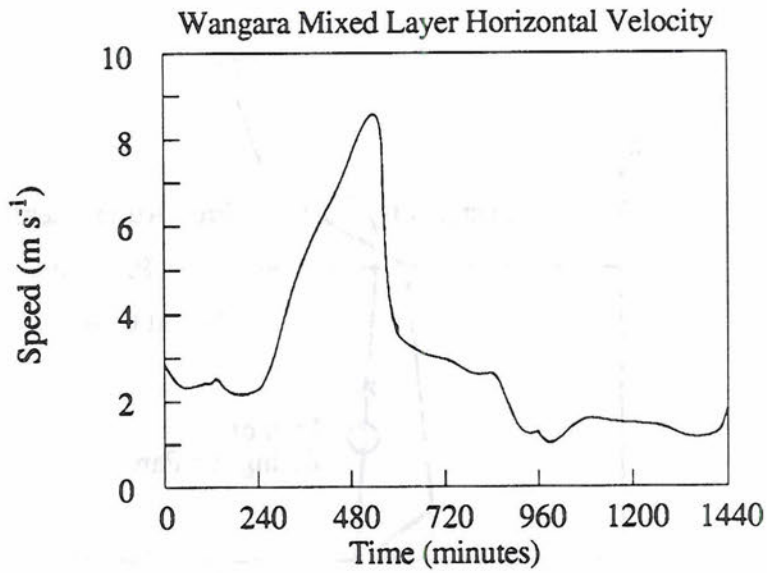
Figure 5.a.(1).5: Predicted Diurnal $|v_m|$ for Wangara Day 33.

Wangara Mixed Layer Turbulence Kinetic Energy
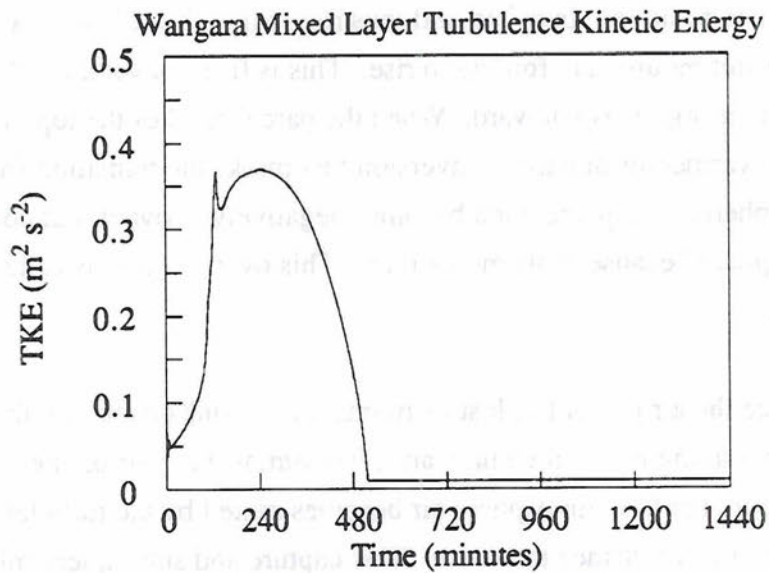
Figure 5.a.(1).6: Predicted Diurnal e_m for Wangara Day 33.

As the morning progresses and the boundary layer becomes deeper, growth occurs not only due to buoyancy, but also because warm free-atmosphere air is entrained into the top of the PBL. This air is mixed by the turbulence within the PBL causing the

PBL to grow. Entrainment arises because of penetrative convection. This is illustrated in Figure 5.a.(1).7.
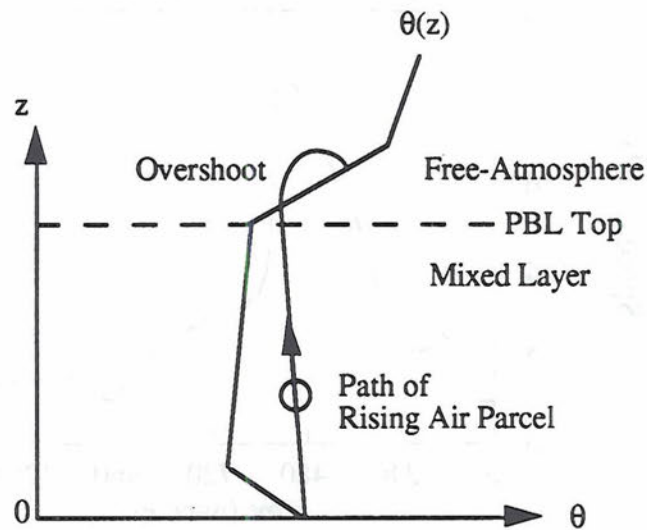
Figure 5.a.(1).7: Illustration of the Process of Penetrative Convection (Stull, 1991).

An air parcel in the mixed layer that is initially warmer than the mean potential temperature is positively buoyant, and thus rises through the layer. At this point the parcel does not require any forcing to rise. This is free-convection where the parcel gains momentum during its trip upward. When the parcel reaches the top of the PBL, it encounters warmer air due to the inversion that marks the transition from mixed layer to free-atmosphere. The parcel then becomes negatively buoyant, but continues to rise into free-atmosphere because of its momentum. This overshooting is called penetrative convection.

Once the air parcel has lost its momentum it sinks back into the mixed layer. The parcel carries along non-turbulent, warm, free-atmosphere air on the return trip. The positively buoyant free-atmosphere air becomes mixed by the turbulence in the mixed layer before it has a chance to escape. This capture and subsequent mixing of warm free-atmosphere air is the process of entrainment. Since less turbulent air is entrained into more turbulent air, entrainment only occurs in one direction -- down into the PBL.

Mechanical mixing caused by wind shear at the surface and top of the PBL also causes PBL growth, but this process is less important in a clear CBL over land. This is shown by Figure 5.a.(1).8.

58
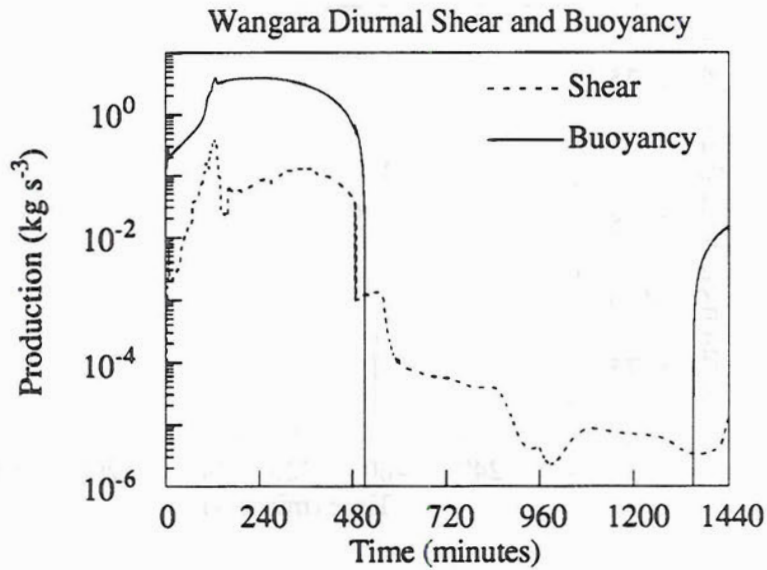
Figure 5.a.(1).8: Diurnal B and S Wangara Day 33.

During the rapid PBL growth period, buoyancy production is an order of magnitude larger than shear production. Both buoyancy and shear production in this figure take into account the contribution due to entrainment when E>0. Shear production becomes important at night when buoyancy production is negative. Shear-generated turbulence may cause the nocturnal boundary layer to grow.

The predicted diurnal change in the entrainment rate is shown in Figure 5.a.(1).9. By mid morning when the PBL has rapidly grown to about 1 km, the entrainment rate has increased dramatically. This gives an indication that entrainment is an important mechanism for boundary layer growth.
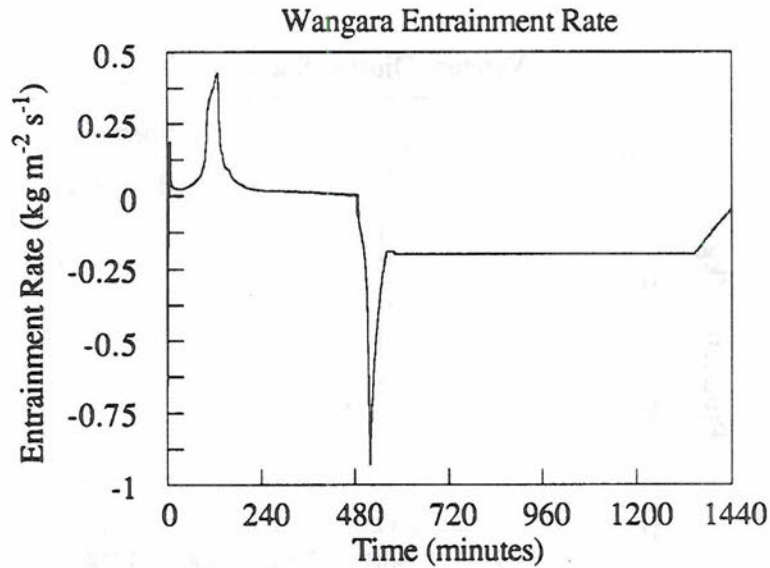
Figure 5.a.(1).9: Predicted Diurnal E Wangara Day 33.

The rapid decrease in PBL growth marks the third stage of the diurnal transition of the mixed layer. At this point rising thermals meet resistance upon reaching the base of the inversion at the top of the PBL. The inversion has increased in strength as indicated in Figure 5.a.(1).2 which makes it more difficult for penetrative convection to occur. Buoyancy production is no longer as effective in a deep boundary layer as it was when the PBL was shallow. The boundary layer continues to grow, however growth is much slower. As Figure 5.a.(1).9 shows, the entrainment rate rapidly drops off by early afternoon which coincides with the much slower growth rate of the PBL during this period.

The final stage in the transition of the mixed layer occurs around sunset. With the loss of daytime heating, buoyancy production rapidly approaches zero. This marks the decay of turbulence in the mixed layer. The TKE is no longer maintained by buoyant production, and is rapidly dissipated. The mixed layer then becomes decoupled from the surface. Since the sum of the buoyancy and shear is now less than the dissipation, the entrainment rate is allowed to become negative. This has the effect of "crashing" the mixed layer.

The mixed layer depth decreases to its preset minimum of 10 meters shortly after sunset. The mixed layer potential temperature decreases continuously until sunrise due to the constant downward heat flux and a constant prescribed radiative cooling. The TKE decreases at sunset and remains at its prescribed minimum of $1 \ 10^{-2} \ m^2 \ s^{-2}$ during the night.

With negative buoyancy production and insufficient shear production, the entrainment rate remains negative, but it approaches zero after sunrise when the buoyancy production becomes positive. The boundary layer is expected to grow at night due to shear generated turbulence and other factors. There appears to be a problem with the negative entrainment parameterization because it does not allow PBL growth during the night.

5.a.(2) Seventy-two Hour Simulation

The model was then run for 72 hours to test the response to repeat use of the Wangara Day 33 data. It was expected that the prognostic variable profiles would look very similar from day-to-day. Slight variations were considered acceptable because the initial conditions at model start time, 0900L Day 1, would not be the same as the predicted conditions 24 hours later, 0900L Day 2. These predicted conditions could be considered the "new" initial conditions at the start of the second day. Figure 5.a.(2).1 shows the mixed layer PBL depth as a representative profile. The profile is consistent from Day 1 through Day 3. Although not shown, the other prognostic variables were also consistent throughout the simulation.
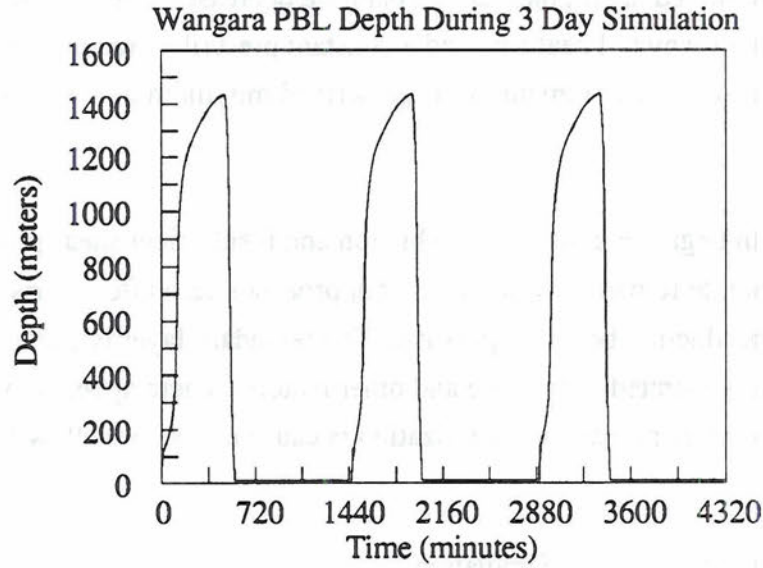
Figure 5.a.(2).1: Predicted 3 Day Δz_m Reusing Wangara Day 33 Data Each Day.

5.b. Ocean Experiment

The ocean experiment was designed to obtain steady-state solutions since no database was used for this simulation. The initialization of the prognostic variables is detailed in Table 2.b.1. Constants required to initialize the prognostic variables are listed in Table 2.b.2. A 100 hour simulation was run to allow the variables to reach equilibrium. The PBL depth prediction equation requires a non-zero divergence to balance a positive entrainment rate when equilibrium has been reached. The steady-state form of this equation is

$$\Delta p_m = \frac{gE}{\nabla \bullet v_m}.$$

(5.b.1)

A divergence of 4 10^{-6} s^{-1} was used for this experiment.

Figure 5.b.1 shows the convergence of the PBL depth completely to its steady-state value by 100 hours. At equilibrium, the local rate of change terms in the prediction equations are zero. As a check, the steady-state solution for one of the prognostic variables can be determined by setting the local term in the prediction equation to zero,

62

thus obtaining an equation for the variable in terms of diagnostic variables. The solution to this equation should equal the value of the variable predicted by the model.
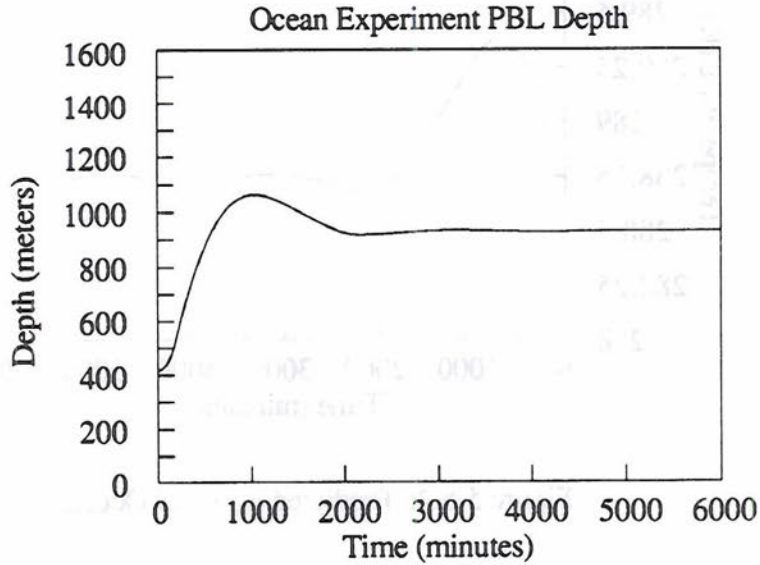
Figure 5.b.1: Predicted Δz_m Over Ocean.

Figures 5.b.2-5.b.5 show the progression of the other prognostic variables to their equilibrium values. The steady-state equation for the potential temperature is

$$\theta_m = \frac{E\bar{\theta}_{B+} + V\bar{\theta}_{S-}}{E + V}. \tag{5.b.2}$$

If E>>V then the mixed layer potential temperature will reach the temperature at the PBL top in equilibrium. This shows that entrainment dominates. If E<<V then the mixed layer potential temperature will reach the temperature at the PBL surface in equilibrium. In this case, the surface heating dominates.

Using the values of the potential temperature at the top and surface of the PBL ($\bar{\theta}_{B+} = 291.93\ K$ and $\bar{\theta}_{S-} = 288.79\ K$), and the values of E = 4.38 10^{-3} kg m^{-2} s^{-1} and V = 2.36 10^{-2} kg m^{-2} s^{-1} at t=6000 minutes, equation (5.b.2) gives$\theta_m = 288.79\ K$. This compares almost exactly with $\theta_m = 288.75\ K$ at t=6000 minutes from Figure 5.b.2.

63
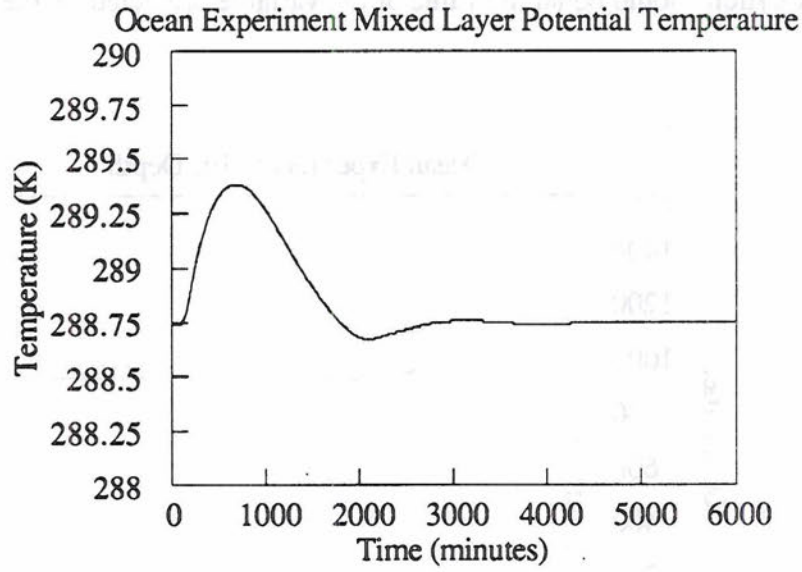
Figure 5.b.2: Predicted θ_m Over Ocean.
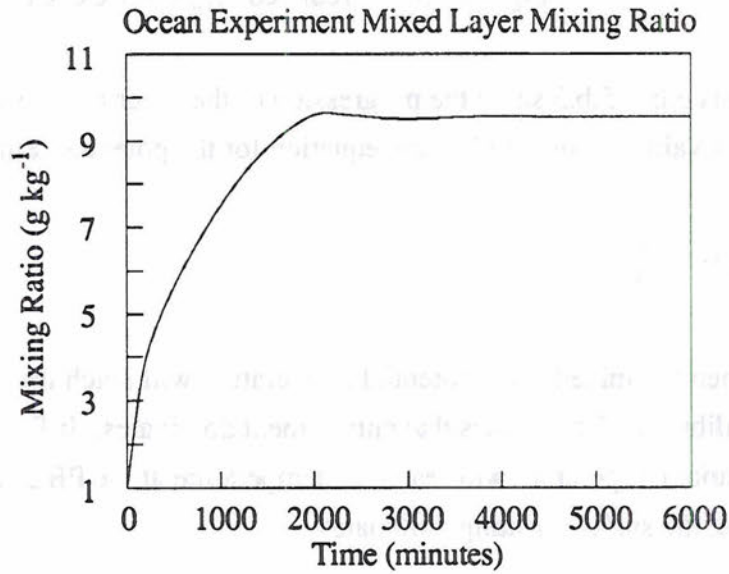
Figure 5.b.3: Predicted q_m Over Ocean.

64

Ocean Experiment Mixed Layer Horizontal Velocity
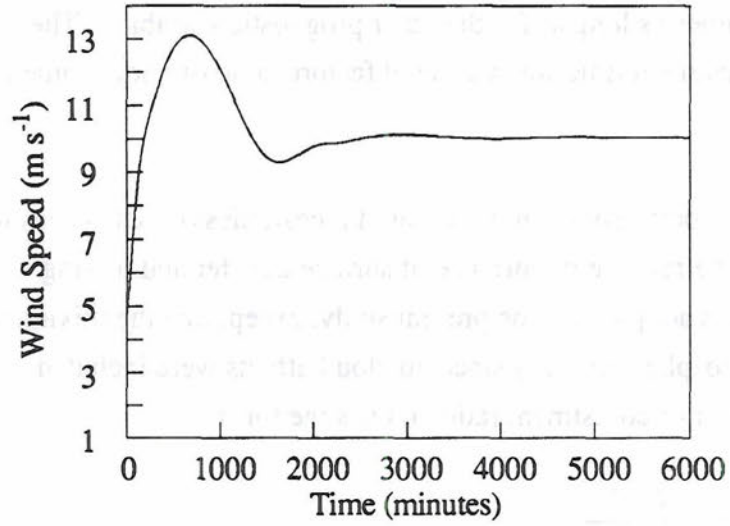
Figure 5.b.4: Predicted $|v_m|$ Over Ocean.

Ocean Experiment Mixed Layer Turbulence Kinetic Energy
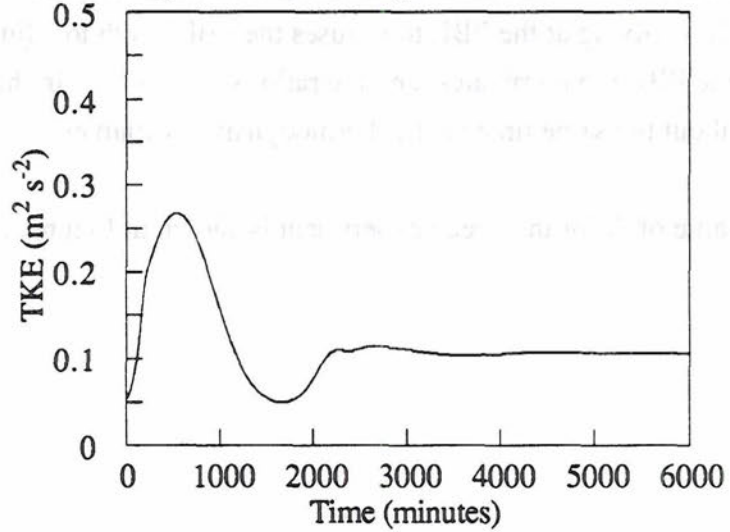
Figure 5.b.5: Predicted e_m Over Ocean.

According to Figures 5.b.1-5.b.5, all the prognostic variables reach equilibrium about the same time. Schubert et al. (1979) developed a coupled, convective-radiative, boundary layer model and performed several ocean simulations where they varied the sea

65

surface temperature (SST), the divergence, or both. In one experiment, the SST was increased instantaneously from 14°C to 16°C, and the divergence was held constant at 4 10^{-6} s^{-1}. They found the adjustment time for the PBL depth to reach steady-state was about 20 times as long as for the other prognostic variables. They concluded that the longer adjustment time was a general feature, at least under some typical eastern ocean situations.

In Schubert's study an important dimensionless quantity was introduced that measured the relative importance of surface transfer and mixing across cloud top. This quantity was adopted for the present study, except that the mixing was due to entrainment of free-atmosphere air only since no cloud effects were included. This quantity can be thought of as an adjustment ratio and has the form

$$A = \frac{C_T V}{D z_B + \frac{dz_B}{dt}},$$ (5.b.3)

where C_T is the surface transfer coefficient, V the surface wind speed, D the divergence, and z_B the height of the PBL in meters. If surface transfer dominates then the ratio is large (about 4 or 5). The surface forcings rapidly adjust the thermodynamic variables, while the slow mixing at the PBL top causes the PBL depth to adjust slowly. If the mixing at the PBL top dominates then the ratio is small (<1). In this case, the PBL depth adjusts in about the same time as the thermodynamic variables.

The value of A for the ocean experiment is shown in Figure 5.b.6.
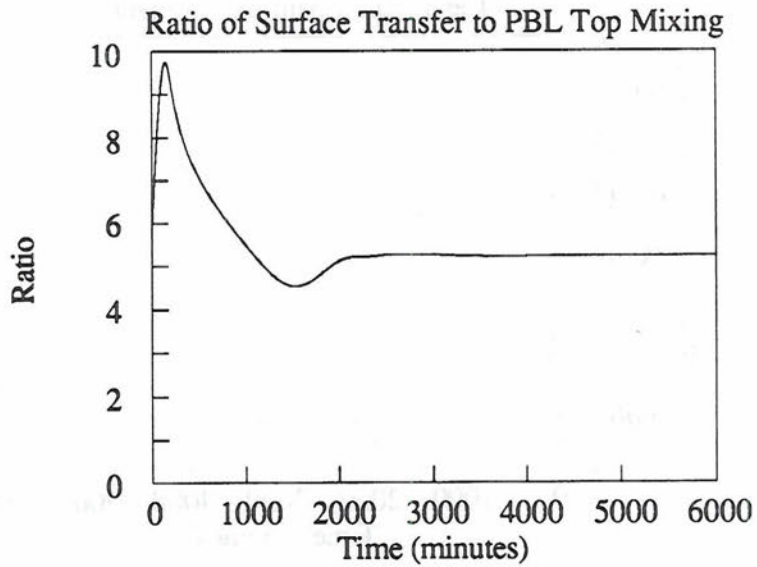
Figure 5.b.6: A for Ocean Experiment.

The ratio was never less than about 4.5 which would indicate that the PBL depth takes much longer to adjust than the other prognostic variables.

This discrepancy is resolved by comparing the entrainment rate in the ocean experiment with the one used in the Schubert study. Figure 5.b.7 depicts E for the ocean experiment.
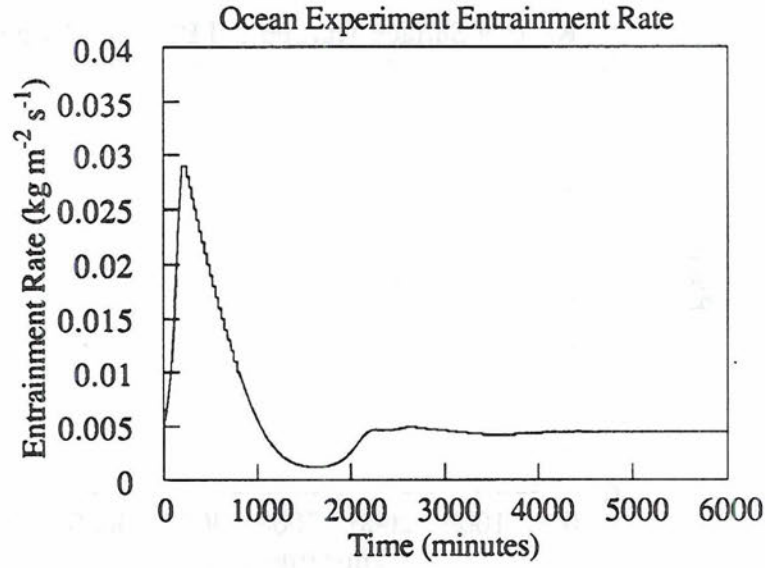
Figure 5.b.7: E for Ocean Experiment.

At equilibrium the entrainment rate was small, but for the initial portion of the simulation the entrainment rate became very large. However, in Schubert's study the entrainment rate remained at a constant small value for the entire simulation. The parameterization for E used in the present experiment caused E to become large enough so that the PBL depth adjusted rapidly.

If one assumes that the equilibrium value of E obtained in the ocean experiment was the value of E for the entire simulation, then the adjustment time for the PBL is obtained by solving the differential equation for the PBL depth, $\frac{\partial \Delta p_m}{\partial t} = \Delta p_m (\nabla \bullet v_m) + gE$. The solution to this equation with the divergence and E constant is

$$\Delta p_m = \frac{gE}{\nabla \bullet v_m}\left[1 - e^{-(\nabla \bullet v_m)t_{e-fold}}\right] + (\Delta p_m)_0 e^{-(\nabla \bullet v_m)t_{e-fold}}, \tag{5.b.4}$$

where t_{e-fold} is the e-folding time (time for variable to decrease to 1/e of its original value) and $(\Delta p_m)_0$ is the initial PBL depth. As $t_{e-fold} \to \infty$ the PBL depth reaches its equilibrium value of $\Delta p_m = \frac{gE}{\nabla \bullet v_m}$. Equation (5.b.4) can be manipulated to get a relation for t_{e-fold}.

This relation is

$$t_{e-fold} = \frac{ln\left\{\left(\Delta p_m - \frac{gE}{\nabla \bullet v_m}\right) \Big/ \left[(\Delta p_m)_0 - \frac{gE}{\nabla \bullet v_m}\right]\right\}}{-\nabla \bullet v_m}.$$ (5.b.5)

The e-folding time obtained with E at its steady state value of 4.382529×10^{-3} kg m^{-2} s^{-1}, a divergence of 4×10^{-6} s^{-1}, an initial depth of 5817.8 Pa and a final depth of 10736.5 Pa was 25.6 days. The adjustment time is approximately 3 times t_{e-fold} which is about 77 days.

This is about 18 times as long as the PBL depth actually took to adjust in the ocean experiment which corresponds excellently with the Schubert study. This shows that the differences in E between the present study and Schubert's study are the key to the rapid adjustment of the PBL in the present study.

6. One-Layer Model Diagnostic Discussion

This chapter provides a brief overview of diagnostic variables determined in the model following Randall et al. (1992). These variables include the fractional area covered by rising motion, σ, the convective mass flux, M_c, plume-scale variance transport, $\overline{\rho w' \psi' \psi'}$ (where ψ is an arbritary scalar such as the potential temperature or water vapor mixing ratio), value of ψ at levels S and B for upward and downward moving parcels, $(\psi_{u \text{ or } d})_{S \text{ or } B}$, dissipation time scale, τ_{dis}, dissipation rate of ψ at levels S and B, $(\psi_{dis})_{S \text{ or } B}$, vertical gradient of $\overline{\psi}$, $\dfrac{\partial \overline{\psi}}{\partial z}$, surface transfer coefficients, C_T and $C_{T'}$,

Richardson number, and Richardson number limits.

6.a. Convective Mass Flux Model

The scalar, ψ satisfies the conservation equation

$$\frac{\partial(\rho\psi)}{\partial t} = -\nabla \bullet (\rho v \psi) - \frac{\partial}{\partial z}(\rho w \psi) + S_\psi, \tag{6.a.1}$$

where the local change and the del operator are defined on constant height surfaces, and S_ψ is the source of ψ per unit mass per unit time. The area average of the scalar is given by

$$\overline{\psi} = \psi_u \sigma + \psi_d (1 - \sigma), \tag{6.a.2}$$

and the upward turbulent flux of ψ is

$$F_\psi = \rho\overline{w'\psi'} = \rho\left[(w_u - \overline{w})(\psi_u - \overline{\psi})\sigma + (w_d - \overline{w})(\psi_d - \overline{\psi})(1 - \sigma)\right]$$
$$or \tag{6.a.3}$$
$$F_\psi = M_C(\psi_u - \psi_d),$$

where the convective mass flux is defined as

$$M_C \equiv \rho\sigma(1-\sigma)(w_u - w_d). \tag{6.a.4}$$

The convective mass flux can not be determined by the model using (6.a.4) because the vertical velocities of upward and downward moving parcels are not known nor predicted. The convective mass flux can also be written in terms of the fractional area covered by rising motion and the turbulence kinetic energy. The former is diagnostically determined (see Section 6.c) using the entrainment rate and ventilation mass flux which are calculated by the model, and the latter is predicted by the model. The definition (6.a.4) is useful, however, in developing an equation for the plume-scale variance.

The plume-scale variance transport is

$$\overline{\rho w' \psi' \psi'} = \rho\left[\sigma(w_u - \overline{w})(\psi_u - \overline{\psi})^2 + (1-\sigma)(w_d - \overline{w})(\psi_d - \overline{\psi})^2\right],$$

or using (6.a.2) where w=ψ,

$$\overline{\rho w' \psi' \psi'} = \rho\sigma(1-\sigma)(1-2\sigma)(w_u - w_d)(\psi_u - \psi_d)^2,$$

or using (6.a.3) and (6.a.4),

$$\overline{\rho w' \psi' \psi'} = (1-2\sigma)\frac{(F_\psi)^2}{M_C}. \tag{6.a.5}$$

Equations for ψ_u and ψ_d are obtained by substituting (6.a.3) into (6.a.2) after rearrangement which gives

$$\psi_u = \overline{\psi} + \frac{(1-\sigma)}{M_C}(F_\psi) \tag{6.a.6}$$

and

$$\psi_d = \overline{\psi} - \frac{\sigma}{M_C}(F_\psi). \tag{6.a.7}$$

6.b. Matching Convective Mass Flux with Ventilation and Entrainment Mass Flux

For the ventilation layer, the bulk aerodynamic formula used by the model is

$$(F_\psi)_S = V(\overline{\psi}_{S-} - \overline{\psi}_S). \tag{6.b.1}$$

The ventilation mass flux can be matched to the convective mass flux at the top of the ventilation layer (at level S) with the following assumptions: (1) The fluxes at the top of the ventilation layer are entirely due to convective circulations, and the small-eddy fluxes are negligible at S. This is a typical assumption in the boundary layer where the small eddies are important very near the surface (viscous dissipation, $Re = \dfrac{UL}{v} \approx 1$, where U is the horizontal velocity, L is the length scale of the eddy, and v is the viscosity), but in most of the surface layer the Reynolds number is large (since U and L are large and v is small compared to their values in the viscous sublayer) and viscous effects are no longer important. (2) The ventilation layer is thin (the model assumes the ventilation and entrainment layers are infinitesimal). The ventilation mass flux can then be matched to the convective mass flux at level S with these assumptions and equation (6.a.3). This gives

$$V(\overline{\psi}_{S-} - \overline{\psi}_S) = M_{c,S}(\psi_u - \psi_d)_S. \tag{6.b.2}$$

Since the small eddies are important near the surface, they will dilute air that rises from the surface and air that descends from the interior of the PBL. To account for this mixing, a mixing parameter, χ_V, is used so that

$$(\psi_u)_S - \overline{\psi}_S = \chi_V(\overline{\psi}_{S-} - \overline{\psi}_S), \tag{6.b.3}$$

where $0 \le \chi_V \le 1$. When the mixing parameter equals 1, no mixing occurs by the small eddies and $(\psi_u)_S = \overline{\psi}_{S-}$. Mixing by the small eddies increases as the mixing parameter decreases from 1. Using (6.a.2), (6.b.2) and (6.b.3) results in

$$\chi_V \frac{M_{c,S}}{V} = 1 - \sigma_S \tag{6.b.4}$$

A similar matching of the fluxes in the entrainment layer at level B leads to

$$\chi_E \frac{M_{C,B}}{E} = \sigma_B. \tag{6.b.5}$$

Now, if M_C and σ are assumed to be independent of height then (6.b.4) and (6.b.5) can be combined to give

$$\sigma = \frac{1}{1 + \frac{E}{V} \frac{\chi_V}{\chi_E}}. \tag{6.b.6}$$

An equation for M_C in terms of the entrainment rate, the ventilation mass flux, and the mixing parameters is obtained by inserting (6.b.6) into (6.b.4) or (6.b.5) which gives

$$M_C = \frac{(E/\chi_E)(V/\chi_V)}{(E/\chi_E) + (V/\chi_V)}. \tag{6.b.7}$$

The model does not determine σ or M_C using equations (6.b.6) and (6.b.7) because it does not contain a parameterization for the mixing parameters. The next section presents an equation for M_C in terms of σ and the TKE. This equation is equated with (6.b.7) to deduce a parameterization for the mixing parameters where they are equal to the same quantity. The parameterization is not applied directly by the model, but is used to simplify (6.b.6).

6.c. Diagnostic Equations for M_C and σ Using the TKE

Assuming the density of air is approximately constant with height in the PBL (since the PBL depth is typically only 1-2 km), the vertically averaged TKE (e_m) is related to the variance of the vertical velocity by

$$a_3 e_m \rho_m \Delta z = \frac{1}{2} \rho_m \int_{z=z_{S-}}^{z=z_{B+}} \overline{w'^2} dz, \tag{6.c.1}$$

where $a_3 = 0.316$. This equation is simply $\dfrac{Kinetic\ Energy}{area} = \dfrac{\frac{1}{2}mv^2}{area}$.

Now, the variance of the vertical velocity is written

$$\overline{w'^2} = \sigma(1-\sigma)(w_u - w_d)^2,$$

or using (6.a.4),

$$\overline{w'^2} = \frac{M_C^2}{\rho_m^2 \sigma(1-\sigma)}. \tag{6.c.2}$$

All the quantities on the right hand side of (6.c.2) are assumed to be independent of height. Then, substituting this equation into (6.c.1) and integrating gives

$$a_3 e_m \rho_m \Delta z = \frac{1}{2} \frac{M_C^2}{\rho_m^2 \sigma(1-\sigma)} \rho_m \Delta z,$$

or

$$M_C = \rho_m \sqrt{2a_3 \sigma(1-\sigma)e_m}. \tag{6.c.3}$$

Once the final equation for σ is determined then M_C can be calculated using (6.c.3).

Setting equation (6.c.3) and (6.b.7) equal to each other results in

$$\frac{(E/\chi_E)(V/\chi_V)}{(E/\chi_E)+(V/\chi_V)} = \rho_m \sqrt{2a_3 \sigma(1-\sigma)e_m}. \tag{6.c.4}$$

Then substituting for σ using (6.b.6) to obtain

$$\chi_V \chi_E = \frac{EV}{2\rho_m^2 a_3 e_m}. \tag{6.c.5}$$

A plausible parameterization for the mixing parameters based on (6.c.5) is then

$$\chi_V = \chi_E = \sqrt{\frac{EV}{2\rho_m^2 a_3 e_m}}.$$ (6.c.6)

Finally with this parameterization, (6.b.6) reduces to

$$\sigma = \frac{1}{1 + \frac{E}{V}}.$$ (6.c.7)

The model calculates the entrainment rate and the ventilation mass flux, and then (6.c.7) and (6.c.3) are used to determine σ and M_C.

6.d. PBL Interior Diagnostics

The balance for the variance of ψ in the PBL interior is written

$$\frac{\partial}{\partial t}\overline{\psi'^2} = -2\frac{F_\psi}{\rho}\frac{\partial \overline{\psi}}{\partial z} - \frac{1}{\rho}\frac{\partial}{\partial z}\left(\rho\overline{w'\psi'\psi'}\right) - 2\varepsilon_\psi,$$ (6.d.1)

where the local change of the variance is due to production of variance, vertical transport of variance, and dissipation of variance (see (6.d.3)). Advection by the mean flow has been ignored and ψ is assumed to be a conservative variable. The variance is given by

$$\overline{\psi'^2} = \sigma(1-\sigma)(\psi_u - \psi_d)^2,$$

or using (6.a.3),

$$\overline{\psi'^2} = \sigma(1-\sigma)\left(\frac{F_\psi}{M_C}\right)^2.$$ (6.d.2)

The triple correlation portion of the triple correlation term is just the plume-scale variance transport (6.a.5). The dissipation rate used by the model is

$$\varepsilon_\psi = \frac{\overline{\psi'^2}}{\tau_{dis}} = \frac{\sigma(1-\sigma)}{\tau_{dis}}\left(\frac{F_\psi}{M_C}\right)^2.$$

or

75

$$\varepsilon_\psi = \frac{\sigma(1-\sigma)(1-2\sigma)^2}{\hat{\tau}}\left(\frac{F_\psi}{M_C}\right)^2,$$ (6.d.3)

where $\quad \tau_{dis} = \dfrac{\hat{\tau}}{(1-2\sigma)^2}.$ (6.d.4)

Equation (6.d.4) is used to calculate the dissipation time scale for ψ based on σ and the parameter, $\hat{\tau}$, which is set during a model simulation. The model determines the dissipation rate of the variance of ψ using the lower equation of (6.d.3).

The last diagnostic to be determined in this section is the vertical gradient of ψ. Writing (6.d.1) using (6.d.2), the plume-scale variance transport, and the top equation of (6.d.3) gives

$$\frac{\partial}{\partial t}\left[\sigma(1-\sigma)\left(\frac{F_\psi}{M_C}\right)^2\right] = -2\frac{F_\psi}{\rho}\frac{\partial\overline{\psi}}{\partial z} -$$

$$\frac{M_C(1-2\sigma)}{\sigma(1-\sigma)}\frac{1}{\rho}\frac{\partial}{\partial z}\left[\sigma(1-\sigma)\left(\frac{F_\psi}{M_C}\right)^2\right] -.$$ (6.d.5)

$$\frac{2\sigma(1-\sigma)}{\tau_{dis}}\left(\frac{F_\psi}{M_C}\right)^2$$

An equilibrium solution to (6.d.5) can be found by setting the local time derivative to zero. The equation then contains a first order derivative in z which requires only a single boundary condition to solve. The boundary condition is applied at level S if $\sigma<1/2$ (boundary layer driven by surface heating), and at level B if $\sigma>1/2$ (boundary layer driven by entrainment). To satisfy both (6.b.1) (surface flux) and $\left(F_\psi\right)_B = -E\left(\overline{\psi}_{B+} - \overline{\psi}_B\right)$ an additional condition must be specified. Choosing $\dfrac{\partial\overline{\psi}}{\partial z}$ to be constant with height will force the differential equation to be satisfied at both boundaries.

Using the hydrostatic equation and the conditions above, (6.d.5) becomes

$$\frac{(1-2\sigma)}{M_C}\left(\frac{\partial F_\psi}{\partial p} - \frac{F_\psi}{\delta p_*}\right) = -\frac{\partial\overline{\psi}}{\partial p},$$ (6.d.6)

where $\quad \delta p_* = \dfrac{gM_C \hat{\tau}}{\sigma(1-\sigma)(1-2\sigma)}.$ $\hfill$ (6.d.7)

Then, using the surface and top fluxes as boundary conditions, the solution of (6.d.6) is

$$F_\psi = \frac{(F_\psi)_S \left[1 - exp\left(\dfrac{p - p_B}{\delta p_*} \right) \right] + (F_\psi)_B \left[exp\left(\dfrac{p - p_B}{\delta p_*} \right) - exp\left(\dfrac{\Delta p_m}{\delta p_*} \right) \right]}{1 - exp\left(\dfrac{\Delta p_m}{\delta p_*} \right)}, \hfill (6.d.8)$$

where $\quad \dfrac{\partial \overline{\psi}}{\partial p} = \dfrac{(1-2\sigma)}{M_C \delta p_*} \left[\dfrac{(F_\psi)_S - (F_\psi)_B \, exp\left(\dfrac{\Delta p_m}{\delta p_*} \right)}{1 - exp\left(\dfrac{\Delta p_m}{\delta p_*} \right)} \right]. \hfill (6.d.9)$

Equation (6.d.9) is used by the one-layer model to obtain the vertical gradient of ψ.

$\qquad$ Assuming σ is close to 1/2 and using the binomial expansion, equations (6.d.8) and ((6.d.9)) become

$$F_\psi \approx (F_\psi)_B \left(\dfrac{p_S - p}{\Delta p_m} \right) + (F_\psi)_S \left(\dfrac{p - p_B}{\Delta p_m} \right) +$$
$$\hfill (6.d.10)$$
$$\dfrac{1}{2} \left(\dfrac{\Delta p_m}{\delta p_*} \right) \left(\dfrac{p - p_B}{\Delta p_m} \right) \left(\dfrac{p_S - p}{\Delta p_m} \right) \left[(F_\psi)_B - (F_\psi)_S \right],$$

and

$$\dfrac{\partial \overline{\psi}}{\partial p} \approx \dfrac{g\hat{\tau}}{\sigma(1-\sigma)(\Delta p_m)^2} \left(\dfrac{\Delta p_m}{\delta p_*} \right) \left[(F_\psi)_B - (F_\psi)_S \right] + \dfrac{1}{2} \left(\dfrac{\Delta p_m}{\delta p_*} \right) \left[(F_\psi)_B - (F_\psi)_S \right]. \quad (6.d.11)$$

Equation (6.d.10) is an approximation to (6.d.8) keeping first order terms. Equation ((6.d.11)) is an approximation to (6.d.9) keeping second order terms. Then, if $\left| (F_\psi)_S \right| \gg \left| (F_\psi)_B \right|$, which is typically true in a convective boundary layer, ((6.d.11) reduces to

$$\frac{\partial \overline{\psi}}{\partial p} \approx \frac{-g\hat{\tau}}{\sigma(1-\sigma)(\Delta p_m)^2}\left(\frac{\Delta p_m}{\delta p_\bullet}\right)(F_\psi)_s.$$ (6.d.12)

The vertical gradient of $\overline{\theta}$ is also determined by (6.d.12) in the one-layer model.

6.e. Surface Transfer Coefficient Using TKE

The bulk aerodynamic formula, $(F_\psi)_s = V(\overline{\psi}_{s-} - \overline{\psi}_s)$, can be written by specifying the ventilation mass flux (V) using the surface density, surface wind speed, and a surface transfer coefficient

$$V = \rho_s C_T |v_m|.$$ (6.e.1)

Based on Randall and Shao (1990), the ventilation mass flux can be related to the TKE by

$$V = \rho_s C_{T'} \sqrt{e_m}.$$ (6.e.2)

In (6.e.2), the square root of the TKE is 'acting' as the velocity. Since turbulent flux requires TKE and V is a measure of this flux at the surface, it seems reasonable that V is proportional to $\sqrt{e_m}$. Another reason to favor (6.e.2) over (6.e.1) is that turbulence can occur in the absence of a mean wind (i.e., when there is positive buoyancy production). As long as TKE exists, (6.e.2) will determine V regardless of the value of the mean wind. Both C_T and $C_{T'}$ are determined by the model using (6.e.1) and (6.e.2) respectively.

6.f. Richardson Number and Limits

The Richardson number is determined using the equation listed in Section 2.a.(6)(a). This equation is

$$Ri = \frac{g\left[(\overline{\theta}_{B+})_v - (\theta_m)_v\right]\Delta z_m}{(\theta_m)_v e_m}.$$ (6.f.1)

When the inversion is strong, Ri>>1 then

$$\lim_{Ri \to \infty} = \frac{Ec_p\left(\dfrac{p_B}{p_o}\right)^{\kappa}\left[(\overline{\theta}_{B+})_v - (\theta_m)_v\right]}{(F_{sv})_S} = 0.2,$$ (6.f.2)

where c_p is the specific heat of air at constant pressure.

When there is no inversion, Ri=0 (see equation (2.a.(6)(a).7)) then

$$\lim_{Ri=0} = \frac{E}{\rho_B b_1 \sqrt{e_m}} = 1.$$ (6.f.3)

The strong and no inversion limits are determined by the model using (6.f.2) and (6.f.3) respectively.

7. One-Layer Model Diagnostic Results

Results are provided covering the convective growth period of the Wangara Day 33 simulation. This period is roughly from 0900L to 1600L, and includes rapid growth of the PBL during the mid-morning and slower growth during the afternoon. The results point out the importance of buoyancy and entrainment in the growth of a clear convective PBL when the PBL top is below a weak or non-existent inversion. During the afternoon when the inversion is strong, surface heating is still significant which continues creating a large amount of buoyancy, but this buoyancy is largely ineffective in penetrating the inversion layer. The strong inversion layer also limits the entrainment rate. The small amount of entrainment present is largely balanced against subsidence, hence the PBL is quasi-steady-state during the afternoon. Results are also shown for the steady-state ocean experiment.

7.a. Wangara Results for the Fractional Area Covered by Rising Motion

Figure 7.a.1 shows the fractional area covered by rising motion, σ, as a function of time.
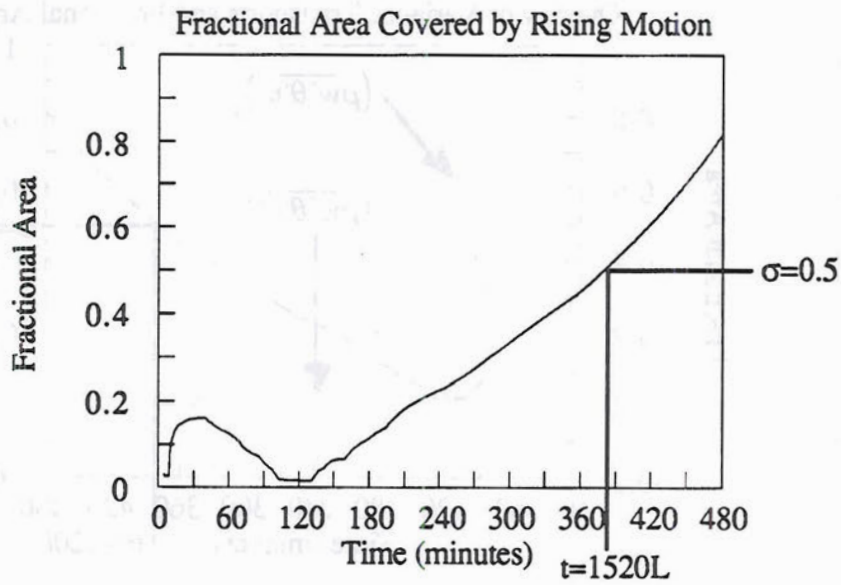
Figure 7.a.1: σ for Wangara Day 33 0900-1600L.

By mid-morning, $\sigma \ll 1$ which is when rapid PBL growth is occurring. After 1200L, σ increases steadily as convective growth begins to diminish. The fractional area exceeds 0.5 after 1520L. At this time convection is no longer significantly affecting the PBL depth.

In Figure 7.a.2 the plume-scale variance transport of the potential temperature at levels S and B has been overlaid with σ.
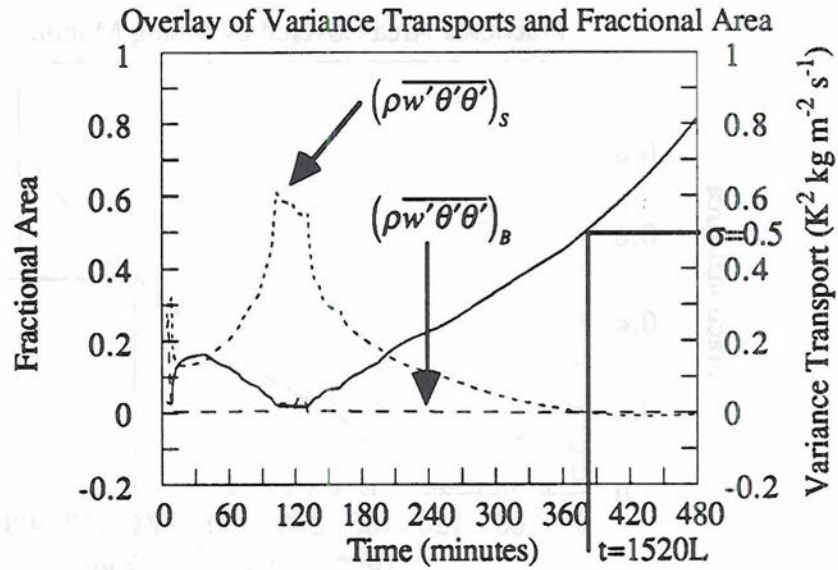
Figure 7.a.2: $\left(\rho\overline{w'\theta'\theta'}\right)_S$, $\left(\rho\overline{w'\theta'\theta'}\right)_B$, and σ for Wangara Day 33 0900-1600L.

It is clear from the figure that the plume-scale variance transport of θ at level S dominates during rapid convective growth when $\sigma\ll 1$. While $\sigma<1/2$, $\left(\rho\overline{w'\theta'\theta'}\right)_S > 0$ which indicates the surface is transporting variance upwards. When σ equals 1/2, both $\left(\rho\overline{w'\theta'\theta'}\right)_S$ and $\left(\rho\overline{w'\theta'\theta'}\right)_B$ are zero. Finally, when σ exceeds 1/2, $\left(\rho\overline{w'\theta'\theta'}\right)_S$ and $\left(\rho\overline{w'\theta'\theta'}\right)_B$ are less than zero. At this point the entrainment layer is exporting variance downward into the PBL. This variance export balances subsidence keeping the PBL in a quasi-steady-state.

The convective mass flux is shown in Figure 7.a.3. The minimum occurs when $\sigma\ll 1$, and the maximum occurs when $\sigma=1/2$ while the TKE is still large. M_C is small when the convection is intense because $M_C \propto \sqrt{\sigma(1-\sigma)}$. As σ increases and the TKE decreases during the late afternoon, M_C decreases.

82

Convective Mass Flux
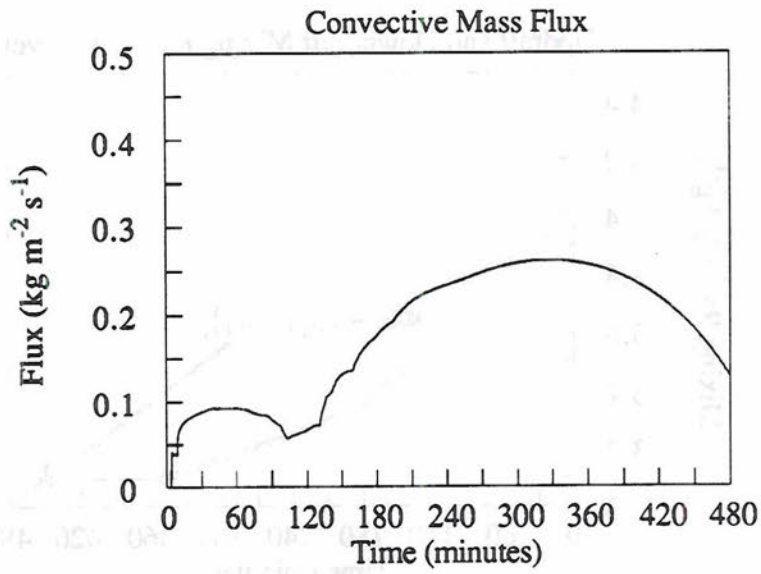
Figure 7.a.3: M_C for Wangara Day 33 0900-1600L.

The updraft (u) and downdraft (d) properties of θ and q at level S are depicted in Figures 7.a.4 and 7.a.5.

Updraft and Downdraft Potential Temperatures at Level S
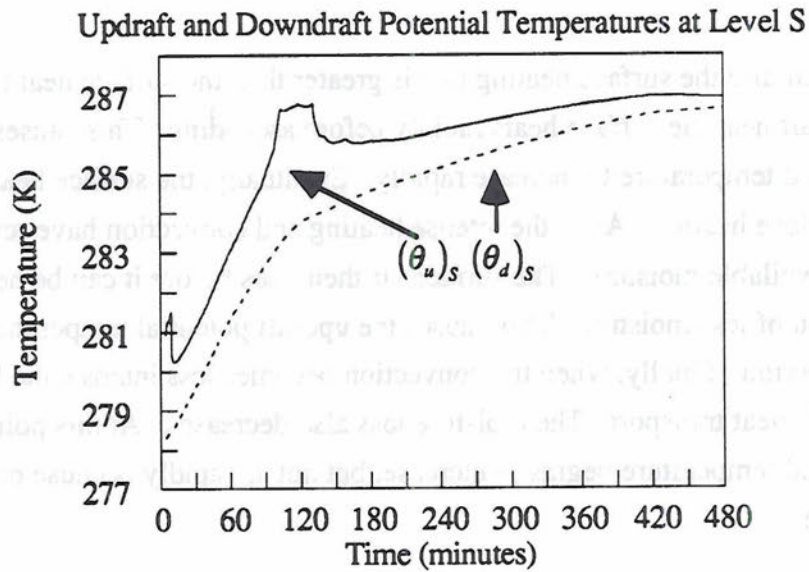
Figure 7.a.4: $(\theta_u)_S$ and $(\theta_d)_S$ for Wangara Day 33 0900-1600L.

83
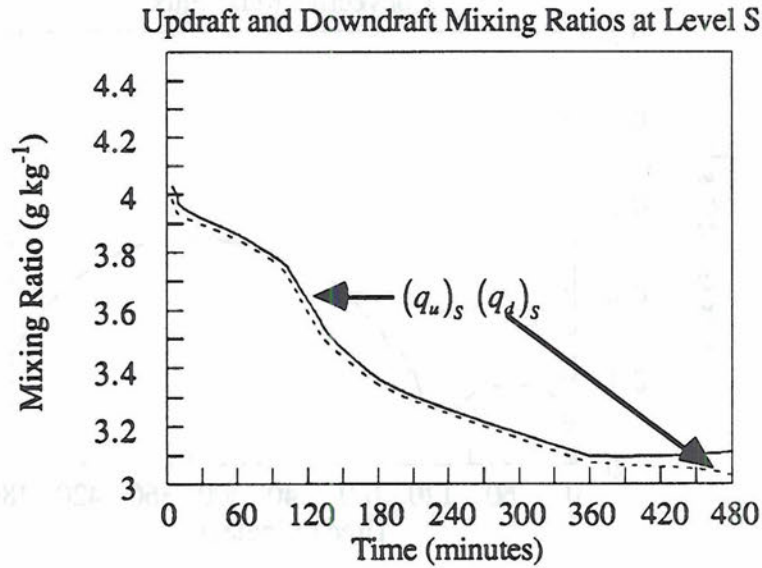
Figure 7.a.5: $(q_u)_s$ and $(q_d)_s$ for Wangara Day 33 0900-1600L.

These figures indicate that the updrafts are warmer and wetter than the downdrafts. The boundary layer is being heated from the surface, and the highest amount of moisture is near the surface. Hence, the updrafts which are coming from a region that is warm and moist, should be warm and wet compared to the downdrafts which come from a relatively dry and cool region.

Initially the surface heating rate is greater than the surface heat transport. Thus, rising air near the surface heats rapidly before ascending. This causes the updraft potential temperature to increase rapidly. Eventually, the surface heat transport exceeds the surface heating. Also, the intense heating and convection have removed some low-level available moisture. The surface air then rises before it can be heated, and it rises in a region of less moisture. This causes the updraft potential temperature to decrease for a short period. Finally, when the convection becomes less intense, the heating rate again exceeds heat transport. The moisture loss also decreases. At this point the updraft potential temperature begins to increase, but not as rapidly because of less intense surface heating.

84

The downdraft potential temperature increases rapidly in the morning when the heating is intense and the heat transport is rapid. Heat is brought quickly into the source region of the downdrafts. Initially, moisture is also brought into this source region. In the afternoon, as the surface heating decreases and moisture is carried away from the source region, the downdraft potential temperature increases much more slowly.

Figures 7.a.6 and 7.a.7 show the updraft and downdraft properties at level B.
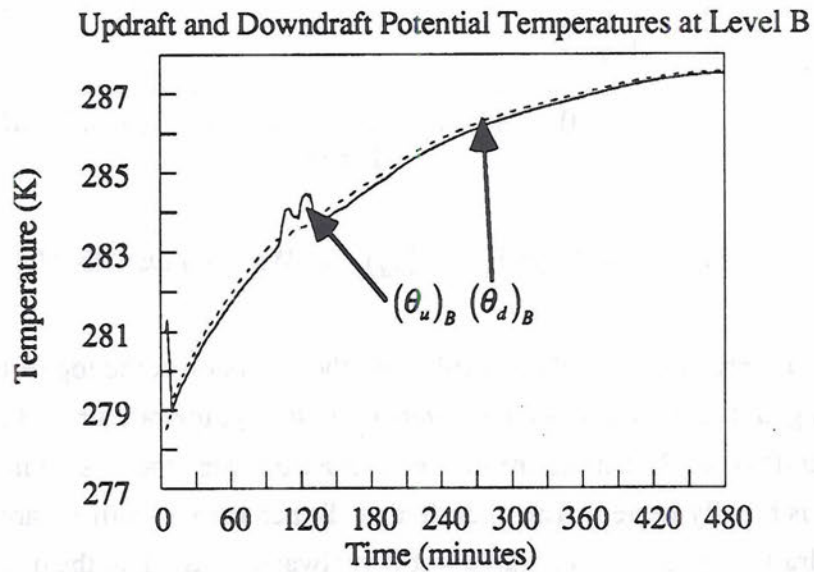
Figure 7.a.6: $(\theta_u)_B$ and $(\theta_d)_B$ for Wangara Day 33 0900-1600L.
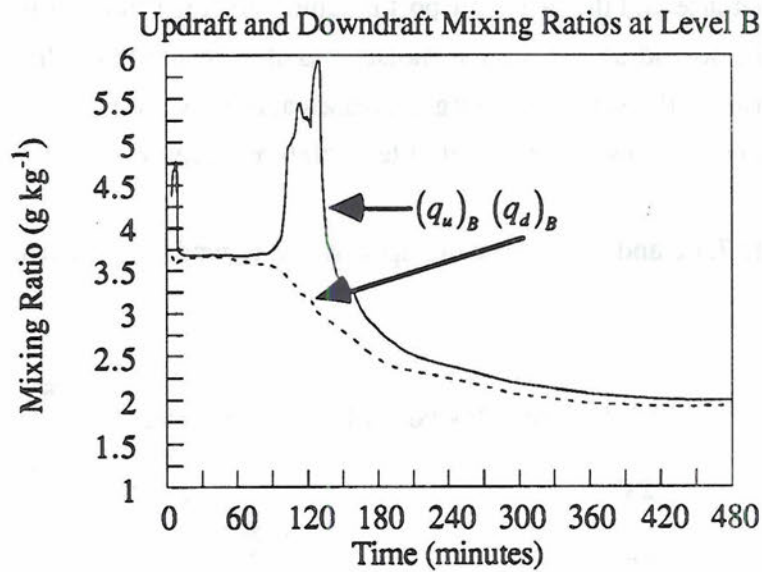
Figure 7.a.7: $(q_u)_B$ and $(q_d)_B$ for Wangara Day 33 0900-1600L.

These properties are largely controlled by the inversion at the top of the PBL. In the morning and afternoon when the inversion is strong, updraft air at B is cooler than downdraft air at B. During the convective period when there is no inversion, the air from below is rapidly heated. The updraft air at B then comes from a warmer source than the downdraft air at B. The updraft air at B is always wetter than the downdraft air. The updraft mixing ratio increases rapidly to a high value for a short time when the vertical moisture transport is large during convection. Mixing brings this large value back down. Both the updraft and downdraft mixing ratios decrease in the afternoon because the sources of moisture from above and below decrease due to heating and mixing.

7.b. Wangara PBL Interior Results

Interior results were obtained for the convective period of Wangara Day 33 using four different values of $\hat{\tau}$. Dissipation rates for θ and q and the dissipation time scale were determined with $\hat{\tau}$ set to 1 second. These diagnostics are just $\hat{\tau}$ times their values at $\hat{\tau} = 1$ second for other settings of $\hat{\tau}$. Figure 7.b.1 shows the dissipation time scale.

86
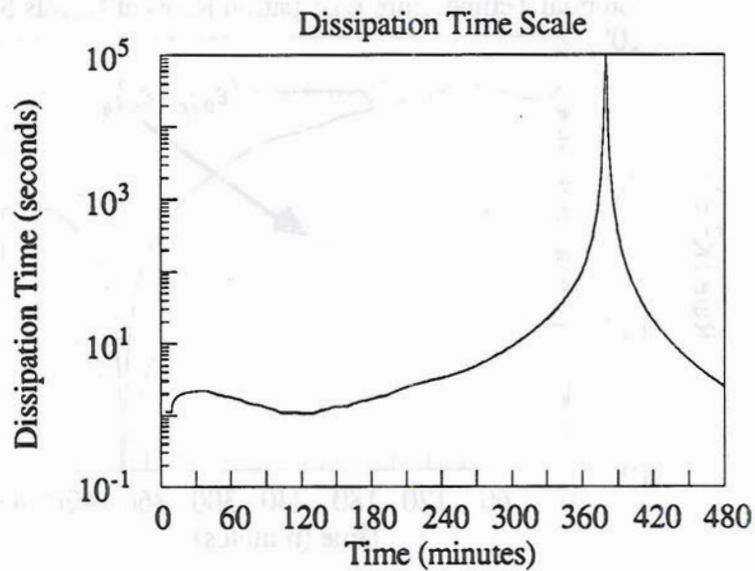
Figure 7.b.1: τ_{dis} for Wangara Day 33 0900-1600L.

The minimum in τ_{dis} occurs during the maximum convection around 1100L when $\sigma \ll 1$. This is when the surface heating is the most intense and when the smaller eddies would be the most effective. As $\sigma \to 1/2$ during the afternoon the PBL becomes more mixed. The variance transports decrease and the time scale for dissipation increases. When $\sigma = 1/2$ at 1520L $\tau_{dis} \to \infty$, hence the sharp peak in the figure.

Figures 7.b.2 and 7.b.3 contain ε_θ and ε_q at levels S and B.

Potential Temperature Dissipation Rates at Levels S and B
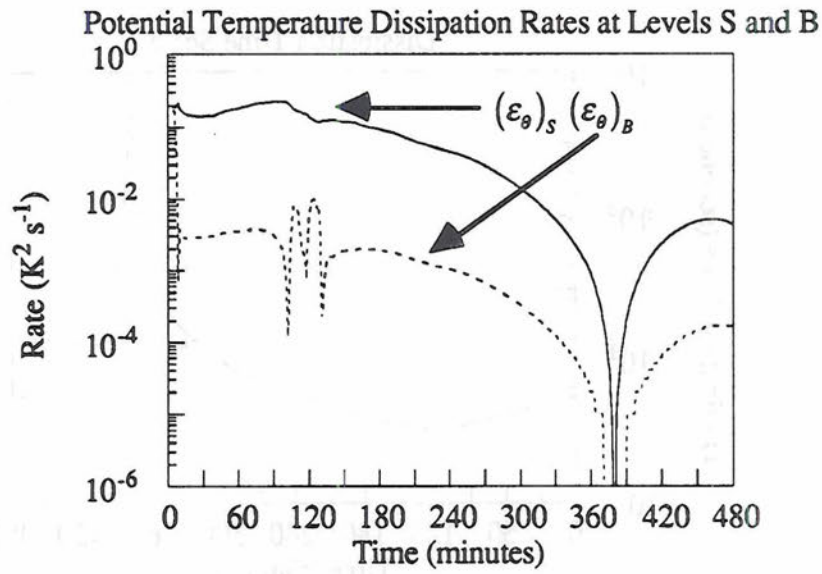
Figure 7.b.2: $(\varepsilon_\theta)_S$ and $(\varepsilon_\theta)_B$ for Wangara Day 33 0900-1600L.

Mixing Ratio Dissipation Rates at Levels S and B
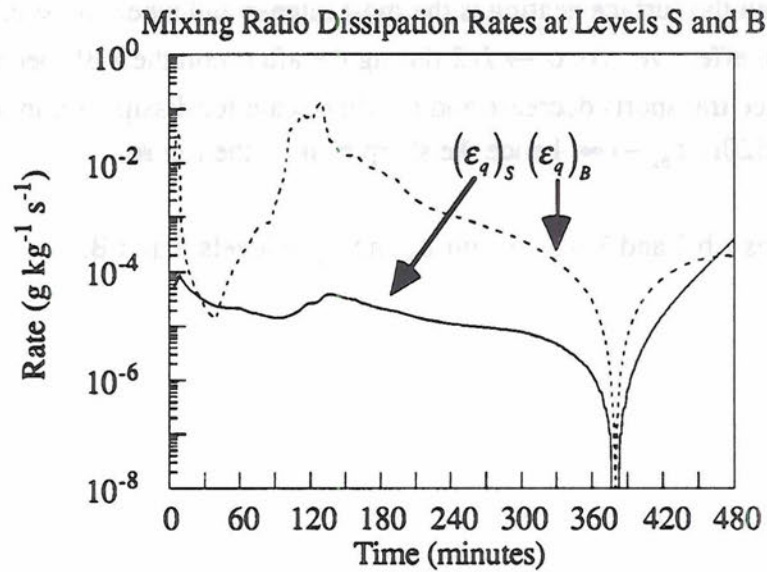
Figure 7.b.3: $(\varepsilon_q)_S$ and $(\varepsilon_q)_B$ for Wangara Day 33 0900-1600L.

The dissipation rates are highest when the fluxes are the largest during mid-morning rapid growth. For the potential temperature the surface flux dominates over the flux at B due to

88

surface heating, thus the potential temperature dissipation rate at S is much greater than at B. For the mixing ratio the opposite is true. The large entrainment rate present when rapid growth is occurring causes the mixing ratio flux at B to be much greater than at S. All the dissipation rates approach zero as $\sigma \rightarrow 1/2$.

The next set of figures shows the gradients of $\bar{\theta}$ and $\bar{q}$ with height using $\hat{\tau}$ equal to 10, 100, and 1000 seconds. The gradients for $\hat{\tau} = 1$ second are not included because they are too large. The gradient profiles of $\bar{\theta}$ are in Figure 7.b.4.
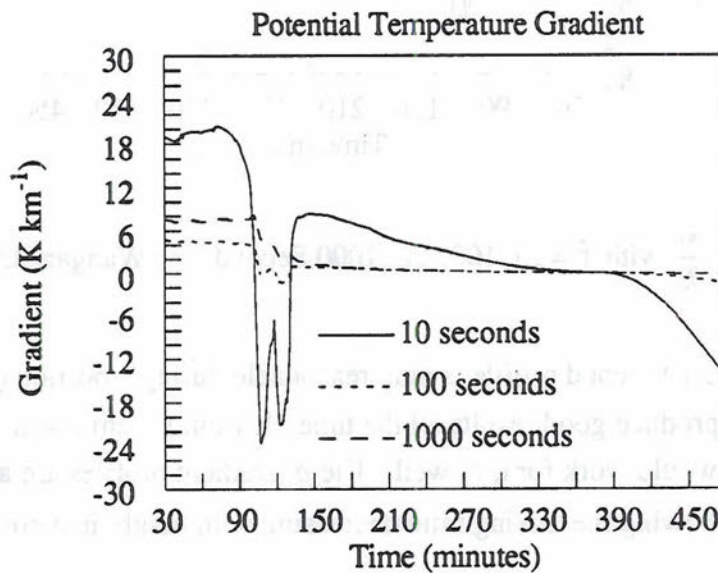
Figure 7.b.4: $\dfrac{\partial \bar{\theta}}{\partial z}$ with $\hat{\tau} = 10$, 100, and 1000 Seconds for Wangara Day 33 0930-1600L.

The gradient of $\bar{\theta}$ with $\hat{\tau} = 10$ seconds seems reasonable between 210 and 420 minutes based on the actual Wangara temperature profile. The other gradients look plausible during the entire period, but the gradient with $\hat{\tau} = 1000$ seconds is the most representative. This is particularly true during the convective growth period when this gradient indicates the potential temperature is increasing with height. Observations have verified that the upward heat flux is countergradient (Wyngaard and Brost 1984). Based on the Wangara data and the gradient profiles shown, $\hat{\tau}$ should be between 100 and 1000 seconds for typical convective boundary layers.

Figure 7.b.5 gives a similar set of gradient profiles for the mixing ratio.
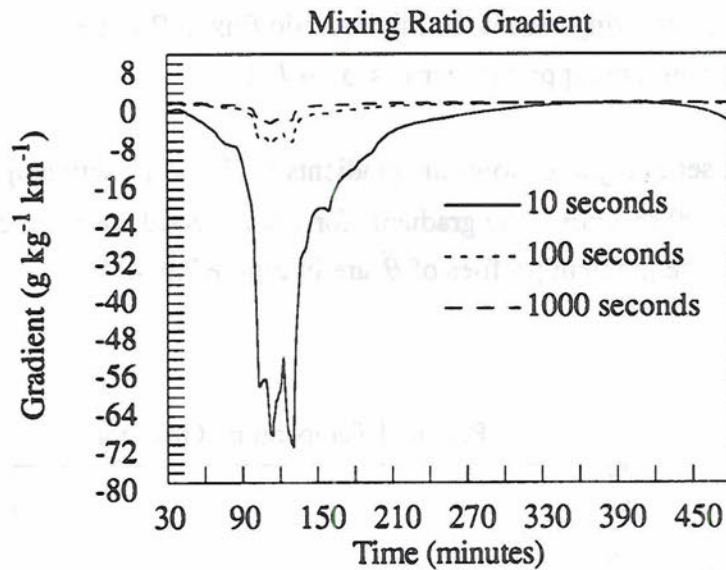
Figure 7.b.5 $\frac{\partial \bar{q}}{\partial z}$ with $\hat{\tau} = 10$, 100, and 1000 Seconds for Wangara Day 33 0930-1600L.

Here again, the 10 second profile is only reasonable during a portion of the period. The other profiles produce good results all the time. It would seem that a $\hat{\tau}$ between 100 and 1000 seconds would work for q as well. The $\bar{q}$ gradient profiles are also consistent with observations showing the mixing ratio decreasing with height in a convective PBL.

The gradient of $\bar{\theta}$ was also determined using equation (6.d.12). The gradient using (6.d.12) is independent of $\hat{\tau}$ because the $\hat{\tau}$ in the numerator of (6.d.12) cancels out with the $\hat{\tau}$ in the denominator (part of the δp. term). Figure x shows this gradient.

90

Potential Temperature Gradient Using Equation (6.d.12)
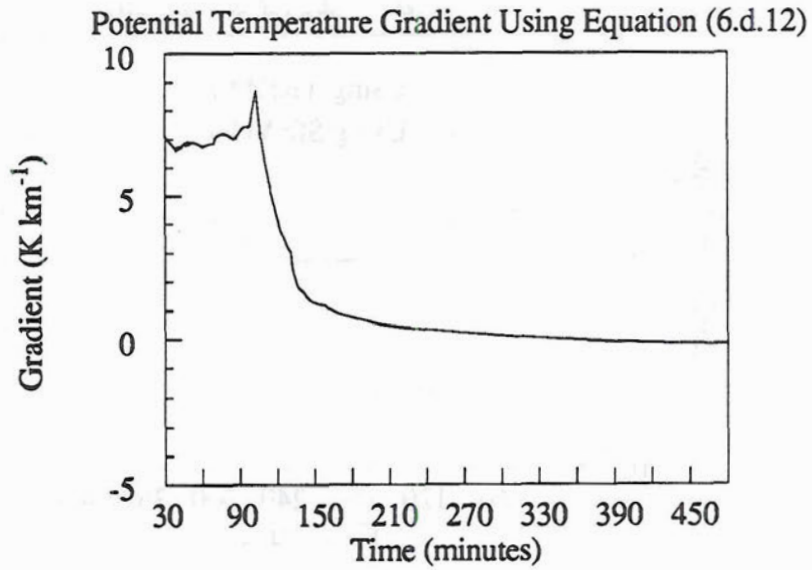
Figure 7.b.6: $\dfrac{\partial \bar{\theta}}{\partial z}$ Using (6.d.12) for Wangara Day 33 0930-1600L.

This profile looks reasonable at all times and it shows the large gradient during the morning before the PBL has become mixed, rapid decrease in the gradient during the mid-morning convective period, and the near zero gradient in the afternoon after mixing has occurred.

7.c. Wangara Surface Transfer Coefficients

Figure 7.c.1 is a comparison of the surface transfer coefficient computed by using the surface velocity with the coefficient calculated using the square root of the TKE.

91
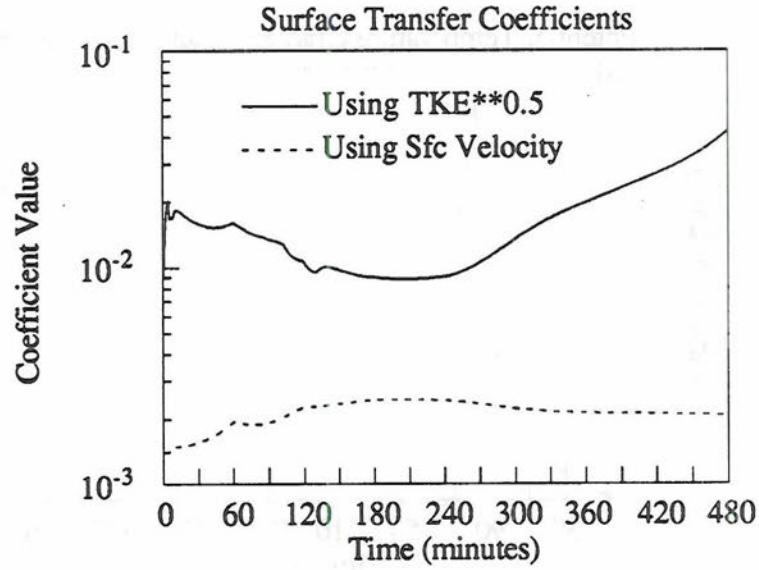
Figure 7.c.1: C_T and $C_{T'}$ for Wangara Day 33 0900-1600L.

The transfer coefficient computed using $\sqrt{e_m}$ is about an order of magnitude larger than the coefficient computed using $|v_m|$ since the square root of the TKE is about 1/10 of the surface velocity. The minimum occurs in this coefficient when e_m is at its maximum value from mid-morning through early afternoon.

Figure 7.c.2 shows a scatter plot of $C_{T'}$ versus the negative of a bulk Richardson number defined by

$$Ri_{Bulk} \equiv -\left\{ \frac{g\left[(\theta_v)_{S-} - (\theta_v)_m\right]\Delta z_m}{(\theta_v)_{S-} e_m} \right\} \qquad (7.c.1)$$

92

Transfer Coefficient (for TKE) Versus Negative Bulk Ri
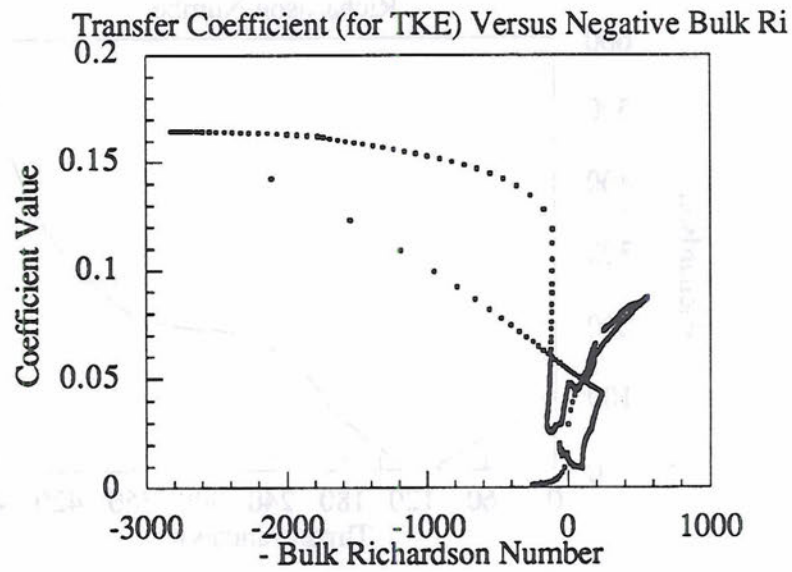
Figure 7.c.2: Scatter Plot of $C_{T'}$ Versus $-Ri_{Bulk}$ for Wangara Day 33 0900-1600L.

There appears to be a relationship between $C_{T'}$ and the bulk Richardson number. The figure indicates that there are two families of curves which likely means that $C_{T'}$ also depends on another variable.

7.d. Wangara Calculation of Richardson Number and Limits

A plot of the Richardson number is shown in Figure 7.d.1.
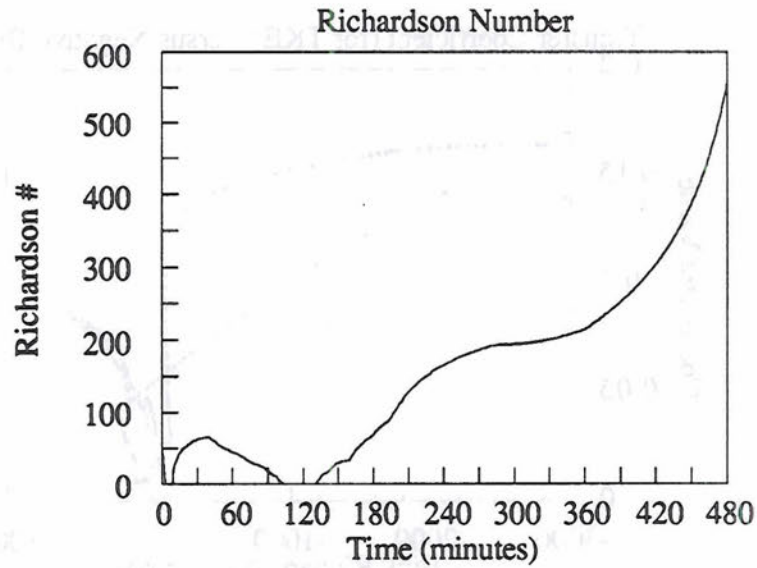
Figure 7.d.1: Ri for Wangara Day 33 0900-1600L.

The Richardson number is zero during the unstable convective growth period when there is no inversion. At this time, the limit when Ri=0 should be 1. As the PBL becomes well mixed during the late afternoon the inversion strengthens. The Richardson number increases as a result. The limit for Ri>>1 should approach 0.2 by late afternoon. Figures 7.d.2 and 7.d.3 are plots of the limits.

94
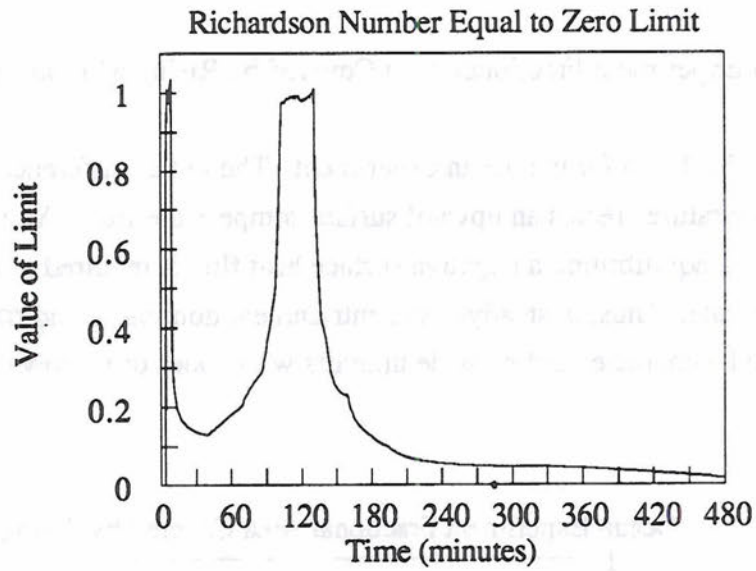
Figure 7.d.2: Ri=0 Limit for Wangara Day 33 0900-1600L.
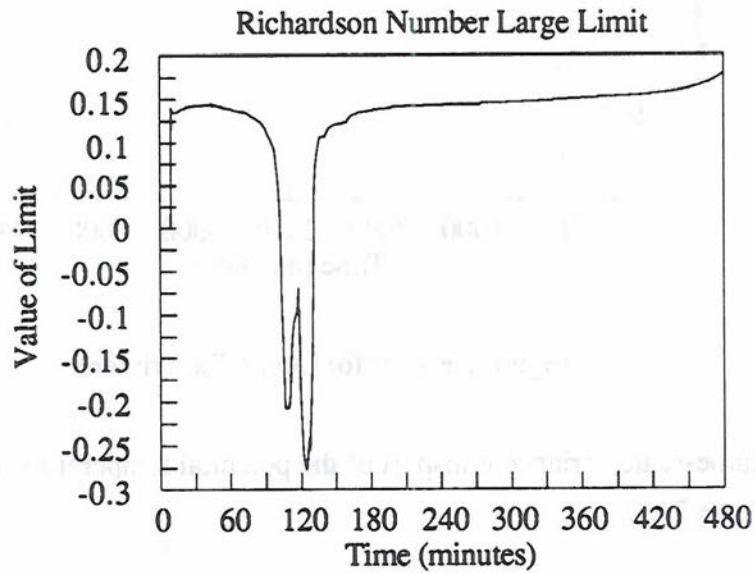
Figure 7.d.3: Ri>>1 Limit for Wangara Day 33 0900-1600L.

As indicated in the figure, the no inversion limit is almost exactly 1 during the rapid growth period. During the late afternoon, the Ri>>1 limit does approach 0.2, but it is a

little too small. This may mean that there is not an exact balance between buoyant production and dissipation of TKE as assumed in the entrainment closure.

7.e. Ocean Experiment Fractional Area Covered by Rising Motion Results

Figure 7.e.1 is σ for the ocean experiment. The initial difference between the SST and air temperature creates an upward surface temperature flux. As a result, σ<1/2 for a short time. In equilibrium, a negative surface heat flux is required to balance a positive entrainment rate. Thus, in steady-state, entrainment dominates and σ>1/2. The boundary layer would be characterized by wide updrafts with zones of narrow downdrafts.

Ocean Experiment Fractional Area Covered by Rising Motion
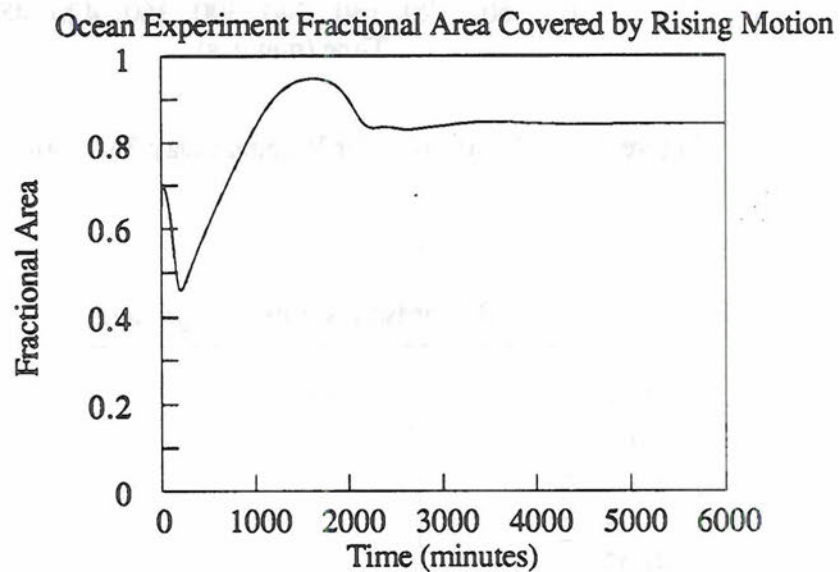
Figure 7.e.1: σ for Ocean Experiment.

The plume-scale variance transport of the potential temperature at levels S and B is shown in figure 7.e.2.

Ocean Experiment Potential Temperature Variance Transports
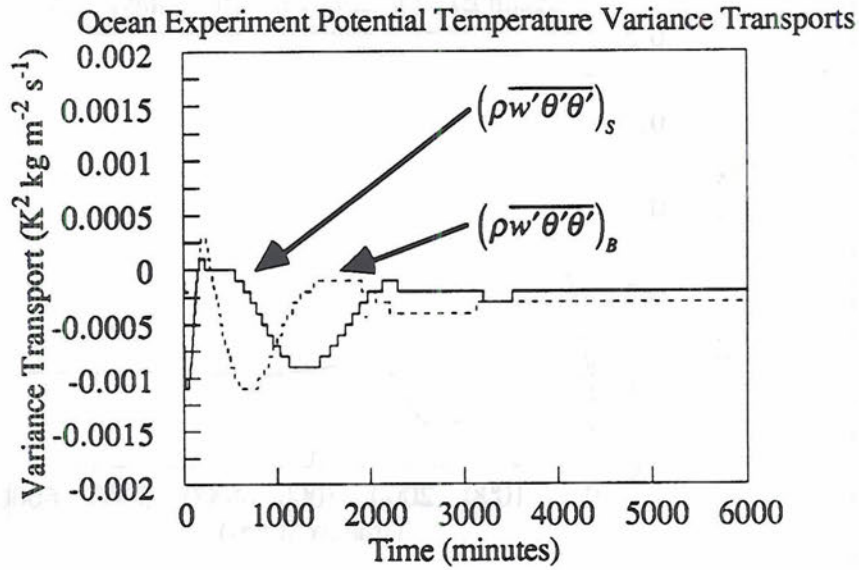
Figure 7.e.2: $\left(\rho\overline{w'\theta'\theta'}\right)_S$ and $\left(\rho\overline{w'\theta'\theta'}\right)_B$ for Ocean Experiment.

When $\sigma<1/2$ both $\left(\rho\overline{w'\theta'\theta'}\right)_S$ and $\left(\rho\overline{w'\theta'\theta'}\right)_B$ are greater than zero. They transition from negative to positive and back to negative when σ becomes less than $1/2$ and then greater than $1/2$. Unlike Wangara, $\left(\rho\overline{w'\theta'\theta'}\right)_S$ never substantially dominates over $\left(\rho\overline{w'\theta'\theta'}\right)_B$. In steady-state, the magnitude of $\left(\rho\overline{w'\theta'\theta'}\right)_B$ is greater than the magnitude of $\left(\rho\overline{w'\theta'\theta'}\right)_S$. Since the transports are negative, the entrainment layer exports variance into the PBL which balances with the dissipation at the surface.

Figure 7.e.3 shows the convective mass flux.
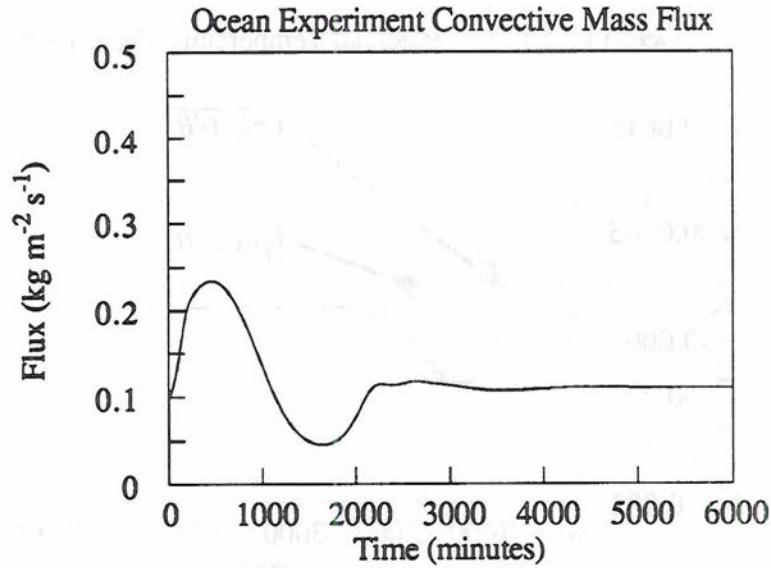
Figure 7.e.3: M_C for Ocean Experiment.

The convective mass flux peaks when $\sigma < 1/2$ and the TKE is large. This marks the short convective period when the PBL grows The minimum of M_C occurs when $\sigma > 1/2$ and the TKE is at its lowest value. Here the surface heat flux is negative and the entrainment rate is at its minimum. For a brief period, the divergence is removing mass faster than it can be replaced by entrainment. There is no convection with the negative heat flux to aid in PBL growth. As a result, the PBL depth levels off and then decreases until the entrainment rate increases sufficiently to balance the divergence At steady-state the TKE and M_C are about twice their minimum values.

For Wangara, M_C was at its minimum value during the most intense convection. The entrainment rate was about 20 times as large as the ventilation mass flux. When $E \gg V$, equation 6.c.7 can be approximated by

$$\sigma = \frac{1}{1 + \dfrac{E}{V}} \approx \frac{V}{E}. \tag{7.e.1}$$

The ratio of V to E, and σ become small when $E \gg V$. This will cause M_C to be small even though vigorous convection is taking place and the PBL is growing rapidly. For the ocean experiment E was only about 1.2 times V during convection. The value of σ was

less than 1/2, but much larger than the minimum from the Wangara simulation. With σ near 1/2 and the TKE large, M_C was at its maximum at the same time as the convection. Caution must be used when comparing the convective mass flux to PBL growth. Growth may occur with a low value if the entrainment rate and ventilation mass flux are large enough to balance subsidence and divergence.

Figures 7.e.4 and 7.e.5 present the updraft and downdraft properties for the potential temperature and mixing ratio at level S.

Ocean Experiment Up/Down Potential Temperatures at Level S
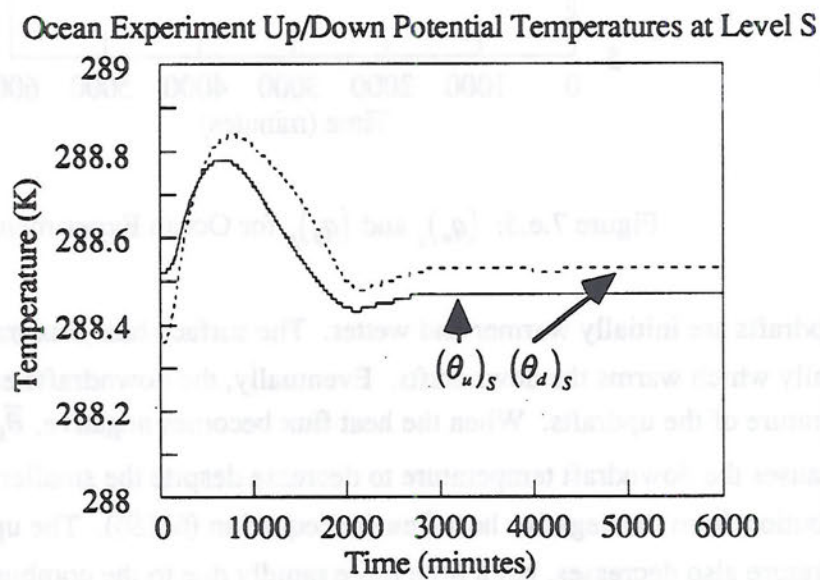
Figure 7.e.4: $(\theta_u)_S$ and $(\theta_d)_S$ for Ocean Experiment.

Ocean Experiment Up/Down Mixing Ratios at Level S
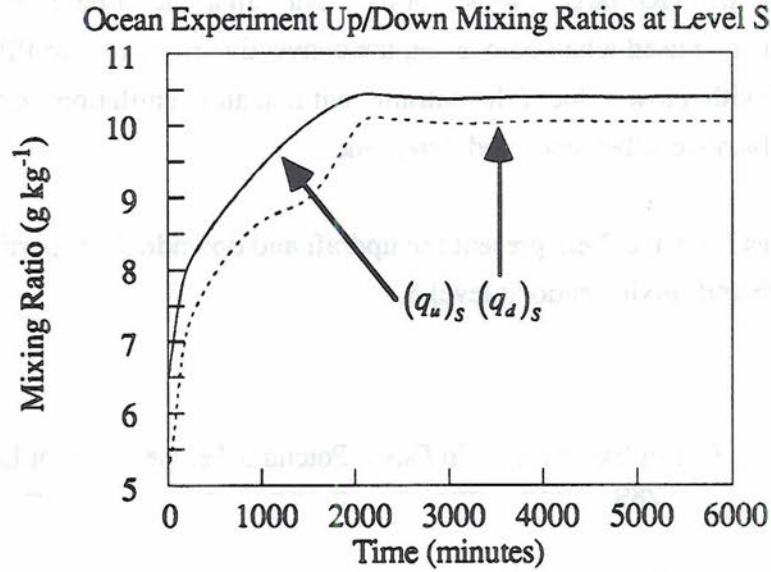
Figure 7.e.5: $(q_u)_s$ and $(q_d)_s$ for Ocean Experiment.

The updrafts are initially warmer and wetter. The surface heat flux transports heat vertically which warms the downdrafts. Eventually, the downdrafts exceed the temperature of the updrafts. When the heat flux becomes negative, $\bar{\theta}_s$ begins to decrease. This causes the downdraft temperature to decrease despite the smaller positive contribution from the negative heat flux (see equation (6.d.9)). The updraft potential temperature also decreases, but a little more rapidly due to the combination of the negative heat flux and decreasing $\bar{\theta}_s$. At equilibrium, $\bar{\theta}_s$, M_C, and $(F_\theta)_s$ are all unchanging, hence $(\theta_u)_s$ and $(\theta_d)_s$ are also unchanging.

Unlike Wangara, the ocean supplies a constant source of moisture. This moisture is readily transported upward in the PBL when convection is strong. This causes the PBL to moisten with time (see Figure 5.b.6). This causes both $(q_u)_s$ and $(q_d)_s$ to increase. As σ increases it begins to have an impact on $(q_d)_s$ which causes $(q_d)_s$ to increase more slowly until σ decreases again. Just as for the potential temperature, the variables that the updraft and downdraft mixing ratio depend on are unchanging at equilibrium, thus $(q_u)_s$ and $(q_d)_s$ do not change either.

The updraft and downdraft properties at level B are shown in Figures 7.e.6 and 7.e.7.

100

Ocean Experiment Up/Down Potential Temperatures at Level B
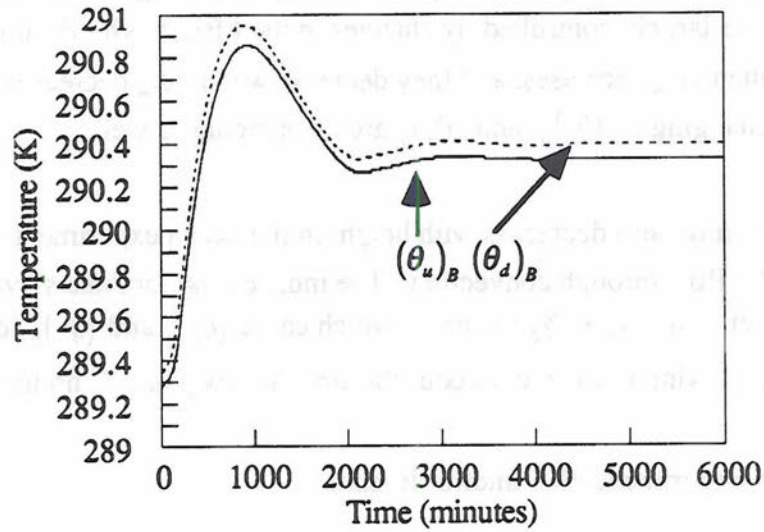
Figure 7.e.6: $(\theta_u)_B$ and $(\theta_d)_B$ for Ocean Experiment.

Ocean Experiment Up/Down Mixing Ratios at Level B
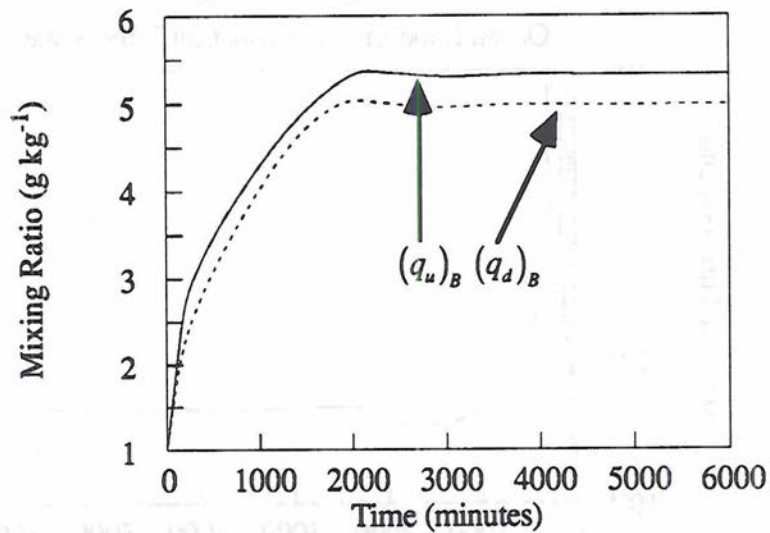
Figure 7.e.7: $(q_u)_B$ and $(q_d)_B$ for Ocean Experiment.

The potential temperature increases with height in the ocean experiment. The updraft and downdraft potential temperature at level B depend on changes in $\overline{\theta}_B$ assuming the flux contribution is small compared to these changes. The PBL depth increases rapidly during

101

the early portion of the simulation. This causes relatively large changes in $\bar{\theta}_B$ compared to the flux contribution. Also, the flux contribution is small initially because it contains M_C in the denominator which is large for about the first 1000 minutes. Therefore, the properties are largely controlled by changes in the PBL depth. Both $(\theta_u)_B$ and $(\theta_d)_B$ increase when Δp_m increases, and they decrease when Δp_m decreases. At equilibrium, Δp_m is unchanging so $(\theta_u)_B$ and $(\theta_d)_B$ are unchanging as well.

The mixing ratio decreases with height in the ocean experiment, but the ocean moistens the PBL through convection. The moistening dominates over drying that occurs due to ascent. Therefore, $\bar{q}_B$ increases which cause $(q_u)_B$ and $(q_d)_B$ to increase until the mixed layer mixing ratio reaches equilibrium. At this point $\bar{q}_B$ no longer changes.

7.f. Ocean Experiment PBL Interior Results

The ocean experiment interior results were done in the same manner as Wangara using a $\hat{\tau}$ of 1 second. These results are also $\hat{\tau}$ times their values at $\hat{\tau} = 1$ second for other settings of $\hat{\tau}$. The dissipation time scale is shown in Figure 7.f.1.
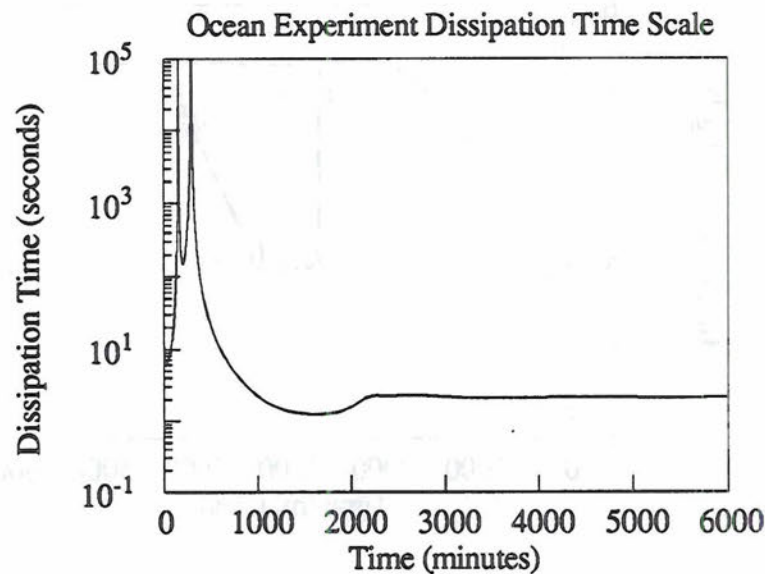
Figure 7.f.1: τ_{dis} for Ocean Experiment.

102

The two peaks correspond to $\sigma = 1/2$ ($\tau_{dis} \to \infty$). For Wangara the minimum in τ_{dis} occurred when $\sigma \ll 1$. In this case the minimum occurs for $\sigma \approx 0.95$. During the convective period τ_{dis} is about 2 orders of magnitude longer (not considering the peaks) than for Wangara. This would indicate that dissipation was more effective for the Wangara simulation due to the intense convection.

The next set of figures contain the dissipation rates for θ and q at levels S and B.

Ocean Experiment Potential Temperature Dissipation Rates
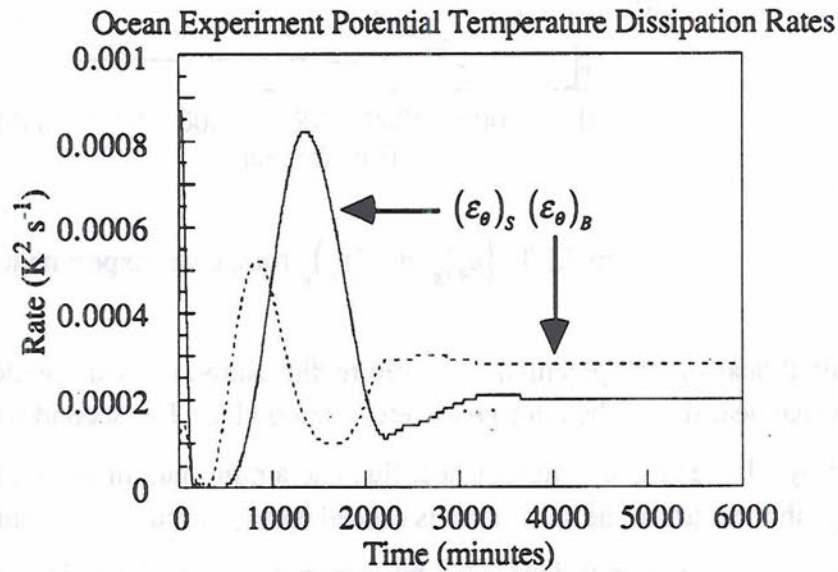
Figure 7.f.2: $\left(\varepsilon_\theta\right)_S$ and $\left(\varepsilon_\theta\right)_B$ for Ocean Experiment.

Ocean Experiment Mixing Ratio Dissipation Rates
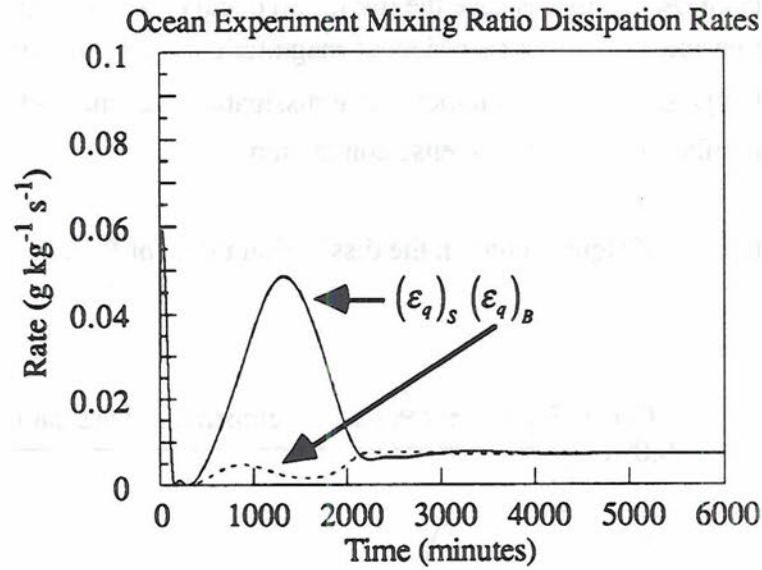
Figure 7.f.3: $\left(\varepsilon_q\right)_S$ and $\left(\varepsilon_q\right)_B$ for Ocean Experiment.

The initial peaks in the potential temperature dissipation rates are predominantly due to the surface heat flux. The rates go to zero when $\sigma=1/2$. The second peak in $\left(\varepsilon_\theta\right)_S$ is caused by a large negative surface heat flux and a minimum in the TKE. The minimum in $\left(\varepsilon_\theta\right)_B$ that occurs at the same time is caused by a minimum in the entrainment rate. At equilibrium, dissipation is dominated by entrainment. The inversion maintains a temperature gradient at the top of the PBL which creates a downward flux. The small negative heat flux at the surface results in a smaller value of $\left(\varepsilon_q\right)_S$.

The large initial surface moisture flux creates the first peak in $\left(\varepsilon_q\right)_S$. The second peak is due to a minimum in the TKE and a relatively large surface flux. The minimum in $\left(\varepsilon_q\right)_B$ at the same time is caused by a minimum in E. In equilibrium, the dissipation rates are equal because the surface and PBL top moisture fluxes are equal. The moisture gradient at the PBL top is greater than at the surface, but V>E.

The last diagnostics for the ocean experiment are the potential temperature and mixing ratio gradients. Figure 7.f.4 shows the potential gradients for $\hat{\tau}$ equal to 10, 100, and 1000 seconds. Like Wangara, the 1 second gradients were too large and are not

shown. The mixing ratio gradients for 100 and 1000 seconds are in Figure 7.f.5. The 10 second gradient was also too large.

Ocean Experiment Potential Temperature Gradient
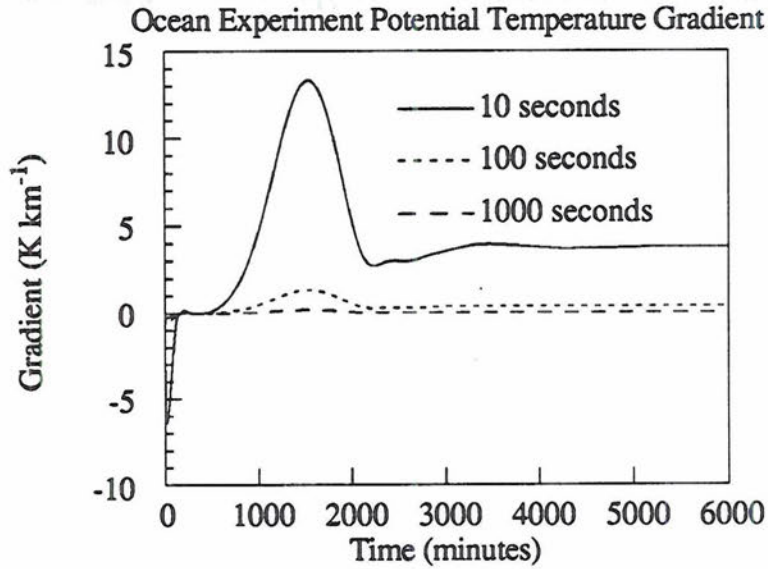
Figure 7.f.4: $\frac{\partial \theta}{\partial z}$ with $\hat{\tau} = 10, 100,$ and 1000 Seconds for Ocean Experiment.

Ocean Experiment Mixing Ratio Gradient
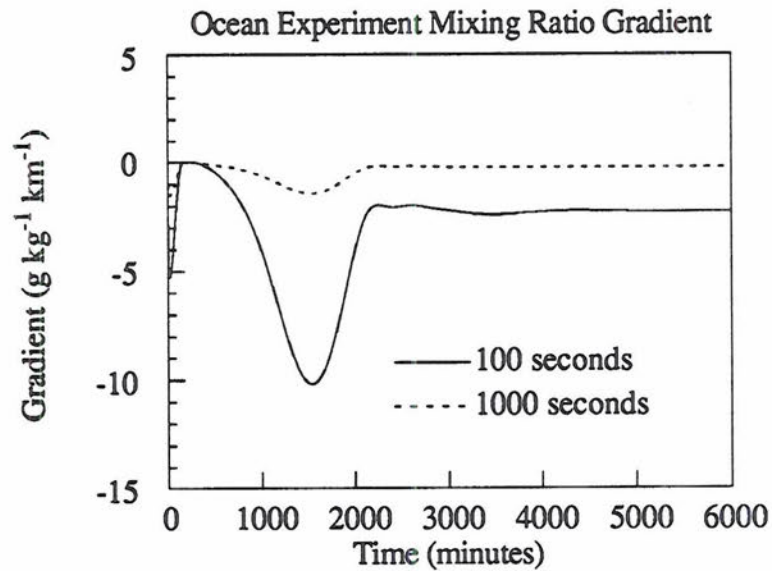
Figure 7.f.5: $\frac{\partial q}{\partial z}$ with $\hat{\tau} = 10, 100,$ and 1000 Seconds for Ocean Experiment.

All the gradients show the potential temperature increasing with height and the mixing ratio decreasing with height, except at the very beginning of the simulation. The 10 second gradients appear to be too large as was found for Wangara. A $\hat{\tau}$ between 100 and 1000 seconds seems most suitable for this type of simulation as well.

8. Description of Two-Layer Model

The two-layer model uses the same set of equations and the same parameterizations as the one-layer model except for the mixed layer potential temperature and mixing ratio equations. Infinitesimal ventilation (surface) and entrainment layers are maintained with the top of the ventilation layer still at level S and the bottom of the entrainment layer still at level B. The mixed layer, however, is divided into 2 layers. Level 1 is within the top layer and level 2 is in the bottom layer. The layers are divided at level I (interior). Figure 8.1 is a diagram of the two-layer model.
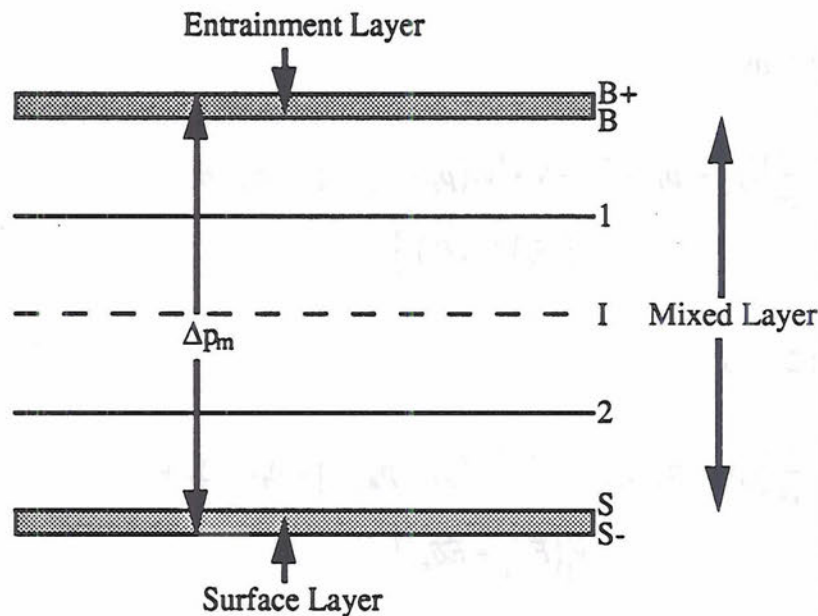
Figure 8.1: Illustration of 2-Layer Model.

Level 2 was set 1/4 of the way up in the mixed layer, level I in the center, and level 1 3/4 of the way up. The levels are evenly spaced for mathematical ease. The equations used to predict the mean potential temperature and mixing ratio at levels 1 and 2 do not require the levels to be equally spaced. These equations are developed in the next section. Once the mean potential temperature and mixing ratio are initialized or predicted at levels 1 and 2, the mixed layer values are determined using

$$\theta_m = \frac{\overline{\theta}_1 + \overline{\theta}_2}{2} \tag{8.1}$$

and

$$q_m = \frac{\overline{q}_1 + \overline{q}_2}{2}. \tag{8.2}$$

8.a. Two-Layer Potential Temperature and Mixing Ratio Equations

From Randall (personal communication, 1993), the two-layer equations for the potential temperature and mixing ratio are

$$\frac{\partial}{\partial t}\left[(p_I - p_B)\overline{\theta}_1\right] = -\nabla \bullet \left[v_1(p_I - p_B)\overline{\theta}_1\right] + \Delta p_m \dot{\overline{\xi}}_I \overline{\theta}_I + \\ g\left[(F_\theta)_I + E\overline{\theta}_{B+}\right] \tag{8.a.1}$$

at level 1 and

$$\frac{\partial}{\partial t}\left[(p_S - p_I)\overline{\theta}_2\right] = -\nabla \bullet \left[v_2(p_S - p_I)\overline{\theta}_1\right] - \Delta p_m \dot{\overline{\xi}}_I \overline{\theta}_I + \\ g\left[(F_\theta)_S - (F_\theta)_I\right] \tag{8.a.2}$$

at level 2, and

$$\frac{\partial}{\partial t}\left[(p_I - p_B)\overline{q}_1\right] = -\nabla \bullet \left[v_1(p_I - p_B)\overline{q}_1\right] + \Delta p_m \dot{\overline{\xi}}_I \overline{q}_I + \\ g\left[(F_q)_I + E\overline{q}_{B+}\right] \tag{8.a.3}$$

at level 1 and

$$\frac{\partial}{\partial t}\left[(p_S - p_I)\overline{q}_2\right] = -\nabla \bullet \left[v_2(p_S - p_I)\overline{q}_1\right] - \Delta p_m \dot{\overline{\xi}}_I \overline{q}_I + \\ g\left[(F_q)_S - (F_q)_I\right] \tag{8.a.4}$$

at level 2. In these equations, $\dot{\overline{\xi}}_L$ is the vertical velocity at level I as seen following the ξ-coordinate where $\xi_I = \dfrac{p_S - p_I}{\Delta p_m}$.

The ξ coordinate is similar to the modified σ-coordinate used by Suarez et al. (1983). The coordinate system is designed so that the earth's surface and PBL top are coordinate surfaces. At the earth's surface, $\xi \equiv 0$, and at the PBL top, $\xi \equiv 1$. For $p_S \le p \le p_B$, $\xi = \dfrac{p_S - p}{\Delta p_m}$. The vertical velocity, $\dot{\xi}$, measures how fast a ξ surface moves as the PBL depth changes, and can be given by $\dot{\xi}_{final\ pressure} = \dfrac{(\xi)_{final\ pressure} - (\xi)_{initial\ pressure}}{\Delta t}$. At the earth's surface, ξ is always 0 no matter how much the PBL depth changes, so $\dot{\xi}_S$ is 0 here. At the PBL top, ξ is always 1, and $\dot{\xi}_B$ depends on how much the PBL depth has changed.

A more useful formula for $\dot{\xi}_I$ is obtained by adding the mass conservation equations for layers 1 and 2, $\dfrac{\partial}{\partial t}(p_I - p_B) = -\nabla \bullet [v_I(p_I - p_B)] + \Delta p_m \dot{\xi}_I + gE$ and $\dfrac{\partial}{\partial t}(p_S - p_I) = -\nabla \bullet [v_2(p_S - p_I)] - \Delta p_m \dot{\xi}_I$, together to get

$$\frac{\partial}{\partial t}\Delta p_m + \nabla \bullet (v_m \Delta p_m) - gE = 0, \tag{8.a.5}$$

and then using the conservation of mass for layer 2, (8.a.5), and $\xi_I = \dfrac{p_S - p_I}{\Delta p_m}$ to obtain

$$\Delta p_m \dot{\xi}_I = \xi_I \nabla \bullet [(v_m - v_2)\Delta p_m] - \xi_I gE. \tag{8.a.6}$$

The vertical velocity is simply $\dot{\xi}_I = \dfrac{\xi_I}{\Delta p_m}\nabla \bullet [(v_m - v_2)\Delta p_m] - \dfrac{\xi_I gE}{\Delta p_m}$.

Equations (8.a.1)-(8.a.4) can be written in advective form by using the conservation of mass equations for the two layers. Then, assuming horizontal homogeneity, except for the mean divergence, gives

$$(p_I - p_B)\frac{\partial \overline{\theta}_I}{\partial t} = \Delta p_m \dot{\xi}_I(\overline{\theta}_I - \overline{\theta}_I) + g[(F_\theta)_I + E(\overline{\theta}_{B+} - \overline{\theta}_I)], \tag{8.a.7}$$

$$(p_S - p_I)\frac{\partial \overline{\theta}_2}{\partial t} = \Delta p_m \dot{\overline{\xi}}_I(\overline{\theta}_I - \overline{\theta}_2) + g\left[(F_\theta)_S - (F_\theta)_I\right],$$ (8.a.8)

$$(p_I - p_B)\frac{\partial \overline{q}_I}{\partial t} = \Delta p_m \dot{\overline{\xi}}_I(\overline{q}_I - \overline{q}_I) + g\left[(F_q)_I + E(\overline{q}_{B+} - \overline{q}_I)\right],$$ (8.a.9)

$$(p_S - p_I)\frac{\partial \overline{q}_2}{\partial t} = \Delta p_m \dot{\overline{\xi}}_I(\overline{q}_I - \overline{q}_2) + g\left[(F_q)_S - (F_q)_I\right],$$ (8.a.10)

and $$\dot{\overline{\xi}}_I = \frac{-gE\xi_I}{\Delta p_m}.$$ (8.a.11)

Equations (8.a.7)-(8.a.10) can be solved if the flux of the potential temperature and mixing ratio at level I are known. The equations for this flux are developed in the next section. The mean value of θ and q at level I is just the mixed layer value of these variables ($\theta_m = \overline{\theta}_I$, $q_m = \overline{q}_I$). Equations (8.a.7)-(8.a.10) can then be rewritten in terms of $\overline{\theta}_I$, $\overline{q}_I$, $\overline{\theta}_2$, and $\overline{q}_2$ using (8.1), (8.2), and the interpolation relations for $\overline{\theta}_{S \, and \, B}$ and $\overline{q}_{S \, and \, B}$.

The mean potential temperature increases linearly with height, and the mean mixing ratio decreases linearly with height. The mean value of these variables at any pressure is given by

$$\overline{\theta}(p) = a + bp$$ (8.a.12)

and

$$\overline{q}(p) = c + dp$$ (8.a.13)

Equations (8.a.12) and (8.a.13) are just equations for lines where a and c are intercepts, and b and d are slopes of the lines. The slopes are given by the difference of the mean values at levels 1 and 2 divided by the difference in pressure between levels 1 and 2. The intercepts are then

$$\overline{\theta}(p = I) = \theta_m = a + \frac{\overline{\theta}_I - \overline{\theta}_2}{p_I - p_2}p_I$$

or

$$a = \theta_m - \frac{\overline{\theta}_I - \overline{\theta}_2}{p_I - p_2}p_I,$$ (8.a.14)

and

$$\bar{q}(p=I)=q_m=c+\frac{\bar{q}_1-\bar{q}_2}{p_1-p_2}p_1$$

or

$$c=q_m-\frac{\bar{q}_1-\bar{q}_2}{p_1-p_2}p_1. \qquad (8.a.15)$$

Inserting (8.a.14) into (8.a.12) and (8.a.15) into (8.a.13) gives the mean quantities at any pressure,

$$\bar{\theta}(p)=\theta_m+(p-p_1)\frac{\bar{\theta}_1-\bar{\theta}_2}{p_1-p_2} \qquad (8.a.16)$$

and

$$\bar{q}(p)=q_m+(p-p_1)\frac{\bar{q}_1-\bar{q}_2}{p_1-p_2}. \qquad (8.a.17)$$

The interpolation relations for θ and q at levels S and B are obtained by using $p=p_S$ and $p=p_B$ in (8.a.16) and (8.a.17).

Then, the finite difference forms of (8.a.7)-(8.a.10) for Wangara using a backward (implicit) scheme are

$$\bar{\theta}_1^{n+1}-\frac{gE\Delta t}{\Delta p_m}\left(\frac{p_S-p_1}{p_1-p_B}\right)\bar{\theta}_1^{n+1}+\frac{gE\Delta t}{\Delta p_m}\left(\frac{p_S-p_1}{p_1-p_2}\right)\bar{\theta}_1^{n+1}-$$

$$\frac{(p_S-p_1)\sigma(1-\sigma)\Delta t}{2\hat{\tau}(p_1-p_2)}\bar{\theta}_1^{n+1}+\frac{gE\Delta t}{(p_1-p_B)}\bar{\theta}_1^{n+1}-\frac{gE\Delta t}{\Delta p_m}\left(\frac{p_S-p_1}{p_1-p_2}\right)\bar{\theta}_2^{n+1}+$$

$$\frac{(p_S-p_1)\sigma(1-\sigma)\Delta t}{2\hat{\tau}(p_1-p_2)}\bar{\theta}_2^{n+1}=-\frac{gE\Delta t}{\Delta p_m}\left(\frac{p_S-p_1}{p_1-p_B}\right)\bar{\theta}_{B+}+\frac{g\Delta t}{\Delta p_m}(F_\theta)_S \qquad (8.a.18)$$

$$+\frac{gE\Delta t}{(p_1-p_B)}\bar{\theta}_{B+}+\bar{\theta}_1^n,$$

$$\frac{gE\Delta t}{\Delta p_m}\overline{\theta}_1^{n+1} - \frac{gE\Delta t}{\Delta p_m}\left(\frac{p_l - p_B}{p_l - p_2}\right)\overline{\theta}_1^{n+1} + \frac{(p_l - p_B)\sigma(1-\sigma)\Delta t}{2\hat{\tau}(p_l - p_2)}\overline{\theta}_1^{n+1} +$$

$$\frac{gE\Delta t}{(p_l - p_B)}\overline{\theta}_1^{n+1} + \overline{\theta}_2^{n+1} + \frac{gE\Delta t}{\Delta p_m}\left(\frac{p_l - p_B}{p_l - p_2}\right)\overline{\theta}_2^{n+1} -$$

$$\frac{(p_l - p_B)\sigma(1-\sigma)\Delta t}{2\hat{\tau}(p_l - p_2)}\overline{\theta}_2^{n+1} = \frac{g\Delta t}{(p_S - p_l)}(F_\theta)_S + \frac{gE\Delta t}{\Delta p_m}\overline{\theta}_{B+} - \qquad (8.a.19)$$

$$\frac{g\Delta t}{\Delta p_m}\left(\frac{p_l - p_B}{p_S - p_l}\right)(F_\theta)_S + \overline{\theta}_2^n,$$

$$\overline{q}_1^{n+1} - \frac{gE\Delta t}{\Delta p_m}\left(\frac{p_S - p_l}{p_l - p_B}\right)\overline{q}_1^{n+1} + \frac{gE\Delta t}{\Delta p_m}\left(\frac{p_S - p_l}{p_l - p_2}\right)\overline{q}_1^{n+1} -$$

$$\frac{(p_S - p_l)\sigma(1-\sigma)\Delta t}{2\hat{\tau}(p_l - p_2)}\overline{q}_1^{n+1} + \frac{gE\Delta t}{(p_l - p_B)}\overline{q}_1^{n+1} + \frac{gV\Delta t}{2\Delta p_m}\overline{q}_1^{n+1} +$$

$$\frac{gV\Delta t}{\Delta p_m}\left(\frac{p_S - p_l}{p_l - p_2}\right)\overline{q}_1^{n+1} - \frac{gE\Delta t}{\Delta p_m}\left(\frac{p_S - p_l}{p_l - p_2}\right)\overline{q}_2^{n+1} + \frac{(p_S - p_l)\sigma(1-\sigma)\Delta t}{2\hat{\tau}(p_l - p_2)}\overline{q}_2^{n+1} +$$

$$+\frac{gV\Delta t}{2\Delta p_m}\overline{q}_2^{n+1} - \frac{gV\Delta t}{\Delta p_m}\left(\frac{p_S - p_l}{p_l - p_2}\right)\overline{q}_2^{n+1} = -\frac{gE\Delta t}{\Delta p_m}\left(\frac{p_S - p_l}{p_l - p_B}\right)\overline{q}_{B+} + \frac{gV\Delta t}{\Delta p_m}\overline{q}_{S-} + \qquad (8.a.20)$$

$$\frac{gE\Delta t}{(p_l - p_B)}\overline{q}_{B+} + \overline{q}_1^n,$$

and

$$\frac{gE\Delta t}{\Delta p_m}\overline{q}_1^{n+1} - \frac{gE\Delta t}{\Delta p_m}\left(\frac{p_l - p_B}{p_l - p_2}\right)\overline{q}_1^{n+1} + \frac{(p_l - p_B)\sigma(1-\sigma)\Delta t}{2\hat{\tau}(p_l - p_2)}\overline{q}_1^{n+1} +$$

$$\frac{gV\Delta t}{2(p_S - p_l)}\overline{q}_1^{n+1} + \frac{gV\Delta t}{(p_l - p_2)}\overline{q}_1^{n+1} - \frac{gV\Delta t}{2\Delta p_m}\left(\frac{p_l - p_B}{p_S - p_l}\right)\overline{q}_1^{n+1} -$$

$$\frac{gV\Delta t}{\Delta p_m}\left(\frac{p_l - p_B}{p_l - p_2}\right)\overline{q}_1^{n+1} + \overline{q}_2^{n+1} + \frac{gE\Delta t}{\Delta p_m}\left(\frac{p_l - p_B}{p_l - p_2}\right)\overline{q}_2^{n+1} -$$

$$\frac{(p_l - p_B)\sigma(1-\sigma)\Delta t}{2\hat{\tau}(p_l - p_2)}\overline{q}_2^{n+1} + \frac{gV\Delta t}{2(p_S - p_l)}\overline{q}_2^{n+1} - \frac{gV\Delta t}{(p_l - p_2)}\overline{q}_2^{n+1} -$$

$$\frac{gV\Delta t}{2\Delta p_m}\left(\frac{p_l - p_B}{p_S - p_l}\right)\overline{q}_2^{n+1} + \frac{gV\Delta t}{\Delta p_m}\left(\frac{p_l - p_B}{p_l - p_2}\right)\overline{q}_2^{n+1} = \frac{gV\Delta t}{(p_S - p_l)}\overline{q}_{S-} + \qquad (8.a.21)$$

$$\frac{gE\Delta t}{\Delta p_m}\overline{q}_{B+} - \frac{gV\Delta t}{\Delta p_m}\left(\frac{p_l - p_B}{p_S - p_l}\right)\overline{q}_{S-} + \overline{q}_2^n.$$

112

The surface heat flux appears explicitly in (8.a.18) and (8.a.19) because it was prescribed for the Wangara simulations. For the ocean simulations (8.a.20) and (8.a.21) were used with $\bar{\theta}$ in place of $\bar{q}$, instead of (8.a.18) and (8.a.19), for the potential temperatures at levels 1 and 2.

Equations (8.a.18) and (8.a.19) are two equations in two unknowns, $\bar{\theta}_1$ and $\bar{\theta}_2$. Equations (8.a.20) and (8.a.21) are also two equations in two unknowns, $\bar{q}_1$ and $\bar{q}_2$. These sets of equations are solved simultaneously to obtain the mean values at levels 1 and 2. The mixed layer values are finally determined using (8.1) and (8.2).

8.b. Two-Layer Model Diagnostics

Since the two-layer model predicts the mean values of θ and q at levels 1 and 2, the gradients of these variables were determined by using

$$\frac{\partial \bar{\theta}}{\partial z} = \frac{\bar{\theta}_1 - \bar{\theta}_2}{z_1 - z_2} \qquad (8.b.1)$$

and

$$\frac{\partial \bar{q}}{\partial z} = \frac{\bar{q}_1 - \bar{q}_2}{z_1 - z_2}, \qquad (8.b.2)$$

instead of equation (6.d.9).

The final form for the flux is obtained by truncating ((6.d.11) at first order in $\Delta p_m / \delta p_*$ and substituting this into (6.d.10) at level I. This gives

$$\left(F_\psi\right)_I \approx \left(F_\psi\right)_B \left(\frac{p_S - p_I}{\Delta p_m}\right) + \left(F_\psi\right)_S \left(\frac{p_I - p_B}{\Delta p_m}\right) +$$
$$\frac{1}{2} \frac{(p_I - p_B)(p_S - p_I)\sigma(1 - \sigma)}{g\hat{\tau}} \frac{\partial \bar{\psi}}{\partial p}. \qquad (8.b.3)$$

The gradient in (8.b.3) is determined using (8.b.1) or (8.b.2) and the hydrostatic relation.

9. Two-Layer Model Results

Prognostic results for the two-layer model using the Wangara data are presented and compared with the prognostic results from the one-layer model. Diagnostic results for the gradients, and the mean values of θ and q at levels S, 2, I, 1, and B are also shown. The diagnostic results were obtained using a $\hat{\tau}$ of 1, 10, 100, and 1000 seconds.

9.a. Two-Layer Prognostic Results

Figures 9.a.1-9.a.5 show the prognostic variables using the two-layer model.

Figure 9.a.1: Two-Layer Δz_m.

Two-Layer Potential Temperature
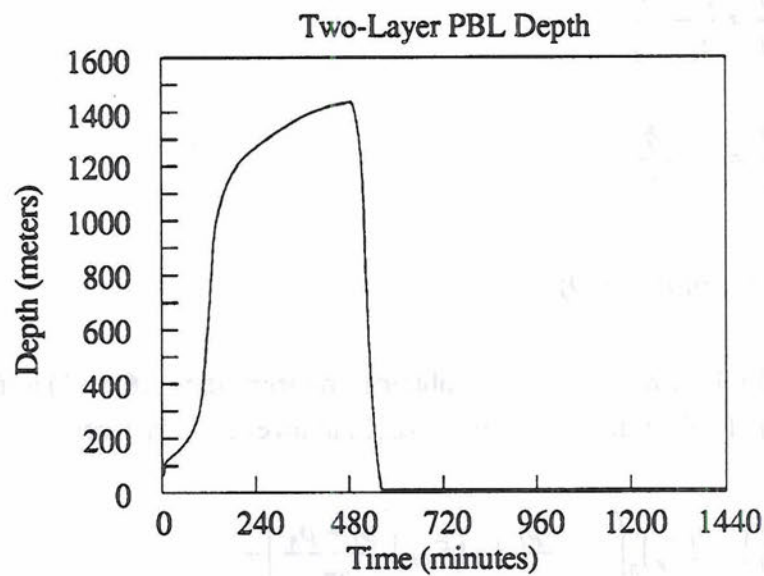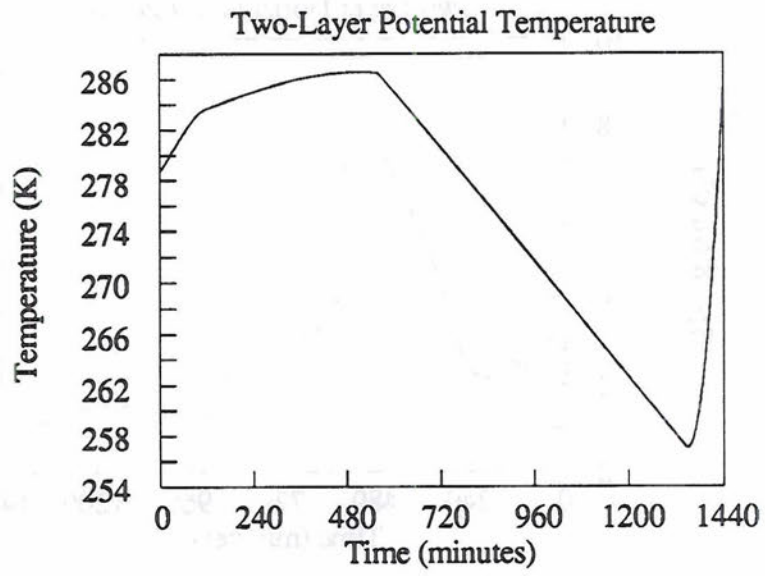
Figure 9.a.2: Two-Layer θ_m.

Two-Layer Mixing Ratio
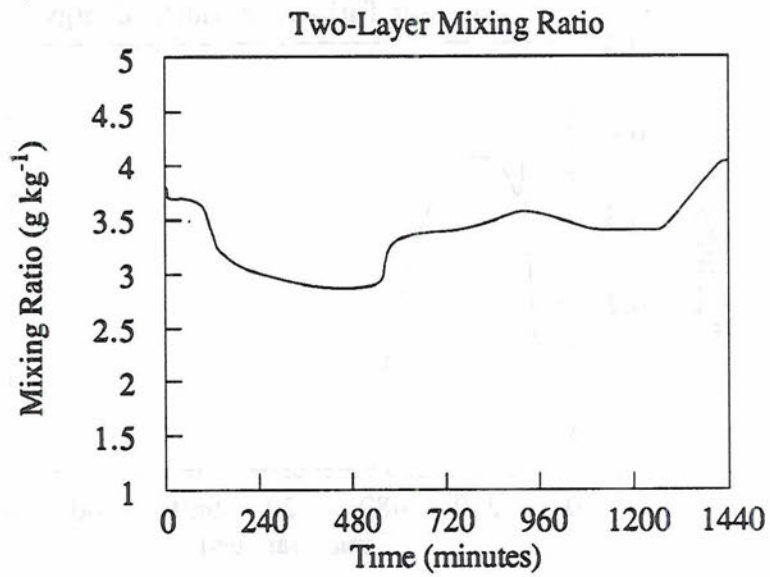
Figure 9.a.3: Two-Layer q_m.
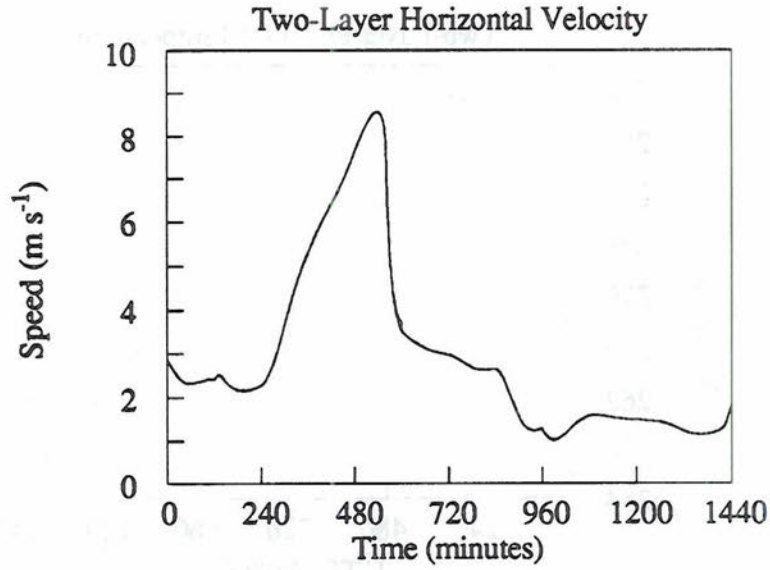
Figure 9.a.4: Two-Layer $|v_m|$.
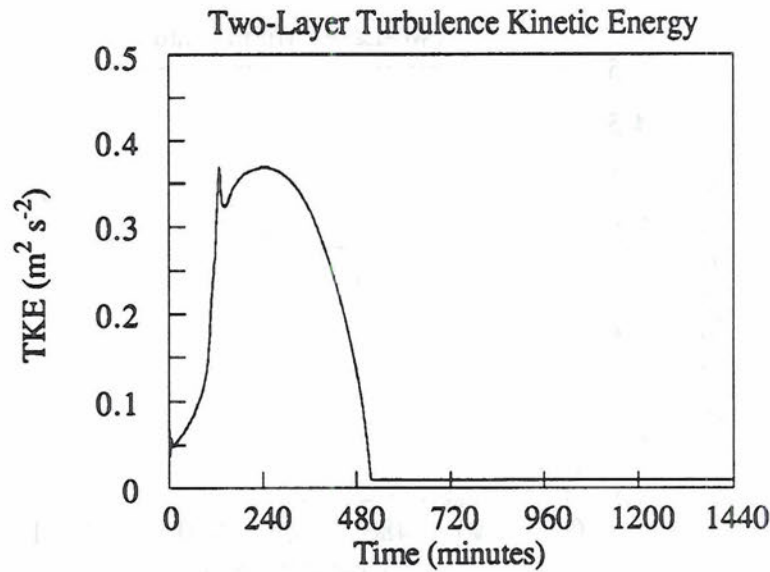
Figure 9.a.5: Two-Layer e_m.

This is no difference between these figures and the figures for the one-layer prognostic variables. This was expected for Δz_m, $|v_m|$, and e_m which are predicted the same way in each model. Identical values for θ_m and q_m indicate that the two-layer model is

116

functioning properly. Prognostic variables for the two-layer ocean experiment are not shown, but they were also the same as the one-layer ocean experiment variables.

9.b. Two-Layer Diagnostic Results

To show the effects of varying $\hat{\tau}$, the initial values of the mean θ and q were set to

$$\left(\overline{\theta}_1\right)_{initial} = \left(\theta_m\right)_{initial} + 3\ K,$$

$$\left(\overline{\theta}_2\right)_{initial} = \left(\theta_m\right)_{initial} - 3\ K,$$

$$\left(\overline{q}_1\right)_{initial} = \left(q_m\right)_{initial} - 1\ g\ kg^{-1},$$

and

$$\left(\overline{q}_2\right)_{initial} = \left(q_m\right)_{initial} + 1\ g\ kg^{-1}. \tag{9.b.1}$$

This gave a sounding where the potential temperature was initially increasing with height and the mixing ratio was initially decreasing with height. The gradients of $\overline{\theta}$ and $\overline{q}$ were then determined with these initial conditions and are shown in Figures 9.b.1 and 9.b.2.
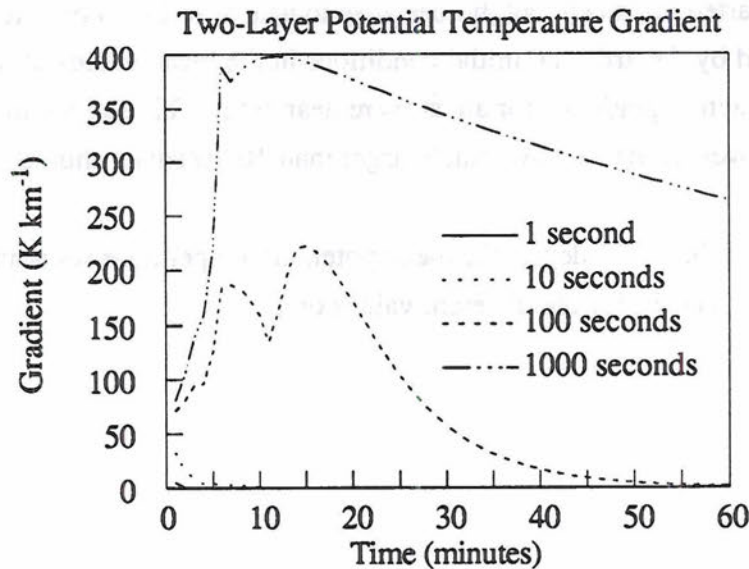
Figure 9.b.1: $\dfrac{\partial\overline{\theta}}{\partial z}$ with $\hat{\tau}$ = 1, 10, 100, and 1000 Seconds for Two-Layer Model.

117
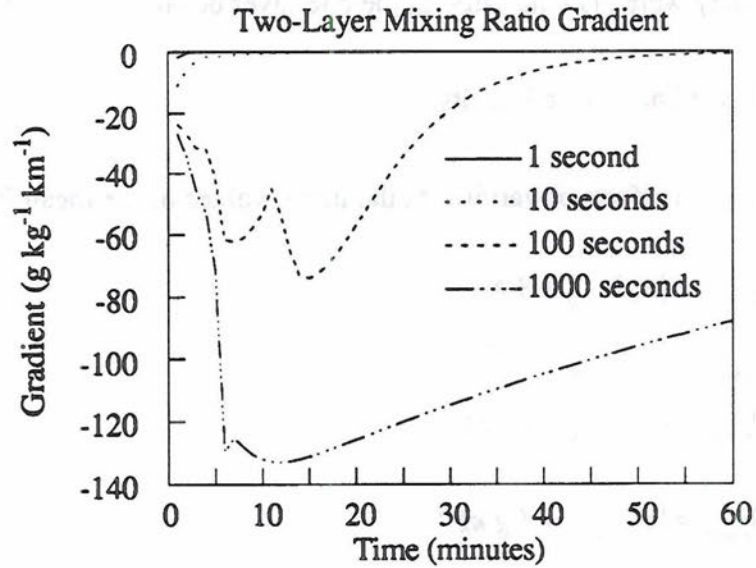
Figure 9.b.2: $\dfrac{\partial \overline{q}}{\partial z}$ with $\hat{\tau} = 1, 10, 100,$ and 1000 Seconds for Two-Layer Model.

The gradients for $\hat{\tau}$ of 1 and 10 seconds were very small all the time. The 1000 second gradients are the only ones that were not near zero within 60 minutes. The 100 second gradients started out steep, but did decrease to near zero by 60 minutes. These gradients were created by the artificial initial conditions in the mean values of θ and q at levels 1 and 2. The actual gradients for all $\hat{\tau}$s were near zero. This and the one-layer gradients do indicate, however, that a $\hat{\tau}$ not much larger than 100 seconds should be used.

Figures 9.b.3-9.b.6 depict the mean potential temperature soundings using $\overline{\theta}$ at levels S, 2, 1, and B, for the different values of $\hat{\tau}$.

118

Two-Layer Mean Potential Temperatures For 1 Second
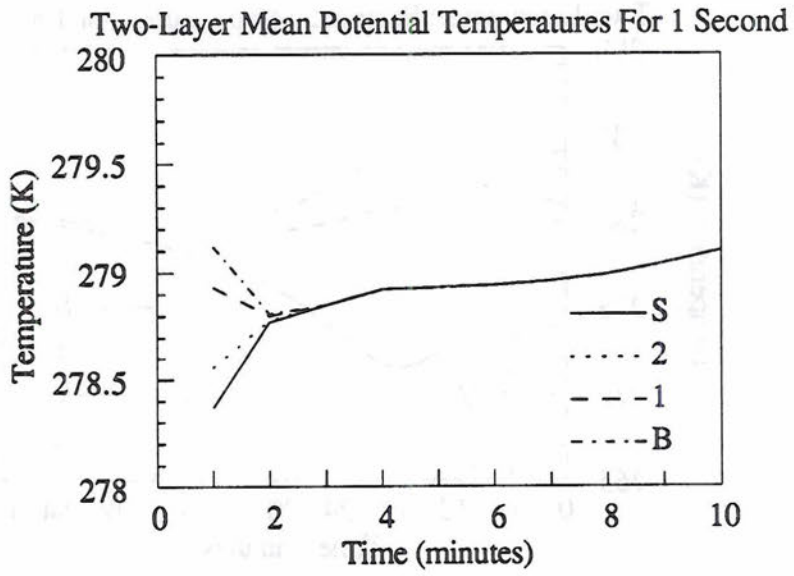
Figure 9.b.3: Mean Potential Temperatures Using $\hat{\tau} = 1$ Second.

Two-Layer Mean Potential Temperatures For 10 Seconds
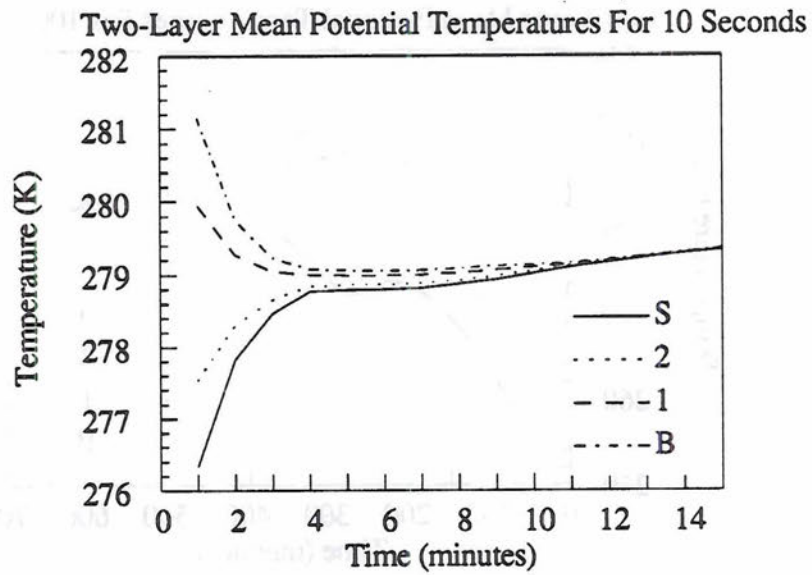
Figure 9.b.4: Mean Potential Temperatures Using $\hat{\tau} = 10$ Seconds.
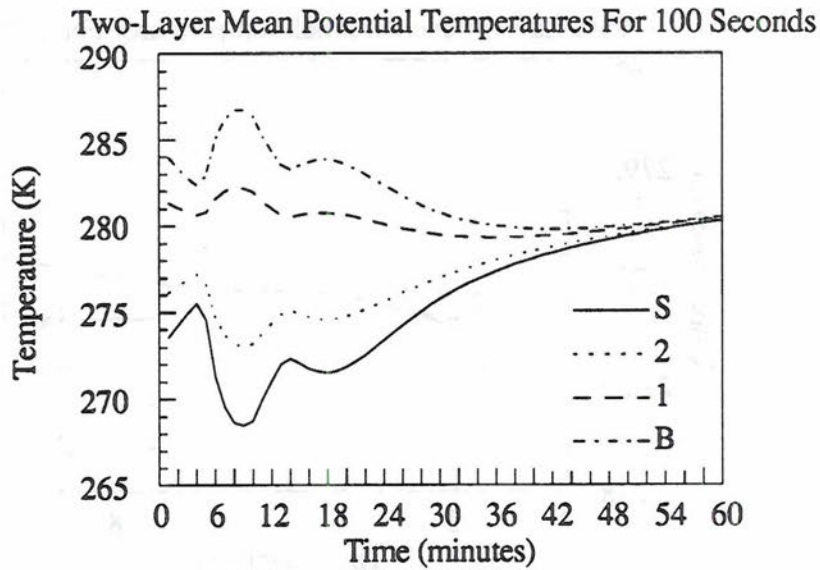
Figure 9.b.5: Mean Potential Temperatures Using $\hat{\tau} = 100$ Seconds.
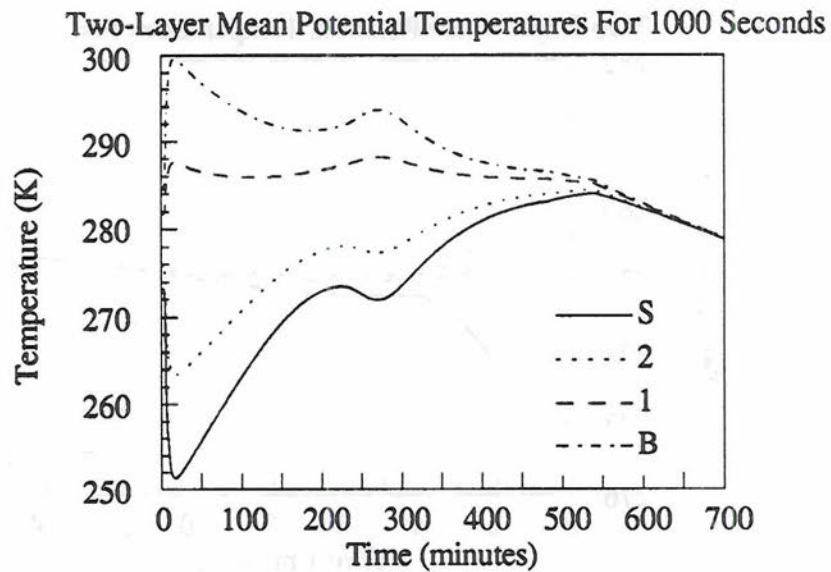
Figure 9.b.6: Mean Potential Temperatures Using $\hat{\tau} = 1000$ Seconds.

These figures indicate how long it took for the mean potential temperatures to adjust to the mixed layer potential temperature. For $\hat{\tau} = 1$ second, it only took 3 minutes for adjustment. When $\hat{\tau}$ was set to 10 seconds, the adjustment time increased to about 15

minutes. At a $\hat{\tau}$ of 100 seconds, the time to adjust had jumped to a little over an hour. Also, the temperatures diverged for short periods twice. Finally, when $\hat{\tau}$ was set to 1000 seconds, the temperatures did not adjust until t=700 minutes (12 hours). There was considerable divergence in the temperatures initially, and a small amount of divergence from about t=240 to 300 minutes.

10. Summary and Conclusions

A single-layer bulk boundary layer model was presented that predicts the mixed layer values of the potential temperature, mixing ratio, and u and v momentum. The model also predicts the depth of the boundary layer in terms of pressure (Δp_m) and the turbulence kinetic energy (TKE). The TKE prediction equation was formulated using a second-order closure that relates the dissipation velocity to the TKE. The model also diagnostically determines the fractional area covered by rising motion (σ) and the entrainment rate (E).

Positive and negative entrainment rate parameterizations were developed, and the one used for a particular time step was based on the sums of the buoyancy (B) and shear (S) production (with and without E included). A tunable parameter was used to specify a fraction of the sums to check. This was done to prevent a large positive E from suddenly becoming negative. A value of 0.9 for this parameter was found to produce good results.

The positive entrainment rate was parameterized by assuming that E is proportional to the square root of the TKE. The constants in the parameterization were obtained by assuming a balance between buoyant production and dissipation, and using large-eddy simulation results from Deardorff (1974). This parameterization led to two Richardson number limits, Ri>>1 (strong inversion) and Ri=0 (no inversion).

The negative entrainment rate was parameterized by assuming that E and e_m are small compared to their values during rapid PBL growth. The local change term was then neglected in the e_m equation which led to a balance between the entrainment rate and $\dfrac{B + S - D}{e_m}$. A tunable parameter was then introduced to partition this balance equation into a weighted contribution of the local change of e_m and the production of e_m due to E. A value of 0.9 was used for the simulations and produced the best results.

Two simulations were run. The first simulation used the Wangara Day 33 PBL data. The surface heat flux was prescribed using a sine approximation. The ventilation (surface) mass flux was parameterized using the formulation from Louis (1979) and was used for the

122

surface momentum and moisture fluxes. The land simulation was initialized using the Wangara data.

The diurnal trend of the mixed layer depth, except for night values, was accurately depicted by the model. The model captured the slow growth early in the morning when there was a strong inversion, rapid growth during mid-morning when the inversion broke, slow growth during the afternoon under a quasi steady-state PBL topped by an inversion, and rapid decay after loss of surface heating at sunset. The nocturnal PBL did not grow slowly as expected. There appears to be a problem with the negative entrainment parameterization at night. The shear production at night due to the nocturnal jet should be sufficient to allow the PBL to grow even with negative buoyancy production.

Diagnostic variables to study the characteristics of a clear convective boundary layer (CBL) were developed using the concept of the convective mass flux model. Equations were presented for the plume-scale variance transport of a scalar, ψ, and updraft and downdraft properties of ψ. Then the convective mass flux was matched with the ventilation and entrainment layer fluxes. This was accomplished by assuming these layers were infinitesimal, and the small-eddy fluxes at levels S and B were negligible compared with the convective circulations. Use of the TKE then allowed the convective mass flux and the fractional area covered by rising motion to be determined using model variables.

The features of the CBL were well illustrated by the model diagnostic results. The model showed the dominance of buoyancy production over shear production in a CBL. This was shown by a plot of the buoyancy production versus the shear production, and by a plot of the plume-scale variance transport of θ at levels S and B. The entrainment rate was also shown to be an important mechanism, especially during rapid growth when E became large. The intense convection typical of a CBL was indicated by $\sigma \ll 1$. The convective mass flux was a minimum at this time, contrary to what one would expect. However, during vigorous convection when $E \gg V$, $\sigma \ll 1$, and M_C is small because $M_C \propto \sqrt{\sigma(1-\sigma)}$.

The updraft and downdraft properties further highlighted the CBL characteristics. The updrafts at level S were warmer and wetter than the downdrafts. Here, the convection was seen in terms of the surface heating rate and the surface heat and moisture transport rates. The dominance of one of these over the other was important in determining the behavior of the updraft and downdraft properties at the surface.

123

The inversion at the top of the PBL was the controlling factor for the updraft and downdraft properties at level B. When there was an inversion, the updraft air was cooler and wetter than the downdraft air. When the inversion was absent, the updraft air was warmer and much wetter than the downdraft air. This was caused by the strong convection that rapidly transported heat and moisture upwards.

Diagnostics for the PBL interior were developed to gain further insight into the CBL. A balance equation was presented for the variance of ψ. Each term in this equation was modeled to obtain equations for the variance and dissipation rate. A dissipation time scale in terms of the model parameter $\hat{\tau}$ was introduced. The balance equation was then solved to get a relation for the gradient of $\overline{\psi}$.

The dissipation time scale was found to be the shortest during the period when the surface heating was the strongest, corresponding to the high efficiency of the small-eddies. As expected at this time, the dissipation rates, ε_θ and ε_q, were at their largest values. The dissipation rate of θ at the surface dominated over the dissipation rate at level B. Again, this was due to the strong surface heating present. For q, the opposite was true. The large value of E caused the moisture flux at the PBL top to be much greater than at the surface, especially since mixing had reduced the surface to mixed layer moisture gradient.

The gradients of $\overline{\theta}$ and $\overline{q}$ were determined using a $\hat{\tau}$ of 10, 100, and 1000 seconds. The gradient results were matched to the Wangara data to determine the best value for $\hat{\tau}$. A value between 100 and 1000 seconds seemed most reasonable based on the data. The 1000 second gradients showed the expected increase in potential temperature with height and decrease of moisture with height, typical of a convective boundary layer.

A surface transfer coefficient was developed using the TKE, and was determined to be about an order of magnitude larger than the transfer coefficient normally found in the bulk aerodynamic formula for V. This was expected because the surface velocity was about 10 times the square root of the TKE. Using this transfer coefficient over the conventional one has the advantage that V exists if there is turbulence, even if the surface wind is zero. This may occur in a heated boundary layer where turbulence is generated only by buoyancy when the surface wind is calm.

The period when the inversion vanished was clearly indicated by the Richardson number. The limit for Ri=0 was about 1 during this time as expected. When the inversion was strong in the afternoon, the limit for Ri>>1 approached 0.2, but was too small. The assumption of the balance between buoyant production and dissipation that led to the relation for the limit when Ri>>1 may be slightly inaccurate.

A one-layer simulation using simple ocean data was then run to obtain steady-state solutions. Fixed surface and top mixing ratios, sea surface temperature, surface winds, and geostrophic winds were used. The temperature and winds at the top of the PBL were determined by constant lapse rates. The surface fluxes of heat, moisture, and momentum were determined using Louis (1979) ventilation mass flux formulation. A divergence of 4 10^{-6} s^{-1} was used to balance E in the Δp_m prediction equation.

The prognostic variables converged to their equilibrium values by 100 hours. The steady-state form of the prognostic equation for θ was derived. This equation was used to compare the value of θ with the model predicted value. The value from the equation was only 0.04 K different from that predicted by the model.

In a study done by Schubert et al. (1979), they found the adjustment time for the PBL depth was considerably longer than for the other prognostic variables when the ratio of $\dfrac{C_T V}{Dz_B + dz_B / dt}$ was about 4 or 5. This would indicate that surface transfer dominates over mixing at the PBL top. The value of the ratio obtained in the present ocean simulation was not constant, but was never less than 4.5. However, the adjustment time of the PBL depth was the same compared to the other prognostic variables.

This discrepancy can be explained by the different entrainment parameterization used in Schubert's study and the present model. In Schubert's study a constant small value of E was used, while in the present study E varied and became large during the early portion of the simulation. The large value of E allowed the PBL depth to adjust as fast as the other prognostic variables. This was shown by determining how long adjustment would have taken, had E been small and constant during the entire simulation. This adjustment time was about 77 days, which corresponds to an adjustment time for the PBL depth of about 20 times as long as the adjustment for the other variables. This agrees with the results obtained in Schubert's study.

125

A two-layer model that predicts the mean values of θ and q at two levels in the PBL was then developed to address the problem of the large gradients obtained by the one-layer model. The model was developed by equally spacing the levels for mathematical simplicity, even though the 2-level equations do not require these constraints. This model retains all the parameterizations used in the one-layer model. The only differences are the determination of the mixed layer values of θ and q, and the gradients of $\bar{\theta}$ and $\bar{q}$.

The two-layer model produced the same results for the prognostic variables using the Wangara data as the one-layer model. This verified that the model worked correctly. The gradients of $\bar{\theta}$ and $\bar{q}$ were near zero for the entire simulation which differed considerably from the one-layer model gradients. Identical results were also obtained for the ocean experiment.

The initial values of the mean values of θ and q at levels 1 and 2 were perturbed to study the effects of changing $\hat{\tau}$. The gradients were found to be larger at a given time step as $\hat{\tau}$ was increased. The gradients for all values of $\hat{\tau}$ except 1000 seconds approached zero within 60 minutes. Also, the mean values of the potential temperatures at levels S, 2, 1, and B converged to the mixed layer potential temperature within 60 minutes for all values of $\hat{\tau}$ except 1000 seconds. This result, along with the gradients from the one-layer model, indicate that a $\hat{\tau}$ near 100 seconds is the best choice.

Following is a summary of items that were presented for the first time in this thesis:

(1) A positive entrainment rate parameterization that assumed a balance between buoyancy production and dissipation of turbulence kinetic energy.

(2) A negative entrainment rate parameterization that allowed the PBL depth to decrease late in the day when buoyancy production was no longer sufficient to maintain the turbulence.

(3) A fully implicit finite difference equation for the TKE (when the entrainment rate is positive) solved as a cubic equation. The square of the solution that is always real was assigned to the TKE.

(4) Results for both the Wangara and Ocean studies showing the fractional area covered by rising motion, convective mass flux, updraft and downdraft properties of $\bar{\theta}$

126

and $\bar{q}$ at the surface and PBL top, dissipation rates of θ and q at the surface and PBL top, dissipation time scale, and gradients of $\bar{\theta}$ and $\bar{q}$.

(5) Results and comparison for the Wangara study of two surface bulk transfer coefficients, one dependent on the surface velocity and the other on the turbulence kinetic energy.

(6) A two-layer model which predicted $\bar{\theta}$ and $\bar{q}$ at two levels.

(7) Equations that determined the upward turbulent fluxes of θ and q in the interior of the PBL. These equations were used to obtain $\bar{\theta}$ and $\bar{q}$ in the two-layer model.

The one and two-layer models presented provide an accurate representation of the clear CBL. The turbulence characteristics are depicted by the prognostic turbulence kinetic energy equation. However, the PBL typically contains clouds. Future work should include adding cloud effects to these models. This can be approached in two steps. First, a simplified dry cloud layer should be added which would have the effect of radiatively cooling the air above the cloud. This is a relatively simple step. Next, as a more complex procedure, moist processes should be included. Lilly (1968) provides a means for accomplishing these steps.

Additional work should also be done to obtain a better representation for the nocturnal PBL. The positive and negative entrainment relations would have to be modified. The addition of more complicated radiative processes besides a simple radiative cooling term, and a parameterization that takes into account the nocturnal jet, may allow the PBL to grow at night.

The convective mass flux and the fractional area covered by rising motion were assumed to be constant with height. However, large-eddy simulations indicate that these variables are not constant with height. Height dependent equations for these variables should be developed. Randall et. al. (1992) provides a possible approach to accomplish this.

The two-layer model should also be further developed with the above suggestions. In addition, the momentum should be calculated at levels 1 and 2. Then all the prognostic variables would be determined at the same resolution. Next, cloud effects should be added

to allow the model to operate in a wide variety of meteorological conditions. The model should then be modified to make predictions at multiple levels. Finally, the model should be incorporated into the CSU GCM.

128

REFERENCES

André, J. C., G. D. Moor, P. Lacarrère, G. Therry, and R. D. Vachat, 1978: Modeling the 24-Hour Evolution of the Mean and Turbulent Structures of the Planetary Boundary Layer. *J. Atmos. Sci.*, **35**, 1861-1883.

Breidenthal, R. E., and M. B. Baker, 1985: Convection and Entrainment Across Stratified Interfaces. *J. Geophys. Res.*, **90D**, 13055-13062.

Businger, J. A., J. C. Wyngaard, Y. Izumi, and E. F. Bradley, 1971: Flux-Profile Relationships in the Atmospheric Surface Layer. *J. Atmos. Sci.*, **28**, 181-189.

Clarke, R. H., A. J. Dyer, R. R. Brook, D. G. Reid, and A. J. Troup, 1971: The Wangara Experiment: Boundary Layer Data. *Tech. Paper 19*, Div. Meteor. Phys., CSIRO, Australia.

Deardorff, J. W., 1970: Convective Velocity and Temperature Scales for the Unstable Planetary Boundary Layer and for Rayleigh Convection. *J. Atmos. Sci.*, **27**, 1211-1213.

Deardorff, J. W., 1972: Parameterization of the Planetary Boundary Layer for Use in General Circulation Models. *Mon. Wea. Rev.*, **100**, 93-106.

Deardorff, J. W., 1974a: Three-Dimensional Numerical Study of the Height and Mean Structure of a Heated Planetary Boundary Layer. *Bound. Layer Meteor.*, **7**, 81-106.

Deardorff, J. W., 1974b: Three-Dimensional Numerical Study of Turbulence in an Entraining Mixed Layer. *Bound. Layer Meteor.*, **7**, 199-266.

Garratt, J. R., 1992: *The Atmospheric Boundary Layer*, Cambridge University Press, Cambridge, Great Britain, 316 pp.

Lilly, D. K., 1968: Models of Cloud-Topped Mixed Layers Under a Strong Inversion. *Quart. J. R. Met. Soc.*, **94**, 292-309.

Louis, J.-F., 1979: A Parametric Model of Vertical Eddy Fluxes in the Atmosphere. *Bound. Layer Meteor.*, **17**, 187-202.

Mahrt, L., 1975: The Influence of Momentum Advections on a Well-Mixed Layer. *Quart. J. R. Met. Soc.*, **101**, 1-11.

Mahrt, L., 1981: The Early Evening Boundary Layer Transition. *Quart. J. R. Met. Soc.*, **107**, 329-343.

Moeng, C. H., 1984: A Large-Eddy Simulation Model for the Study of Planetary Boundary-Layer Turbulence. *J. Atmos. Sci.*, **41**, 2052-2062.

Moeng, C. H., and C. Wyngaard, 1988: Spectral Analysis of Large-Eddy Simulations of the Convective Boundary Layer. *J. Atmos. Sci.*, **45**, 3573-3587.

Nicholls, S. and J. D. Turton, 1986: An observational Study of the Structure of Stratiform Cloud Sheets: Part II. Entrainment. *Quart. J. R. Met. Soc.*, **112**, 461-480.

Paulson, C. A., 1970: The Mathematical Representation of Wind Speed and Temperature Profiles in the Unstable Atmospheric Surface Layer. *J. Appl. Meteorol.*, **9**, 857-861.

Randall, D. A., 1979: Conditional Instability of the First Kind Upside-Down. *J. Atmos. Sci.*, **37**, 125-130.

Randall, D. A., 1984: Buoyant Production and Consumption of Turbulence Kinetic Energy in Cloud-Topped Mixed Layers. *J. Atmos. Sci.*, **41**, 402-413.

Randall, D. A. and M. J. Suarez, 1984: On the Dynamics of Stratocumulus Formation and Dissipation. *J. Atmos. Sci.*, **41**, 3052-3057.

Randall, D. A., J. A. Abeles, and T. G. Corsetti, 1985: Seasonal Simulations of the Planetary Boundary Layer and Boundary-Layer Stratocumulus Clouds with a General Circulation Model. *J. Atmos. Sci.*, **42**, 641-676.

Randall, D. A., P. Sellers, and D. A. Dazlich, 1989: Applications of a Prognostic Turbulence Kinetic Energy in a Bulk Boundary-Layer Model. *Atmospheric Science Paper No. 437*, Colorado State University, 19 pp.

Randall, D. A. and Q. Shao, 1990: Formulation of a Bulk Boundary Layer Model with Partial Mixing and Cloudiness. *Atmospheric Science Paper No. 460*, Colorado State University, 47 pp.

Randall, D. A., Q. Shao, and C. H. Moeng, 1992: A Second-Order Bulk Boundary Layer Model. *J. Atmos. Sci.*, **49**, 1903-1923.

Schubert, W. H., J. S. Wakefield, E. J. Steiner, and S. K. Cox, 1979: Marine Stratocumulus Convection. Part I: Governing Equations and Horizontally Homogeneous Solutions. *J. Atmos. Sci.*, **36**, 1286-1307.

Schubert, W. H., J. S. Wakefield, E. J. Steiner, and S. K. Cox, 1979: Marine Stratocumulus Convection. Part II: Horizontally Inhomogeneous Solutions. *J. Atmos. Sci.*, **36**, 1308-1324.

Suarez, M. J., A. Arakawa, and D. A. Randall, 1983: The Parameterization of the Planetary Boundary Layer in the UCLA General Circulation Model: Formulation and Results. *Mon. Wea. Rev.*, **111**, 2224-2243.

Stull, R. C., 1988: *An Introduction to Boundary Layer Meteorology*, Kluwer Academic Publishers, Dordrecht, The Netherlands, 666 pp.

Taylor, P. A. and J. C. Wyngaard, 1990: *Planetary Boundary Layer Model Evaluation Workshop. World Climate Programme Research (WCPR-42)*, WMO, 46 pp.

Yamada, T., and G. L. Mellor, 1975: A Simulation of the Wangara Atmospheric Boundary Layer Data. *J. Atmos. Sci.*, **32**, 2309-2329.

Wyngaard, J. C., and R. A. Brost, 1984: Top-Down and Bottom-Up Diffusion of a Scalar in the Convective Boundary Layer. *J. Atmos. Sci.*, **41**, 102-112.

Yamada, T. and G. L. Mellor, 1975: A Simulation of the Wangara Atmospheric Boundary Layer Data, J. Atmos. Sci., 32, 2309-2329.

Wyngaard, J. C. and R. A. Brost, 1984: Top-Down and Bottom-Up Diffusion of a Scalar in the Convective Boundary Layer. J. Atmos. Sci., 41, 102-112.